



National Library  
of Canada

Bibliothèque nationale  
du Canada

Canadian Theses Service    Service des thèses canadiennes

Ottawa, Canada  
K1A 0N4

## NOTICE

The quality of this microform is heavily dependent upon the quality of the original thesis submitted for microfilming. Every effort has been made to ensure the highest quality of reproduction possible.

If pages are missing, contact the university which granted the degree.

Some pages may have indistinct print especially if the original pages were typed with a poor typewriter ribbon or if the university sent us an inferior photocopy.

Reproduction in full or in part of this microform is governed by the Canadian Copyright Act, R.S.C. 1970, c. C-30, and subsequent amendments.

## AVIS

La qualité de cette microforme dépend grandement de la qualité de la thèse soumise au microfilmage. Nous avons tout fait pour assurer une qualité supérieure de reproduction.

S'il manque des pages, veuillez communiquer avec l'université qui a conféré le grade.

La qualité d'impression de certaines pages peut laisser à désirer, surtout si les pages originales ont été dactylographiées à l'aide d'un ruban usé ou si l'université nous a fait parvenir une photocopie de qualité inférieure.

La reproduction, même partielle, de cette microforme est soumise à la Loi canadienne sur le droit d'auteur, SRC 1970, c. C-30, et ses amendements subséquents.

THE UNIVERSITY OF ALBERTA

INTENSITY ARTIFACTS IN MRI

BY

SCOTT ROBERTSON

A THESIS

SUBMITTED TO THE FACULTY OF GRADUATE STUDIES AND  
RESEARCH IN PARTIAL FULFILMENT OF THE REQUIREMENTS FOR  
THE DEGREE OF MASTER OF SCIENCE

DEPARTMENT OF PHYSICS

EDMONTON, ALBERTA

SPRING, 1989

Permission has been granted to the National Library of Canada to microfilm this thesis and to lend or sell copies of the film.

The author (copyright owner) has reserved other publication rights, and neither the thesis nor extensive extracts from it may be printed or otherwise reproduced without his/her written permission.

L'autorisation a été accordée à la Bibliothèque nationale du Canada de microfilmer cette thèse et de prêter ou de vendre des exemplaires du film.

L'auteur (titulaire du droit d'auteur) se réserve les autres droits de publication; ni la thèse ni de longs extraits de celle-ci ne doivent être imprimés ou autrement reproduits sans son autorisation écrite.

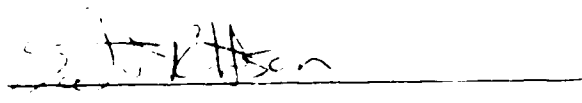
ISBN 0-315-52829-X

THE UNIVERSITY OF ALBERTA  
RELEASE FORM

NAME OF AUTHOR: SCOTT ROBERTSON  
NAME OF THESIS: INTENSITY ARTIFACTS IN MRI  
DEGREE: M.Sc  
YEAR THIS DEGREE GRANTED: 1989

Permission is hereby granted to THE UNIVERSITY OF ALBERTA LIBRARY to reproduce single copies of this thesis and to lend or sell such copies for private, scholarly or scientific research purposes only.

The author reserves other publication rights, and neither the thesis nor extensive extracts from it may be printed or otherwise reproduced without the author's written permission.

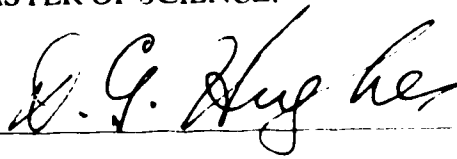


155 Deergrove Cresc.,  
Regina, Sask.,  
S4S 5M2


DATE: January 4, 1989


THE UNIVERSITY OF ALBERTA  
FACULTY OF GRADUATE STUDIES AND RESEARCH

The undersigned certify that they have read, and recommend to the Faculty of Graduate Studies and Research for acceptance, a thesis entitled "INTENSITY ARTIFACTS IN MRI" submitted by SCOTT ROBERTSON in partial fulfilment of the requirements for the degree of MASTER OF SCIENCE.

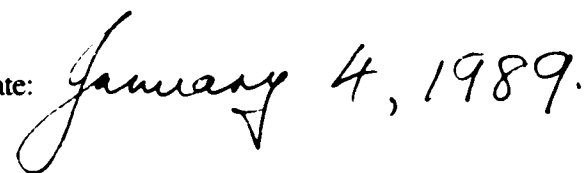


( Supervisor )







Date: 

## ABSTRACT

The recently developed technique of nuclear magnetic resonance imaging (MRI) is an important diagnostic tool in medicine. The most common method, two-dimensional Fourier transform imaging, utilizes pulsed magnetic field gradients to achieve spatial encoding. Serious intensity artifacts related to these gradient pulses have been observed using the technique and this thesis describes a study of these artifacts on images obtained with the University of Alberta animal-sized NMR system.

For simplicity, the slice selection and phase encoding procedures were eliminated and intensity artifacts associated with one-dimensional spin-echo proton projections of a 10 cm x 10 cm x 3 mm square slice phantom were studied. The imaging sequence consisted of the following: a  $\pi/2$ -pulse to uniformly excite the spins throughout the sample, a "read compensation" gradient pulse, a  $\pi$ -pulse causing the spins to refocus at a later time, followed by the application of a read gradient pulse during which the echo forms and is sampled. By varying the timings in the imaging sequence, information was obtained about more important causes of intensity artifacts, i.e. deviations from a "top-hat" projection. It was found that serious intensity artifacts arose if the  $\pi$ -pulse was applied less than about 2 ms after the switch-off of the read compensation pulse. This was due to the finite decay time of the gradient field as governed by the  $L/R$  ratio of the gradient coil.

The other main causes of serious intensity artifacts stemmed from eddy currents which are induced in metallic parts of the cryostat of the superconducting magnet as a result of the gradient switchings. The effect of the eddy currents was studied by measuring the time dependence of the magnetic field following the switch-off of a gradient pulse, using a small spherical sample placed at various positions in the magnet. These measurements showed that the

eddy currents cause an inhomogeneous and time dependent magnetic field, in addition to a time-dependent magnetic field gradient. The inhomogeneous and time dependent magnetic field causes the echoes from different regions of the sample to form at different times leading to intensity artifacts. It also causes nuclei lying on an isochromat to experience different phase shifts prior to data acquisition, thereby causing reduced intensity through destructive interference.

## ACKNOWLEDGEMENTS

Above all I would like to thank Dr. D. G. Hughes , my research supervisor, for his guidance, assistance and interest in this project and Dr. P. S. Allen for his assistance and for allowing me the opportunity to perform this project in his laboratory.

I also wish to thank Dan Doran, Chris Hanstock, Karim D. . . . . and Trimble for their assistance in learning about the experimental equipment.

Finally, I wish to express my gratitude to the University of Alberta for financial support in the form of Graduate Assistantships, the Province of Alberta for financial support in the form of a Province of Alberta Graduate Scholarship, and to NSERC for financial aid in carrying out this project.



# TABLE OF CONTENTS

Chapter	Page
1. INTRODUCTION.....	1
2. THEORY OF NMR AND NMR IMAGING.....	4
2.1 Elementary description of NMR .....	4
2.2 Bloch equations .....	7
2.3 Magnetization in the rotating frame .....	8
2.4 Spin-echo techniques .....	12
2.5 Detection of NMR .....	12
2.6 NMR imaging .....	16
3. IMAGE INTENSITY ARTIFACTS IN MRI.....	23
3.1 Intensity artifacts due to imperfections in the rf field $B_1$ .....	23
3.2 Intensity artifacts arising from inhomogeneity in the steady magnetic field $B_0$ .....	23
3.3 Intensity artifacts associated with the use of a finite data acquisition period .....	24
3.4 Intensity artifacts associated with dielectric resonances .....	24
3.5 Intensity artifacts associated with non-ideality of the gradient pulses .....	25
3.5.1 Generation of pulsed magnetic field gradients; eddy currents .....	25
3.5.2 Intensity artifacts arising from the finite decay time of the read compensation gradient pulse .....	27
3.5.3 Effect of phase shifts caused by eddy currents .....	34

3.5.4	Effect of improper refocussing of the spin-echo signal .....	34
4.	EXPERIMENTAL DETAILS.....	38
4.1	Description of the NMR hardware .....	38
4.2	NMR samples.....	38
4.3	Set-up procedure .....	39
4.4	Pulse program and phantom set-up used to acquire projections .....	40
4.5	Pulse program and set-up to study eddy field decays .....	44
4.6	Dielectric resonances .....	47
5.	RESULTS.....	48
5.1	Inhomogeneity of $B_1$ .....	48
5.2	Inhomogeneity of $B_0$ .....	48
5.3	Finite data acquisition period.....	49
5.4	Dielectric resonances.....	49
5.5	Eddy currents results .....	52
5.5.1	Projections obtained with a read compensation gradient pulse of 5 ms duration.....	57
5.5.2	Projections obtained with a read compensation gradient pulse of 25 ms duration.....	65
5.5.3	Measurements of the offset frequencies due to the magnetic field and field gradient arising from the eddy currents.....	72
6.	ANALYSIS AND DISCUSSION OF RESULTS.....	103
6.1	Off-resonance effects.....	103

6.2	Phase shifts caused by eddy currents.....	113
6.3	Improper refocussing of the spin-echo.....	117
7.	CONCLUSIONS AND RECOMMENDATIONS.....	124
	BIBLIOGRAPHY.....	126

## LIST OF FIGURES

Figure	Page
1. Precession of the nuclear magnetization $\vec{M}$ ( for $\gamma > 0$ ) in the rotating frame about an "on-resonance" $\vec{B}_1$ field through an angle of a) $\theta$ , b) $\pi/2$ and c) $\pi$ radians .....	11
2. A spin-echo experiment. A $\pi/2$ -pulse along the $x'$ axis rotates the magnetization to the $y'$ axis. ....	14
3. A spin-echo imaging experiment. ....	20
4. The magnetic field $\vec{B}_{eff}$ in the rotating frame experienced by a system of nuclei. ....	29
5. The normalized transverse magnetization at time $T_E$ , $(M_x'y')_{TE} / M_0$ , plotted as a function of $\Delta B/B_1$ , where $\Delta B$ is the offset field in the $z$ direction due to the decay of the gradient pulse and $B_1$ is the amplitude of the rf field. ....	36
6. Schematic diagram of the pulse program SRPP.PC used to generate projections of the slice phantom. ....	42
7. Schematic diagram of the pulse program CHECP.M used to measure the decay of the magnetic field after the switch-off of a gradient pulse. ....	46

8.	The real part of the time-domain echo-envelope acquired using the pulse program SRPP.PC with no gradient pulses. ....	50
9.	Projections obtained with the slice phantom filled with doped ( 5 mMolar CuSO <sub>4</sub> ) water ( dielectric constant $\cong$ 80 ) and with cyclohexane ( dielectric constant $\cong$ 2 ) obtained under the same experimental conditions. ....	53
10.	Field homogeneity plot in frequency units as given by the Fourier transform of the FID signal emanating from the slice phantom filled with doped ( 5 mMolar CuSO <sub>4</sub> ) water. ....	56
11.	Projections of the slice phantom acquired using the doped water sample and the pulse program SRPP.PC ( see Fig. 6 ) with D25 = 150 $\mu$ s, D3 = 5 ms, D7 = 5 ms, D1 = 300 $\mu$ s, D2 = 2 ms and $\tau_{aq}/2$ = 6.4 ms. ....	59
12.	Projections of the slice phantom acquired using the doped water sample and the pulse program SRPP.PC ( see Fig. 6 ) with D25 = 150 $\mu$ s, D3 = 5 ms, D7 = 5 ms, D1 = 300 $\mu$ s, D2 = 2 ms and $\tau_{aq}/2$ = 6.4 ms. ....	61
13.	Projections of the slice phantom acquired using the doped water sample and the pulse program SRPP.PC ( see Fig. 6 ) with D25 = 150 $\mu$ s, D3 = 5 ms, D7 = 5 ms, D6 = 5 ms, D1 = 300 $\mu$ s and $\tau_{aq}/2$ = 6.4 ms. ....	64

14. Projections of the slice phantom acquired using the doped water sample and the pulse program SRPP.PC ( see Fig. 6 ) with  $D_{25} = 150 \mu\text{s}$ ,  $D_3 = 12 \text{ ms}$ ,  $D_7 = 25 \text{ ms}$ ,  $D_1 = 300 \mu\text{s}$ ,  $D_2 = 30.2 \text{ ms}$  and  $\tau_{\text{aq}}/2 = 6.4 \text{ ms}$ . .....67
15. Projections of the slice phantom acquired using the doped water sample and the pulse program SRPP.PC ( see Fig. 6 ) with  $D_{25} = 150 \mu\text{s}$ ,  $D_3 = 12 \text{ ms}$ ,  $D_7 = 25 \text{ ms}$ ,  $D_1 = 300 \mu\text{s}$ ,  $D_2 = 30.2 \text{ ms}$  and  $\tau_{\text{aq}}/2 = 6.4 \text{ ms}$ . .....69
16. Projections of the slice phantom acquired using the doped water sample and the pulse program SRPP.PC ( see Fig. 6 ) with  $D_{25} = 150 \mu\text{s}$ ,  $D_3 = 12 \text{ ms}$ ,  $D_7 = 25 \text{ ms}$ ,  $D_6 = 20 \text{ ms}$ ,  $D_1 = 300 \mu\text{s}$ , and  $\tau_{\text{aq}}/2 = 6.4 \text{ ms}$ . .....71
17. Frequency offset ( $F_{\text{offset}}$ ) at locations  $x = +4 \text{ cm}$ ,  $y = 0 \text{ cm}$  ( crosses ),  $y = +5 \text{ cm}$  ( closed circles ) and  $y = -5 \text{ cm}$  ( open circles), plotted as a function of the time  $t$  after switch-off of a  $5 \text{ ms}$  gradient pulse. ....74
18. Frequency offset ( $F_{\text{offset}}$ ) at locations  $x = 0 \text{ cm}$ ,  $y = 0 \text{ cm}$  ( crosses ),  $y = +5 \text{ cm}$  ( closed circles ) and  $y = -5 \text{ cm}$  ( open circles ), plotted as a function of the time  $t$  after switch-off of a  $5 \text{ ms}$  gradient pulse. ....76

19. Frequency offset ( $F_{\text{offset}}$ ) at locations  $x = -4$  cm,  $y = 0$  cm (crosses),  $y = +5$  cm (closed circles) and  $y = -5$  cm (open circles), plotted as a function of the time  $t$  after switch-off of a 5 ms gradient pulse. ....78
20. Frequency offset ( $F_{\text{offset}}$ ) at locations  $x = +4$  cm,  $y = 0$  cm (crosses),  $y = +5$  cm (closed circles) and  $y = -5$  cm (open circles), plotted as a function of the time  $t$  after switch-off of a 25 ms gradient pulse. ....81
21. Frequency offset ( $F_{\text{offset}}$ ) at locations  $x = +0$  cm,  $y = 0$  cm (crosses),  $y = +5$  cm (closed circles) and  $y = -5$  cm (open circles), plotted as a function of the time  $t$  after switch-off of a 25 ms gradient pulse. ....83
22. Frequency offset ( $F_{\text{offset}}$ ) at locations  $x = -4$  cm,  $y = 0$  cm (crosses),  $y = +5$  cm (closed circles) and  $y = -5$  cm (open circles), plotted as a function of the time  $t$  after switch-off of a 25 ms gradient pulse. ....85
23. Frequency offset ( $F_{\text{offset}}$ ) at locations  $y = 0$  cm,  $x = 0$  cm (crosses),  $x = +4$  cm (closed circles) and  $x = -4$  cm (open circles), plotted as a function of the time  $t$  after switch-off of a 5 ms gradient pulse. ....87

24. Frequency offset ( $F_{\text{offset}}$ ) at locations  $y = 0$  cm,  $x = 0$  cm ( crosses ),  $x = +4$  cm ( closed circles ) and  $x = -4$  cm ( open circles ), plotted as a function of the time  $t$  after switch-off of a 25 ms gradient pulse. .... 9
25. Difference between the offset frequencies at  $y = \pm 5$  cm and  $y = 0$  cm for  $x = +4$  cm plotted as a function of time after switch-off of a 5 ms gradient pulse. ....92
26. Difference between the offset frequencies at  $y = \pm 5$  cm and  $y = 0$  cm for  $x = 0$  cm plotted as a function of time after switch-off of a 5 ms gradient pulse. ....94
27. Difference between the offset frequencies at  $y = \pm 5$  cm and  $y = 0$  cm for  $x = -4$  cm plotted as a function of time after switch-off of a 5 ms gradient pulse. ....96
28. Difference between the offset frequencies at  $y = \pm 5$  cm and  $y = 0$  cm for  $x = +4$  cm plotted as a function of time after switch-off of a 25 ms gradient pulse. ....98
29. Difference between the offset frequencies at  $y = \pm 5$  cm and  $y = 0$  cm for  $x = 0$  cm plotted as a function of time after switch-off of a 25 ms gradient pulse. ....100



30. Difference between the offset frequencies at  $y = \pm 5$  cm and  $y = 0$  cm for  $x = -4$  cm plotted as a function of time after switch-off of a 25 ms gradient pulse. ....102
31. Projection obtained using the slice phantom filled with doped water and the pulse program SRPP.PC with  $D7 = 5$  ms ,  $D6 = 1$  ms,  $D25 = 150$   $\mu$ s,  $D3 = 5$  ms,  $D1 = 300$   $\mu$ s,  $D4 = 2.6$  ms and  $\tau_{aq}/2 = 6.4$  ms together with calculated projection based on the off-resonance effect . ....105
32. Projection obtained using the slice phantom filled with doped water and the pulse program SRPP.PC with  $D7 = 5$  ms ,  $D6 = 2$  ms,  $D25 = 150$   $\mu$ s,  $D3 = 5$  ms,  $D1 = 300$   $\mu$ s,  $D4 = 2.6$  ms and  $\tau_{aq}/2 = 6.4$  ms together with calculated projection based on the off-resonance effect. ....107
33. Projection obtained using the slice phantom filled with doped water and the pulse program SRPP.PC with  $D7 = 25$  ms ,  $D6 = 1$  ms,  $D25 = 150$   $\mu$ s,  $D3 = 5$  ms,  $D1 = 300$   $\mu$ s,  $D4 = 2.6$  ms and  $\tau_{aq}/2 = 6.4$  ms together with calculated projection based on off-resonance effect. ....109

34. Projection obtained using the slice phantom filled with doped water and the pulse program SRPP.PC with  $D7 = 25 \text{ ms}$ ,  $D6 = 2 \text{ ms}$ ,  $D25 = 150 \mu\text{s}$ ,  $D3 = 5 \text{ ms}$ ,  $D1 = 300 \mu\text{s}$ ,  $D4 = 2.6 \text{ ms}$  and  $\tau_{\text{aq}}/2 = 6.4 \text{ ms}$  together with calculated projection based on off-resonance effect. ....111

## LIST OF TABLES

Table	Page
<p>I. Calculated values using equation 39 of the normalized transverse magnetization <math>M_{x'y'}/M_0</math> resulting from phase effects at positions <math>x = +4</math> cm, 0 cm and -4 cm as a function of D7, the duration of the read compensation gradient pulse, D2, the duration of the read gradient before the data acquisition and D6, the delay between the read compensation pulse switch-off and the <math>\pi</math>-pulse. ....</p>	116
<p>II. Calculated values of the phase shift <math>\psi / 2\pi</math> at <math>x = +4</math> cm and <math>x = -4</math> cm caused by eddy currents as a function of D7, the duration of the read compensation gradient pulse and D6, the delay between the switch-off of this gradient pulse and the <math>\pi</math>-pulse. ....</p>	118
<p>III. Corrected phase shifts <math>\psi_{\text{corr}} / 2\pi</math> at positions <math>x = +4</math> cm and <math>x = -4</math> cm as a function of D7, the duration of the read compensation gradient pulse and D6, the delay between the switch-off of this gradient and the <math>\pi</math>-pulse. ....</p>	119
<p>IV. Values of the time difference <math>\Delta t</math> (ms) between the time of echo formation and <math>T_E</math> for nuclei at <math>x = +4</math> cm and <math>x = -4</math> cm as a function of D7, the duration of the read compensation gradient and D6, the delay between the switch-off of this gradient and the <math>\pi</math>-pulse. ....</p>	121

## CHAPTER 1

### INTRODUCTION

Since its discovery in 1945, Nuclear Magnetic Resonance ( NMR ) has been used extensively to investigate the physical and chemical properties of matter. To observe NMR signals in the early days, the sample was exposed to a continuous wave (cw) rf magnetic field and the steady magnetic field was swept linearly through the resonance region. An important advance was the development of pulsed NMR in which the sample is exposed to a short, intense rf pulse while the magnetic field is kept constant. Fourier transformation of the time domain-signal received immediately after the pulse gives the same spectral information as that obtained using the cw technique. The pulse method has the advantage that since all of the NMR frequencies within the sample can be simultaneously excited with the rf pulse, spectra can be obtained much more rapidly.

Gabillard ( 1953 ) made the important observation that in the presence of a linear magnetic field gradient, the NMR frequency is a measure of the spatial offset in the direction of the gradient. More recently, NMR has been applied to medicine. Lauterbur (1973) and Mansfield (1973) took advantage of the behavior of the NMR frequencies in the presence of a gradient field to achieve spatial discrimination or NMR imaging ( MRI ). Early techniques of spatial encoding made use of steady magnetic field gradients whereas more recent techniques, such as two-dimensional Fourier transform ( 2DFT ) imaging, involve short, pulsed gradients. In 2DFT imaging, currently the most common MRI modality, two orthogonal field gradients are used to spatially encode, in two dimensions, the NMR signals coming from the different regions of the sample. Two-dimensional Fourier transformation of the time domain signals will then produce a two-dimensional spectrum or image.

The original idea for the thesis work was to study microcirculatory flow or perfusion through the brain. The method proposed to perform this was to subtract two images from two different sequences with different gradient pulses, one sensitive to flow, the other not, such that the subtraction would remove the contribution of stationary spins ( Cho et al., 1987 ). Early on in the work, it was found that images obtained with long pulsed gradients had severe intensity artifacts whose causes were not immediately apparent. Upon further examination, it was found that these intensity artifacts depended very strongly and in a complicated way on the experimental conditions such as the duration of the gradients and the time locations of the gradients within the pulse sequences. Since these were different for the two images to be subtracted, a true representation of the distribution of flowing spins would not be obtained upon subtraction. The elimination of serious intensity artifacts is of great importance in routine imaging and is crucial in any flow measuring technique which involves the subtraction of two images.

Lai ( 1983 ) studied image artifacts arising from inhomogeneity in the main magnetic field and non-linearity in the gradient fields, effects which proved to be unimportant in our case. Vollmann ( 1984 ) studied the effect of a non-linear radio frequency receiving amplifier on the quality of images in NMR. He found the effect to be negligible, and this is to be expected if, as is usually the case, phase sensitive detection is used. Brateman et al. ( 1986 ) studied image artifacts using simple phantoms and found geometric distortions and non-uniformity of signal intensity in the images. They found a correlation between the non-uniformity of the signal intensity and variations in the magnitude of the rf field. Henkelman and Bronskill ( 1987 ) considered various intensity artifacts but did not consider in detail those which we found important in our work. The work in this thesis considers some of the effects described by these workers but in much more detail.

In two-dimensional imaging, the slice to be imaged is normally selected by initially applying a suitably shaped rf pulse in the presence of a linear magnetic field gradient. To avoid intensity artifacts associated with imperfections in the slice-selection process, our imaging was done using a sample in the shape of a square phantom with uniform but small thickness. In that way, intensity artifacts associated with the slice selection process are eliminated.

It has been found that some of the observed intensity artifacts are caused by the rapid switchings of the field gradients. When a gradient is switched on or off in an NMR experiment, eddy currents are induced in nearby conducting materials such as the cryostat in a superconducting system. These in turn create an inhomogeneous magnetic field which decays with multiple time constants because of the different resistances and inductances of the various eddy current loops. This decaying field will be superimposed upon the field produced by the current in the gradient coil and cause intensity artifacts. Also, an effect associated with the finite decay time of the field gradient coil has been observed.

The basic theory of NMR and MRI is developed in Chapter 2 followed, in Chapter 3, by a discussion of various mechanisms which can cause intensity artifacts. Experimental details are described in Chapter 4. The results are presented in Chapter 5 and analyzed and discussed in Chapter 6. Some conclusions and recommendations are presented in Chapter 7.

## CHAPTER 2

### THEORY OF NMR AND NMR IMAGING

#### 2.1 Elementary description of NMR

The following is a brief outline of the theory behind NMR imaging. ( For a more complete description of the theory, see the well-known books dealing with NMR by Abragam (1961), Slichter (1963), Farrar and Becker (1971) and Morris (1986) )

NMR takes advantage of the nuclear magnetic moment  $\vec{\mu}$  of specific nuclei such as  $^1\text{H}$ ,  $^{13}\text{C}$ ,  $^{31}\text{P}$  and  $^{19}\text{F}$  where  $\vec{\mu}$  is given by

$$\vec{\mu} = \gamma \hbar \vec{I} \quad (1)$$

and  $\gamma$  is the magnetogyric ratio which is unique for each nucleus,  $\hbar$  is Planck's constant divided by  $2\pi$  and  $\vec{I}$  is the spin of the nucleus. Only nuclei with non-zero spin exhibit the NMR phenomenon.

A simple quantum mechanical analysis leads to a resonance condition or frequency which is the same as the classical Larmor precessional frequency. Since this thesis is concerned only with proton NMR, the discussion will be restricted to nuclei with spin  $I = 1/2$  nuclei. If such a nucleus is situated in a steady magnetic field  $\vec{B}_0$  parallel to the z-axis, it will have two possible energy levels, with energies given by

$$E = -\mu_z B_0 = -\gamma \hbar m B_0 \quad (2)$$

where  $m$  is the z-component of spin angular momentum with possible values of  $\pm 1/2$ .

The energy difference  $\Delta E$  between the levels is given by

$$\Delta E = \gamma \hbar B_0 \quad (3)$$

so that the frequency  $\omega_0$  of a quantum which causes a transition from one energy level to the other will be

$$\omega_0 = \Delta E / \hbar = \gamma B_0. \quad (4)$$

This is the same as the classical Larmor frequency of a spinning magnetic moment ( Slichter, 1963 ).

For an ensemble of spins, the nuclei will be distributed among the two energy levels according to the Boltzmann distribution so that more spins will be aligned parallel to  $B_0$  than antiparallel, thus giving rise to a net magnetic moment  $\vec{M}$  parallel to  $B_0$ . If the populations of the two energy levels are perturbed by, for example, applying an rf field with frequency  $\omega_0$ , the populations will return to their equilibrium values exponentially in a characteristic time  $T_1$ , known as the spin-lattice or longitudinal relaxation time, by interacting with its surrounding lattice. One can predict the natural linewidth of a particular resonance arising from this phenomenon. Using the Heisenberg Uncertainty Principle

$$\Delta E \Delta t \geq \hbar \quad (5)$$

and the fact that the mean lifetime of the spin state will be  $T_1$ , one may deduce that the transition will exhibit a natural linewidth,  $\Delta\omega = \Delta E / \hbar$ , which, if defined as being the linewidth between half-maximum points, is given by  $2 / T_1$ .



Spin-lattice relaxation is usually caused by the magnetic dipole-dipole interaction where one nuclear spin  $\vec{I}_1$  is affected by the dipole field of neighboring spin  $\vec{I}_2$ . If  $\vec{I}_2$  is moving relative to  $\vec{I}_1$  such that its frequency of motion has components at  $\omega_0$  or  $2\omega_0$ , this will cause  $\vec{I}_1$  to undergo a transition to the other energy state and thus cause spin-lattice relaxation.

The excitation of a spin system in NMR, in general, generates a transverse component of magnetization which rotates in the xy plane around the magnetic field direction. The presence of a distribution of local magnetic fields generated by neighboring magnetic nuclei causes a dephasing of the spins as they precess about  $\vec{B}_0$ . As a result, the transverse magnetization will decay, in many cases exponentially, with a characteristic time  $T_2$  called the spin-spin or transverse relaxation time.

Processes that give rise to longitudinal relaxation will at the same time cause a decay of the transverse magnetization. In addition, other mechanisms can cause the transverse magnetization to decay more rapidly than by the  $T_1$  processes alone. NMR signals are observed via the transverse magnetization so the NMR linewidth is governed by  $T_2$  rather than  $T_1$ , with  $T_2 \leq T_1$  always. If the  $T_2$  relaxation is exponential, the linewidth  $\Delta\omega$  between half-maximum points is given by  $2/T_2$ .

$T_2$  relaxation is caused by similar processes to  $T_1$  except that magnetic field fluctuations at low frequencies also contribute. For instance, if nuclei experience different static fields, they will precess at different rates and thus dephase, or relax.

An important point to mention here is that the relaxation times are normally quite different for spins in a liquid and a solid. In a solid, the positions of the various spins relative to each other and thus the magnetic field at one spin site due to the other spins, stays relatively constant due to a lack of translational motion. However, in a liquid, the orientation of the internuclear vectors relative to the magnetic field continually changes, thereby giving rise to a fluctuating local magnetic field. The motion is usually extremely rapid and the given nucleus sees only the average field due to the other spins.

This leads to much longer  $T_2$ 's for liquids than solids and, thus, much narrower linewidths. For a more thorough discussion of this and other magnetic relaxation mechanisms, see Farrar and Becker (1971).

An inhomogeneity in the static magnetic field  $\vec{B}_0$  will also cause a dephasing of the various nuclear spins and will contribute to the observed linewidth. If the decay in the transverse magnetization caused by the inhomogeneity in  $B_0$  is exponential, the two contributions can be added so that the overall observed linewidth at half-maximum can be written as

$$\Delta\omega = 2 / T_2 + \gamma \Delta B_0 = 2 / T_2^* \quad (6)$$

where  $\Delta B_0$  is the width of the  $B_0$  distribution at half-maximum. Here,  $T_2^*$  is a modified spin-spin relaxation time which includes the effects of the static field inhomogeneity.

## 2.2 Bloch equations

Bloch et. al. (1946) described the motion of macroscopic magnetization  $\vec{M}$ , resulting from an ensemble of nuclei, in the presence of a static field  $\vec{B}_0$  and an applied rf field  $\vec{B}_1$  by the phenomenological Bloch equations. In the absence of relaxation, the rate of change of  $\vec{M}$  is given by

$$d\vec{M}/dt = \gamma \vec{M} \times \vec{B} \quad (7)$$

where  $\vec{B}$  is the vector sum of  $\vec{B}_0$  and  $\vec{B}_1$ . If  $\vec{B}_1$  is transverse, initially along the x-axis, and rotates at a frequency  $\Omega$  about the z-axis, then

$$\vec{B} = \vec{B}_1 + \vec{B}_0 = B_1 \cos \Omega t \hat{x} - B_1 \sin \Omega t \hat{y} + B_0 \hat{z}. \quad (8)$$

Substitution in equation (7) gives

$$dM_x / dt = \gamma ( M_y B_0 + M_z B_1 \sin \Omega t ) \quad (9a)$$

$$dM_y / dt = \gamma ( M_z B_1 \cos \Omega t - M_x B_0 ) \quad (9b)$$

$$dM_z / dt = -\gamma ( M_x B_1 \sin \Omega t + M_y B_1 \cos \Omega t ) \quad (9c)$$

If relaxation effects are included and the decay is assumed to be exponential, the above equations (9a,b,c) become

$$dM_x / dt = \gamma ( M_y B_0 + M_z B_1 \sin \Omega t ) - M_x / T_2 \quad (10a)$$

$$dM_y / dt = \gamma ( M_z B_1 \cos \Omega t - M_x B_0 ) - M_y / T_2 \quad (10b)$$

$$dM_z / dt = -\gamma ( M_x B_1 \sin \Omega t + M_y B_1 \cos \Omega t ) - ( M_z - M_0 ) / T_1 \quad (10c)$$

These are the so-called Bloch equations.

### 2.3 Magnetization in the rotating frame

To understand what happens to  $\vec{M}$  under the influence of  $\vec{B}_1$  and  $\vec{B}_0$ , it is easier to observe its motion from a frame rotating about  $B_0$  with the same frequency  $\Omega$  and in the same sense as  $\vec{B}_1$ . The equivalent of equation (7) in this frame is given by (Slichter, 1963)

$$(d\vec{M} / dt)_{\text{rot}} = \gamma \vec{M} \times \vec{B} - \vec{\Omega} \times \vec{M} = \gamma ( \vec{M} \times ( \vec{B} + \vec{\Omega} / \gamma ) )$$

$$= \gamma (\vec{M} \times \vec{B}_{\text{eff}}) \quad (11)$$

where  $\vec{B}_{\text{eff}}$  is an effective field given by  $\vec{B} + \vec{\Omega}/\gamma$ . If  $\vec{B} = \vec{B}_0 + \vec{B}_1$ , then

$$\vec{B}_{\text{eff}} = \vec{B}_0 + \vec{\Omega}/\gamma + \vec{B}_1 \quad (12)$$

and, if  $\vec{\Omega} = -\gamma \vec{B}_0$ , the Larmor frequency, then  $\vec{B}_{\text{eff}} = \vec{B}_1$ . Since  $\vec{B}_1$  rotates at the same frequency as the rotating frame,  $\vec{B}_1$  is stationary in the rotating frame and  $\vec{M}$  will precess about  $\vec{B}_1$  with a frequency

$$\omega = \gamma B_1. \quad (13)$$

If  $\vec{B}_1$  is applied for a time  $\tau$  along the x-axis of the rotating frame, the angle of precession of the magnetization about this axis will be

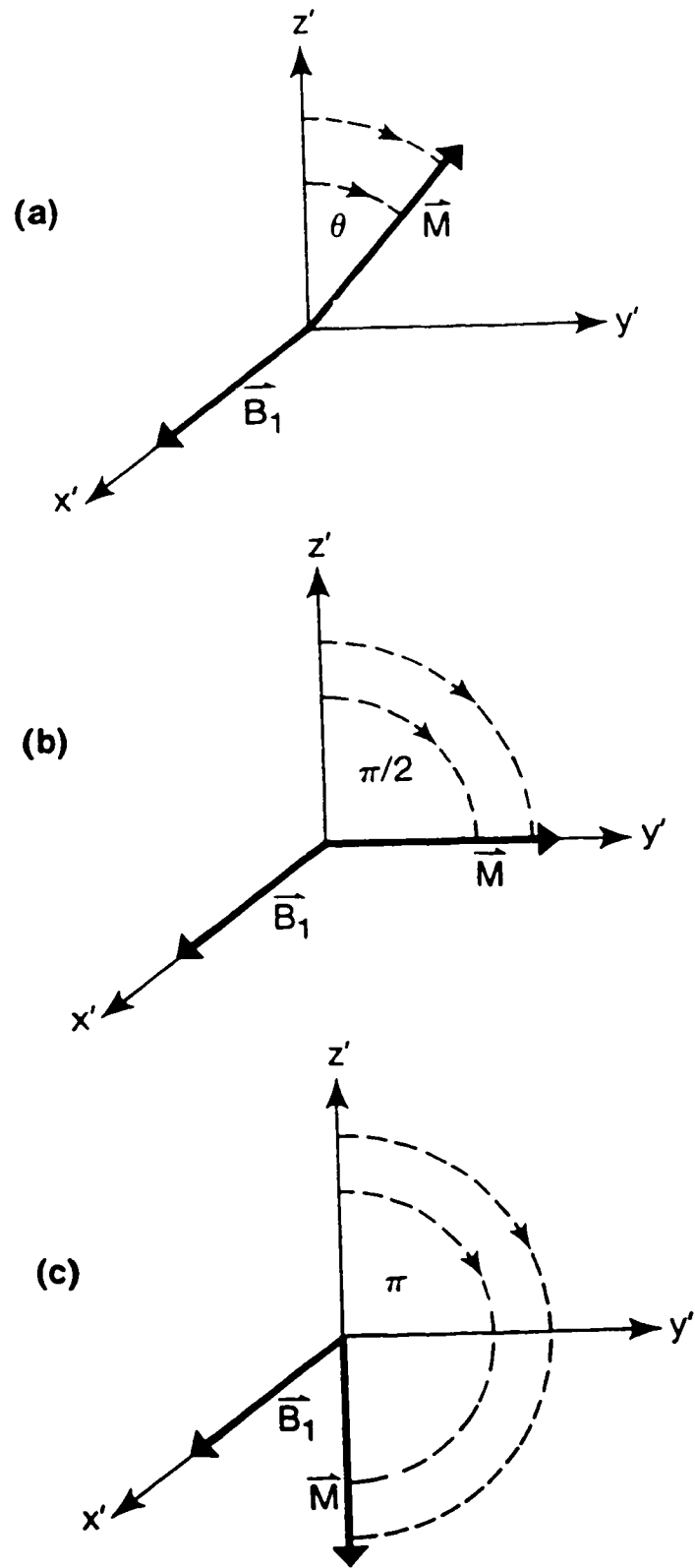
$$\theta = \omega \tau = \gamma B_1 \tau \quad (14)$$

as indicated in Fig. 1. By suitable choice of  $B_1$  or  $\tau$ , one can rotate  $\vec{M}$  by  $\pi/2$  radians from the z axis to bring the magnetization into the xy plane or by  $\pi$  radians to create -z magnetization as shown in Fig. 1.

As can be seen from equations 11 and 12, if  $\vec{B}_1$  is not "on-resonance", i.e.  $\Omega \neq -\gamma B_0$ ,  $\vec{M}$  will be rotated about an axis tilted away from the x-axis in the rotating frame. The rotation of  $\vec{M}$  will then deviate from the desired angle and, the greater  $\vec{B}_1$  is off resonance, the greater this deviation until such a point that a  $\pi/2$  pulse would create negligible transverse magnetization.

Fig. 1

Precession of the nuclear magnetization  $\vec{M}$  ( for  $\gamma > 0$  )  
rotating frame about an "on-resonance"  $\vec{B}_1$  field through an angle  
radians ) of a)  $\theta$ , b)  $\pi/2$  and c)  $\pi$ . The primes here refer to the rotating  
frame.



## 2.4 Spin-echo techniques

In many cases, the transverse magnetization decays relatively rapidly because of the dephasing associated with the inhomogeneity of  $B_0$ . However, this dephasing is reversible whereas the dephasing associated with  $T_2$  is not. As was shown by Hahn (1950), the application of a  $\pi/2$ -pulse, followed at a time  $\tau$  later by a  $\pi$ -pulse, will give rise after a further time  $\tau$ , to a "free induction echo" which has been called a "spin-echo". The  $\pi$ -pulse rotates the spins in such a way that the dephasing that occurs during the first time interval  $\tau$  is reversed during the second  $\tau$  interval. In the absence of  $T_2$  processes, the transverse magnetization in the second interval builds up in the same fashion as the FID decayed in the first interval. After its formation, the echo decays in the same way as the FID. The echo "envelope" therefore looks like two FID signals back-to-back. In practice,  $T_2$  processes cause the echo amplitude to be smaller than the FID, the situation being as shown in Fig. 2. In this figure, it has been assumed that the phase of the  $\pi$ -pulse is shifted by  $90^\circ$  relative to the  $\pi/2$ -phase. Otherwise, if the pulses have the same phases, the echo would be inverted.

The technique was originally used to determine values of  $T_2$ . However, the spin-echo technique is being used to great advantage in NMR imaging, as will be shown in section 2.6.

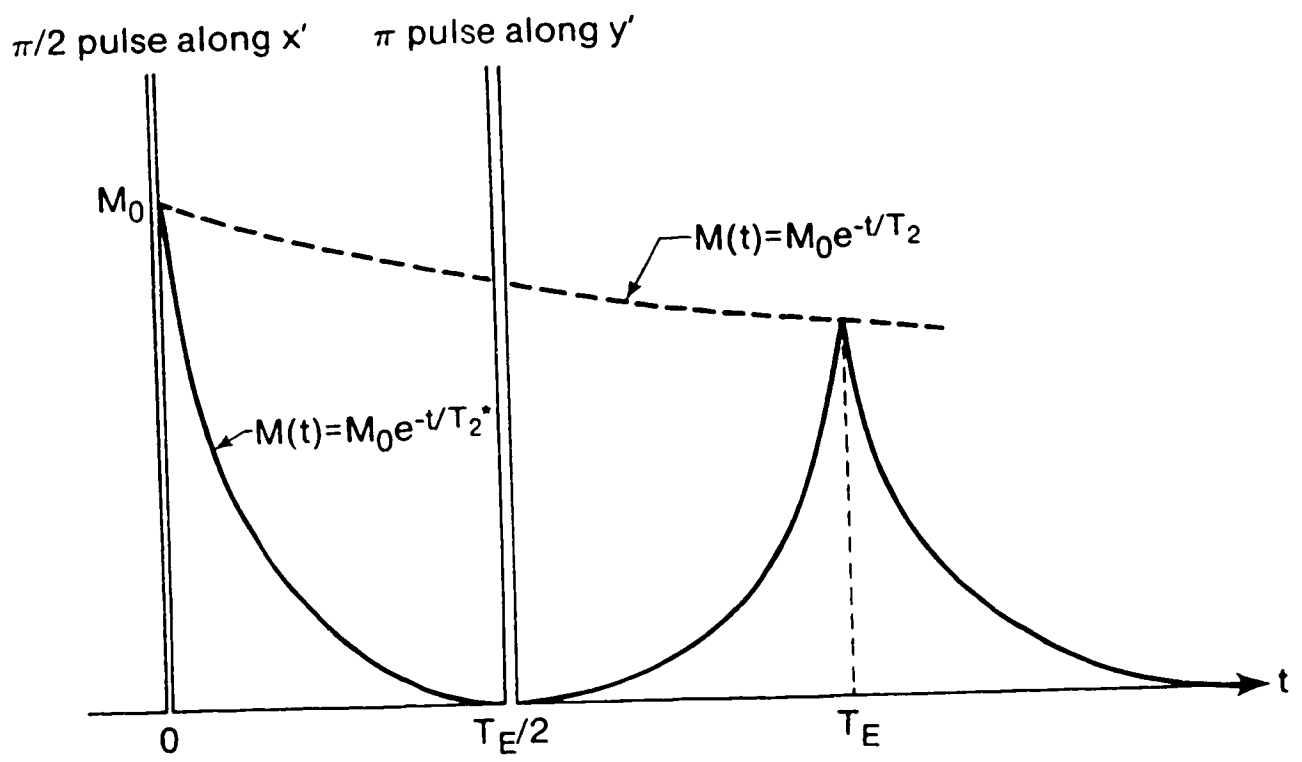
## 2.5 Detection of NMR

Two general methods of detection exist in NMR; continuous wave (cw), which is an older technique, and pulsed methods, which are used much more extensively today. In pulsed methods, a short intense rf pulse is applied to a coil, often called the transmitter coil, which is wound in such a way as to generate an rf magnetic field which is perpendicular to the static field. The linearly polarized rf magnetic field can be

Fig. 2

A spin-echo experiment. A  $\pi/2$ -pulse along the  $x'$  axis rotates the magnetization to the  $y'$  axis. The signal arising from this magnetization decays with a characteristic time  $T_2^*$ . At time  $T_E/2$ , a  $\pi$ -pulse is applied along the  $y'$  axis causing the magnetization to refocus at time  $T_E$ . The magnetization at time  $T_E$  is reduced from its initial value of  $M_0$  because of  $T_2$  processes which are not reversed by the  $\pi$ -pulse.





decomposed into two contra-rotating circularly polarized components, one of which rotates in the same sense as the nuclei and is the  $B_1$  field referred to above. If the rf pulse is extremely short so that it approximates a delta function, it will contain a wide band of frequencies which simultaneously irradiates the entire NMR spectrum.. The resultant precessing magnetization in the sample induces a voltage in the receiver coil. Often the same coil serves as both receiver and transmitter coils. The voltage induced in the coil decays because of the relaxation effects discussed in section 2.1 and the time-domain signal is called a free-induction decay ( FID ). It can be shown ( Slichter, 1963 ) that the Fourier transform of the FID gives the same frequency spectrum as that obtained using the cw technique, provided the rf pulse is short enough to uniformly excite the whole NMR spectrum.

To analyze the high frequency time domain signal resulting from the system of spins, phase sensitive detection is used. In phase sensitive detection, the input signal is multiplied by a reference signal at a frequency  $\omega_0$  which is usually close to the frequencies associated with the input signal. Components of the input signal at frequency  $\omega$  thus give rise to two components, with frequencies  $\omega + \omega_0$  and  $\omega - \omega_0$ . A low pass filter eliminates the high frequency signal. Using two phase sensitive detectors whose reference signals are in quadrature or out of phase by  $\pi/2$  radians, one may distinguish positive ( $\omega - \omega_0 > 0$ ) from negative ( $\omega - \omega_0 < 0$ ) frequencies. In many cases, the reference frequency  $\omega_0$  is chosen to be the same as the frequency of  $B_1$ . The output of the phase sensitive detectors will then give the frequencies as observed in the rotating frame. The use of two phase detectors in quadrature also has the advantage of improving the Signal to Noise ratio ( S / N ) by  $\sqrt{2}$ .

## 2.6 NMR imaging

Since the initial development of NMR imaging (MRI) in 1973, many techniques have been proposed and developed such as point, line, planar and three dimensional methods, projection reconstruction and the more common Fourier methods developed by Ernst et al. (1975). In MRI, a linear magnetic field gradient  $\vec{G} = \nabla B_z$  is applied to the sample in order to bring about spatial differentiation. The gradient field is parallel to  $B_0$  and is therefore along the  $z$  axis whereas the direction of the gradient is at the control of the experimenter. In practice,  $B_0$  is usually very much larger than the gradient field so that any  $x$  or  $y$  components which may be inadvertently generated will have a negligible effect. The  $z$  component of the magnetic field at a location  $\vec{r}$ , where  $\vec{r}$  is measured from the point where the gradient field is zero, is then given by

$$B_z(\vec{r}) = B_0 + \Delta B(\vec{r}) = B_0 + \vec{G} \cdot \vec{r}. \quad (15)$$

Thus the new resonance condition is

$$\omega(\vec{r}) = \gamma ( B_0 + \vec{G} \cdot \vec{r} ) \quad (16)$$

and the frequency offset from  $\omega_0$  of a group of spins is proportional to their distance away from the plane where the gradient field is zero.

To uniquely encode all locations in a sample, one requires three orthogonal field gradients. The  $z$ -gradient is normally generated using a Maxwell coil and the  $x$ -gradient and  $y$ -gradient are normally generated using Golay coils ( Morris, 1986 ).

Two dimensional Fourier imaging is currently the most common imaging modality and this thesis is concerned with intensity artifacts that arise using this technique. For this technique, one first "selects" a slice by rotating all of the spins in a thin slice from

the z-axis into the xy plane. Moreover, all the spins should have the same phase in the xy-plane. An ideal "top-hat" slice profile is one in which all the nuclei in the slice are rotated through  $\pi/2$  radians and have the same phase in the xy-plane while all the nuclei outside the slice are unaffected.

All spins in a slice can, in principle, be rotated through  $\pi/2$  radians by simultaneously applying a linear field gradient perpendicular to the slice and a tailored selective rf pulse which is a sinc function in the time domain. However, the excited nuclei will have a roughly uniform distribution of phases in the transverse plane (Morris, 1986). Also, the sinc function is impractical to implement because of the side-lobes. The first problem can be largely overcome by "unwrapping" the spins by applying a so-called "slice compensation" gradient pulse of suitable amplitude and duration but of opposite polarity after the rf-pulse has died away. The second problem can be overcome by sacrificing a top-hat slice profile and, using instead, a time-limited rf-pulse such as a Gaussian. If a Gaussian pulse is used, the slice profile will be roughly Gaussian in shape. It will not be exactly Gaussian because the Bloch equations are non-linear (Mansfield et al., 1979, Hoult, 1979). Once a slice normal to the z direction is selected, spatial encoding of x and y is achieved using the magnetic field gradients  $G_x$  and  $G_y$ .

For a one dimensional image, the sequence to encode the data would involve selecting a slice followed by the application of a frequency encoding or read gradient in a direction orthogonal to the slice direction and recording the resultant time-domain signal. A serious problem with this is the loss of NMR signal or dephasing which occurs during the finite rise time ( $\sim 2\text{ms}$ ) of the read gradient. This is overcome by using not one, but two read gradients of the same polarity and applying a "hard" (non-selective)  $\pi$ -pulse between the gradients to achieve refocussing of the signal in a "spin-echo" as shown in Fig. 3.

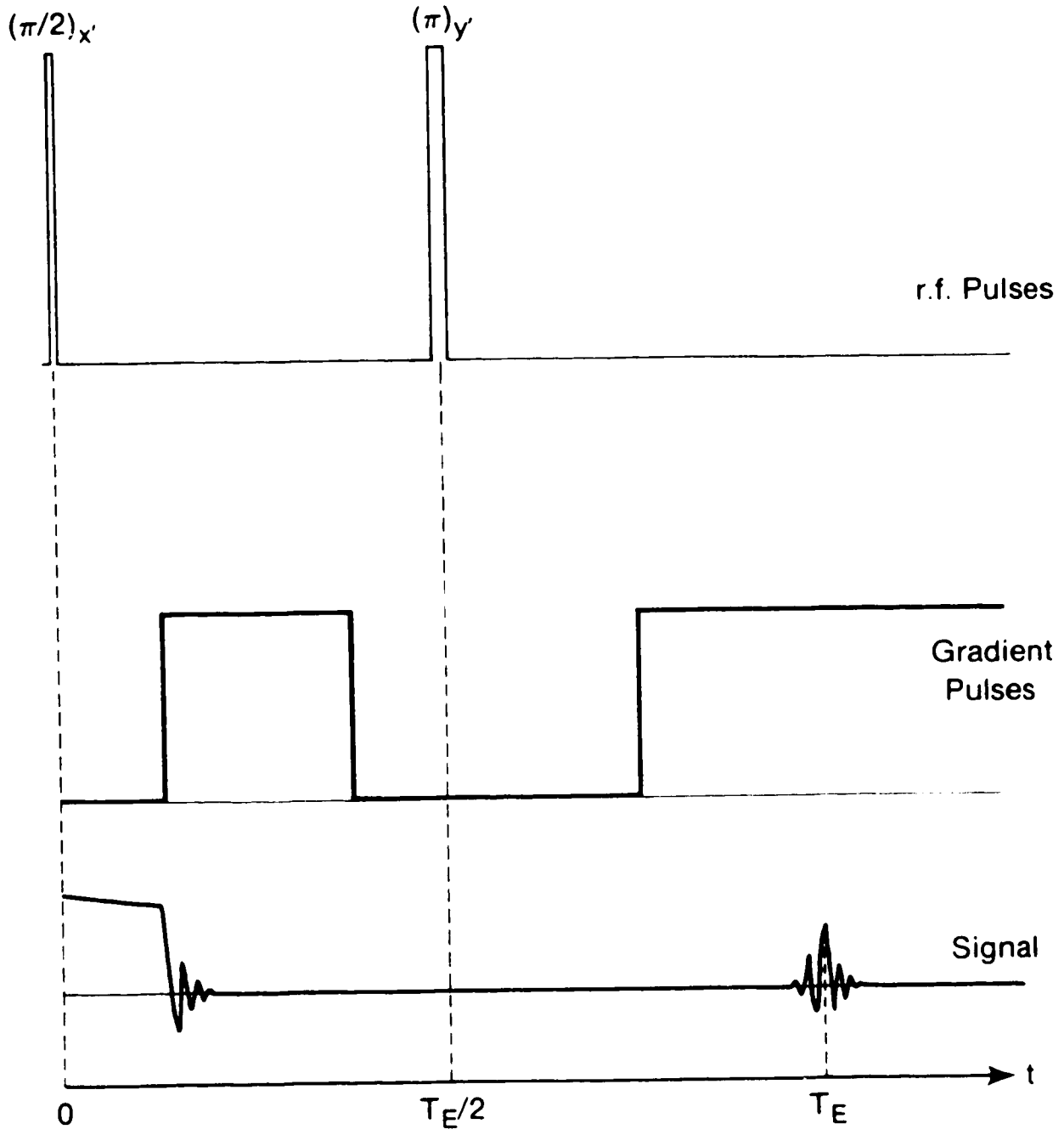
The first read gradient pulse, which is called the read compensation gradient, causes dephasing of the spins. The second gradient pulse, since it occurs after the  $\pi$ -pulse, causes rephasing of the spins, such that an echo forms at a time when the time-integrated areas under the two read gradient pulses are equal. The duration and strength of the read compensation gradient is chosen so that the echo forms well after the rise time of the second read gradient. The spin-echo signal is therefore formed in an essentially constant field gradient, as required. Fourier transformation of this spin-echo signal then gives a one-dimensional image or projection.

In practice, some additional dephasing of the spins will occur because of the inhomogeneity in the  $B_0$  field. As is well known from the spin-echo experiment (Farrar and Becker, 1971), the effect of the  $\pi$ -pulse applied at a time  $T_E/2$  after the initial excitation is to rotate the spins about the axis of the pulse in the rotating frame. This has the effect of causing the spins to refocus at a time  $T_E/2$  after the  $\pi$ -pulse, i.e. at a time  $T_E$  (echo-time) after the initial rf excitation. Thus, the loss of signal in the imaging procedure caused by the inhomogeneity of  $B_0$  can be largely eliminated by positioning the  $\pi$ -pulse midway in time between the initial rf excitation and the formation of the echo in the presence of the gradients.

To create a two-dimensional image, it is necessary to encode the signal in a direction orthogonal to the read ( $x$ ) direction and slice ( $z$ ) direction. This is done by applying a so-called "phase encoding" gradient between the time of the initial rf excitation and the time of the echo formation. Application of such a pulse of amplitude  $G_y$  and duration  $\tau$  changes the phase, by  $\gamma G_y y \tau$ , of the signal from nuclei in a plane whose  $y$  coordinate is  $y$ . By incrementing the amplitude of this pulse by a small amount, determined by the required resolution in the phase encoding direction, and repeating the imaging sequence for each increment, a two-dimensional image can be

Fig. 3

A spin-echo imaging experiment. Following a  $\pi/2$ -pulse along the  $x'$  axis which rotates the magnetization to the  $z$  axis, a read compensation gradient pulse is applied causing the individual spins which make up the net magnetization to dephase coherently. After a subsequent  $\pi$ -pulse along the  $y'$  direction, another read gradient pulse is applied which causes the spins to refocus to form an echo at time  $T_E$ .



obtained by two-dimensional Fourier transformation of the resultant time domain signals.

The minimum read gradient strength,  $(G_x)_{\min}$ , is determined by the static field inhomogeneity. The frequency range across one picture element (pixel) due to the gradient must be much larger than the field inhomogeneity expressed in frequency units. With this in mind, and knowing the maximum displacement  $L_x$  of the sample in the x-direction, the gradient strength  $G_x$  can be chosen. The maximum frequency in the signal,  $\nu_{\max}$ , will then be given by

$$\nu_{\max} = (\gamma G_x L_x) / 2\pi . \quad (18)$$

Once this frequency is known, the dwell time (DW) or the time between samplings during data acquisition can be determined using Nyquist's condition. This states that the maximum frequency to be correctly reproduced without aliasing will be

$$\nu_{\max} = 1 / (2 \times DW). \quad (19)$$

Thus, to prevent aliasing in the image, the condition

$$\gamma G_x L_x DW \leq \pi \quad (20)$$

must be met.

The number of sampled points  $n$  during the data acquisition interval determines the number of pixels in the x direction and thus the resolution. The acquisition time is given by  $\tau_{\text{aq}} = (n-1) \times DW$ . Since the data processing involves a Fast Fourier transform (Brigham, 1974), it is preferable that  $n$  be a power of two. The effect of D.C. offsets may be eliminated by repeating the pulse sequence with the phase of the



$\pi/2$ -pulse reversed ( i.e. the first  $\pi/2$ -pulse along  $+x'$  and the second along  $-x'$  ) and subtracting the two echoes. Also, of course, repeating each pair of pulse sequences will lead to an improved S/N.

The frequency response in the phase direction is determined by the phase gradient increment. The condition for this increment is that a spin located at the maximum phase displacement ( $\pm L_y$ ) will not be dephased when  $G_y = 0$  but will be dephased by  $\pi$  with no aliasing on the next increment. This leads to the condition

$$\gamma (G_y)_{\min} L_y t_y \leq \pi \quad (21)$$

where  $(G_y)_{\min}$  is the smallest non-zero phase gradient or the phase gradient increment and  $t_y$  is the duration of the phase gradient pulse.

A variation of this form of imaging is multiple echo imaging where additional echoes are created by placing another  $\pi$ -pulse after the echo and modifying the read gradient after the echo such that a second echo forms at the centre of the second acquisition and so on for the subsequent echoes. Each echo will be reduced in signal intensity due to natural  $T_2$  processes and the gradient areas would have to be very precisely adjusted to ensure that the echoes form at the centres of the acquisition periods. Also, three-dimensional imaging can be accomplished by eliminating the slice selection and incorporating another phase encoding step for that dimension. However, this is not very popular due to the longer experimental times required and the difficulty of displaying a three-dimensional image on conventional displays.

## CHAPTER 3

### IMAGE INTENSITY ARTIFACTS IN MRI

Image intensity artifacts can be caused by many different mechanisms. To simplify matters, intensity artifacts arising from imperfections in the slice selection and phase encoding procedures are not treated. This thesis, therefore, deals with intensity artifacts arising in one-dimensional spin-echo imaging which uses an initial non-selective  $\pi/2$ -pulse followed by a read compensation gradient pulse, a non-selective  $\pi$ -pulse and a read gradient pulse in that order (see Fig. 3).

#### 3.1 Intensity artifacts due to imperfections in the rf field $B_1$

A factor governing the accuracy of the intensity values in MRI is the spatial homogeneity of the rf or  $B_1$  field. If the strength of the  $B_1$  field varies throughout the sample, the tip angles experienced with a  $\pi$ -pulse and a  $\pi/2$ -pulse will vary throughout the sample. This will lead to intensity variations in the image which are not intrinsic to the sample.

#### 3.2 Intensity artifacts arising from the inhomogeneity of the steady magnetic field $B_0$

If the object or phantom to be imaged has a uniform number of spins per unit length in the read direction, the image should be a "top-hat" shape in the frequency domain with frequencies ranging from  $-f_1$  to  $f_1$ , say. The corresponding time domain signal is the inverse Fourier transform of this, viz. a sinc function with zeros every  $1/f_1$  seconds. In order for this sinc function to be faithfully sampled and recorded, the

echo envelope associated with the inhomogeneity in  $B_0$  should be essentially constant during the period when the echo is being formed. Otherwise, the wings of the sinc function will be attenuated and the Fourier transform of the echo will no longer be a top-hat shape. To avoid this kind of intensity distortion,  $T_2^*$  should be much greater than  $1/f_1$ . This condition is equivalent to the requirement that the linewidth  $\Delta\omega/2\pi$  associated with the inhomogeneity  $B_0$  shall be much less than the total width  $2f_1$  of the image. This requirement is usually stated in the form that the  $B_0$  inhomogeneity width in frequency units shall be less than the pixel (picture element) width.

### 3.3 Intensity artifacts associated with the use of a finite data acquisition period

The time domain signal associated with the top-hat frequency domain signal, viz. the sinc function, possesses side lobes which extend out to  $t = \pm\infty$ . The use of a finite data acquisition time,  $\tau_{aq}$ , truncates the signal at  $t = \pm\tau_{aq}/2$ . In effect, the true signal is multiplied by the top-hat function of width  $\tau_{aq}$ . By the convolution theorem, this implies that the observed image is the convolution of the true image shape with a sinc function of the form  $\text{sinc}(f\tau_{aq})$ . To obtain an accurate image intensity distribution,  $\tau_{aq}$  must obviously be chosen to be much larger than  $1/f_1$  defined in the previous section.

### 3.4 Intensity artifacts associated with dielectric resonances

Roschmann et al. (1988) have recently observed image intensity variations which they attribute to dielectric resonances (Gastine et al., 1965). These resonances give rise to a spatial inhomogeneity in the amplitude of the rf magnetic field in the sample, thereby causing variations in the image intensity. This effect is worse at high frequencies and for samples with a high dielectric constant.

### 3.5 Intensity artifacts associated with non-ideality of the gradient pulses

In order to understand intensity artifacts associated with imperfections in the gradient pulses, it is necessary to discuss problems caused by the use of pulsed gradients. These are discussed in section 3.5.1. Artifacts which stem from these are discussed in sections 3.5.2 to 3.5.4.

#### 3.5.1 Generation of pulsed magnetic field gradients: eddy currents

The coils used to generate the magnetic field gradients are inductive and therefore have a finite rise and fall time given by the ratio  $L/R$  where  $L$  and  $R$  are, respectively, the inductance and resistance of the coil. In practice,  $L/R$  is of the order of 1ms. It is important that the gradients are turned on and off rapidly so that the imaging sequence can be carried out as quickly as possible. A faster rise and fall time than that implied by the  $L/R$  ratio can be achieved by shaping the voltage pulse so that it has a large positive value immediately after switch-on and a large negative value immediately after switch off for a positive gradient voltage pulse. This approach is called "pre-emphasis" but its use is limited by the available driving power.

The rapid change in the gradient field that occurs during switch on and switch off induces eddy currents in nearby metallic components, the effect being particularly prominent in superconducting as opposed to resistive magnets. The eddy currents will in turn produce magnetic fields which are superimposed on the main gradient fields. Because of the relatively large  $L$ 's and small  $R$ 's of the eddy current loops in the cryostat of a superconducting solenoid, these spurious magnetic fields may take a long time to decay. Moreover, they may be characterized by several different decay times.

If the cryostat is approximately cylindrically symmetric, the eddy currents will generate a fairly uniform field gradient of opposite sign to the gradient produced by the current in the gradient coil. It is possible to compensate the slowly decaying gradient caused by such eddy currents by suitably shaping the waveform of the current in the gradient coils. In practice, perfect compensation cannot usually be achieved because of the large number of different decay time constants associated with the different eddy current loops. Moreover, the cryostat is not usually perfectly cylindrically symmetric, so the eddy currents may generate a magnetic field in addition to a magnetic field gradient. This magnetic field cannot be expected to be perfectly homogeneous.

Mansfield (1986) has suggested a method for reducing these eddy fields by "active-screening". His idea is based on the fact that if a conducting cylinder of suitable thickness were placed around the gradient coils, any alternating magnetic field outside the cylinder would be zero. He approximates the screening cylinder with wires placed at various positions around the gradient coil. The position, the wires and the amplitudes of the currents flowing through them are such as to approximate the currents that would be induced in the conducting screen during gradient switchings. The currents through the screening wires would cancel the external fields due to the main gradient coils. The field at the parts of the cryostat which formerly had eddy currents induced in them would remain virtually unaffected by the gradient pulse, so little eddy current would be generated.

Another method used to reduce the effects of eddy currents is to try to isolate the gradient coils from materials such as the cryostat. This can be done by having smaller gradient coils. However, it has the disadvantage of reducing the volume over which images can be made because of the reduced volume over which the gradient fields are linear.

### 3.5.2 Intensity artifacts arising from the finite decay time of the read compensation gradient pulse

If the  $\pi$ -pulse is applied too soon after the read-compensation gradient is switched off, the extremities of the sample in the read direction will be far off-resonance because of the finite decay time of the gradient pulse. This will result in tip angles greater than  $\pi$  radians about axes tilted away from the  $y'$  axis in the  $y'z'$  plane, if  $B_1$  is along the  $y'$  axis, as discussed in section 2.3. This causes a loss of transverse magnetization by two mechanisms. Firstly, part of the transverse magnetization is rotated by the " $\pi$ -pulse" ( i.e. by an on-resonance  $\pi$ -pulse ) into the  $z'$  direction. Secondly, because of inhomogeneity of the  $B_0$  field in a direction orthogonal to the gradient field, nuclei lying along an isochromat will possess different phases at the time of the " $\pi$ -pulse". Such nuclei will experience different rotations as a result of the " $\pi$ -pulse". Thus, destructive interference will occur because of an imperfect refocussing of the spins at time  $T_E$  leading to a loss of signal intensity near the extremities of the sample.

If at some position,  $\vec{r}$ , the additional field in the  $z$  direction experienced by the spins due to the decay of the gradient is  $\Delta B$ , then, in the rotating frame, the effective field during the " $\pi$ -pulse" with  $B_1$  along the  $y'$  axis is given by ( Farrar and Becker, 1971 )

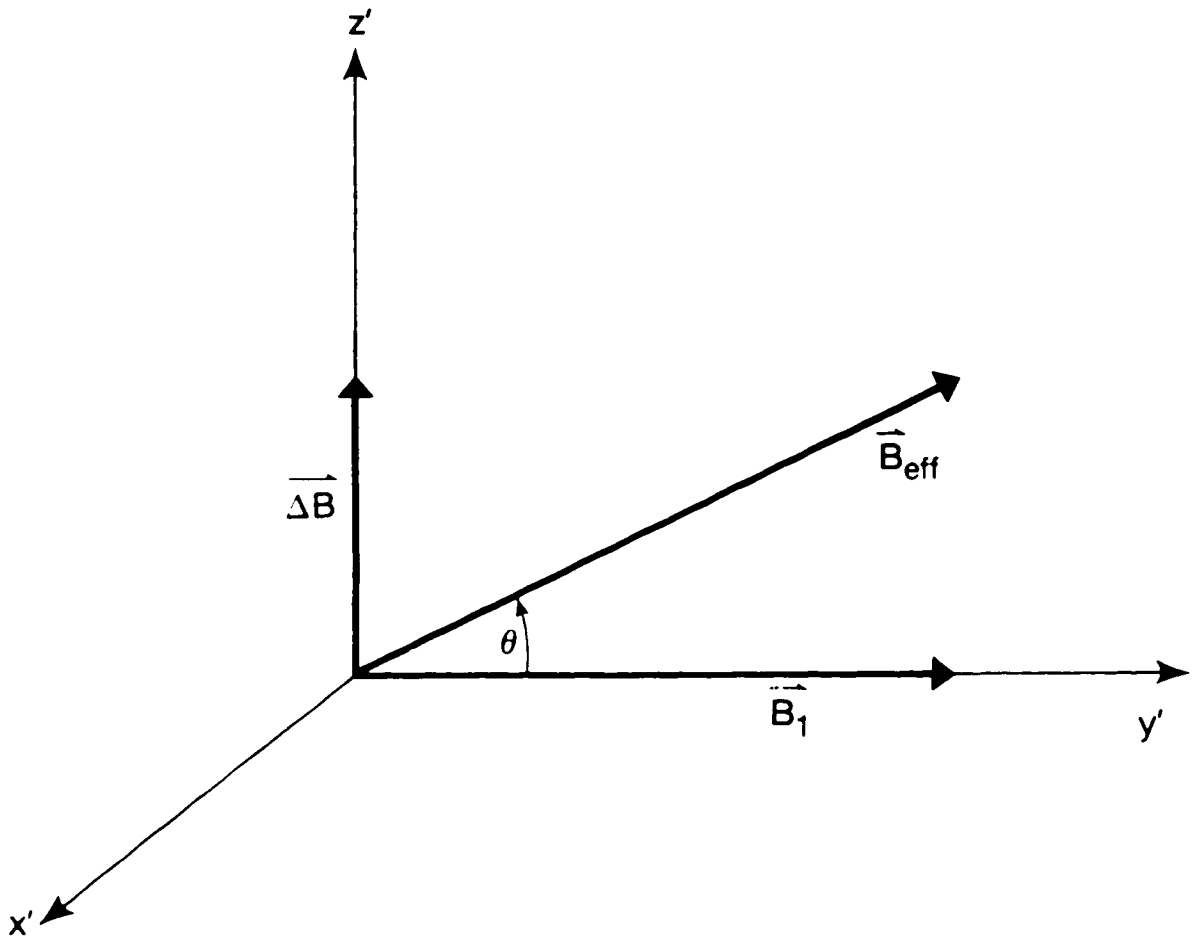
$$B_{\text{eff}} = ( B_1^2 + \Delta B^2 )^{1/2}. \quad (22)$$

As shown in Fig. 4,  $B_{\text{eff}}$  will be oriented at an angle  $\theta$  to the  $y'$  axis in the  $y'z'$  plane given by

$$\theta = \tan^{-1} ( \Delta B / B_1 ). \quad (23)$$

Fig. 4

The magnetic field  $\vec{B}_{\text{eff}}$  in the rotating frame experienced by a system of nuclei.  $\vec{B}_{\text{eff}}$  is the vector sum of the rf magnetic field,  $\vec{B}_1$ , and the offset magnetic field,  $\Delta\vec{B}$ , due to the decay of the gradient pulse.





The angle of rotation  $\phi$  about  $B_{\text{eff}}$  for a " $\pi$ -pulse" of duration  $\tau$  is given by

$$\begin{aligned}\phi &= \gamma B_{\text{eff}} \tau = \gamma (B_1^2 + \Delta B^2)^{1/2} \tau \\ &= \gamma B_1 \tau (1 + (\Delta B / B_1)^2)^{1/2} \\ &= \pi (1 + (\Delta B / B_1)^2)^{1/2}.\end{aligned}\quad (24)$$

Consider a group of spins with transverse magnetization  $\vec{M}_0$  situated at a position  $\vec{r}$ . As a result of the dephasing arising from the inhomogeneity in  $B_0$  and the read compensation gradient pulse, the magnetization  $\vec{M}_0$  will be oriented at an angle  $(\pi/2 - \beta)$ , say, with respect to the  $x'$  axis immediately prior to the " $\pi$ -pulse". This magnetization can be resolved into components  $M_0 \sin\beta$  along the  $x'$  axis and  $M_0 \cos\beta$  along the  $y'$  axis.

To determine what happens to the  $y'$  component,  $M_0 \cos\beta$ , as a result of the " $\pi$ -pulse", one can simply use the expressions developed by Mansfield et al. (1979). Their result was for an initial magnetization along  $z'$  followed by an rf pulse with a  $B_{\text{eff}}$  at an angle  $\theta$  from the  $z'$  axis in the  $z'x'$  plane. After suitable transformation of axes to correspond to our case, the magnetization after a " $\pi$ -pulse" is given by

$$M_{x'} = M_0 \cos\beta \{ \sin\theta \sin\phi \} \quad (25a)$$

$$M_{y'} = M_0 \cos\beta \{ \cos^2\theta + \sin^2\theta \cos\phi \} \quad (25b)$$

$$M_{z'} = M_0 \cos\beta \{ \sin\theta \cos\theta (1 - \cos\phi) \}. \quad (25c)$$

To determine what happens to the  $x'$  component,  $M_0 \sin\beta$ , one can simply transform to another rotating frame,  $\Sigma''$ , with the  $x''$  axis coincident with the  $x'$  axis and the  $y''$  axis along the direction of  $B_{\text{eff}}$ . The magnetization in this frame after the " $\pi$ -pulse" is given by

$$M_x'' = M_0 \sin\beta \cos\theta \quad (26a)$$

$$M_y'' = 0 \quad (26b)$$

$$M_z'' = M_0 \sin\beta \sin\theta. \quad (26c)$$

To find the magnetization in the original rotating frame resulting from the original  $x'$  magnetization  $M_0 \sin\beta$ , one simply transforms this magnetization back giving

$$M_x' = M_x'' = M_0 \sin\beta \cos\theta \quad (27a)$$

$$M_y' = -M_0 \sin\beta \sin\theta \sin\theta \quad (27b)$$

$$M_z' = M_0 \sin\beta \sin\theta \cos\theta. \quad (27c)$$

The resultant transverse magnetization immediately after the " $\pi$ -pulse",  $(M_{x'y'})_{\text{after}}$ , can be found by determining the new magnetization for each component  $M_0 \cos\beta$  along  $y'$  and  $M_0 \sin\beta$  along  $x'$  and adding them vectorially. The new  $x'$  and  $y'$  magnetization components are given by

$$(M_{x'})_{\text{after}} = M_0 (a \sin\beta + b \cos\beta) \quad (28a)$$

$$(M_{y'})_{\text{after}} = M_0 (c \cos\beta - b \sin\beta) \quad (28b)$$

where  $a = \cos\theta$ ,  $b = \sin\theta \sin\theta$  and  $c = \cos^2\theta + \sin^2\theta \cos\theta$ . The transverse magnetization immediately after the " $\pi$ -pulse" is therefore given by

$$(M_{x'y'})_{\text{after}} = M_0 \{ (a \sin\beta + b \cos\beta)^2 + (c \cos\beta - b \sin\beta)^2 \}^{1/2} \quad (29)$$

oriented at an angle  $-\beta'$  from the  $y'$  axis given by

$$\begin{aligned}\beta' &= \tan^{-1} \left\{ (M_x')_{\text{after}} / (M_y')_{\text{after}} \right\} \\ &= \tan^{-1} \left\{ (a \sin\beta + b \cos\beta) / (c \cos\beta - b \sin\beta) \right\}. \quad (30)\end{aligned}$$

The final phase angle at time  $T_E$  will then be given by  $\beta' + \beta$  since the spins will continue to precess about the  $z'$  axis at the same rate as before the " $\pi$ -pulse". By substitution of  $\theta = 0$  radians and  $\phi = \pi$  radians in the above equations, corresponding to the on-resonance condition, we see that  $(M_x'y')_{\text{after}}$  is  $M_0$  and the accumulated phase angle  $\beta' + \beta$  is zero at time  $T_E$ , as expected. However, if the " $\pi$ -pulse" is not on-resonance,  $(M_x'y')_{\text{after}}$  will be less than  $M_0$  and  $\beta' + \beta$  will not be zero. Since the accumulated phase angle is not zero for the off-resonance condition but depends on the initial angle  $\beta$  and the offset  $\Delta B$ , the spins along an isochromat which experience different magnetic fields due to the inhomogeneity in  $B_0$  (and thus have different  $\beta$ 's) will not be in phase at time  $T_E$ .

To obtain an expression for the net transverse magnetization at time  $T_E$ , it is necessary to know the distribution of the phase angles  $\beta$ . If the transverse magnetization is zero at the time of the " $\pi$ -pulse", as is usually the case, the spins can be assumed to have a uniform distribution of phase angles  $\beta$ . In that case, the net component magnetizations at time  $T_E$ ,  $(M_x')_{T_E}$  and  $(M_y')_{T_E}$ , are given by the following integrals:

$$\begin{aligned}(M_x')_{T_E} &= 1/2\pi \int_0^{2\pi} M_0 \left\{ (a \sin\beta + b \cos\beta)^2 + (c \cos\beta - b \sin\beta)^2 \right\}^{1/2} \times \\ &\quad \sin(\beta' + \beta) \, d\beta \quad (31a)\end{aligned}$$

$$\begin{aligned}(M_y')_{T_E} &= 1/2\pi \int_0^{2\pi} M_0 \left\{ (a \sin\beta + b \cos\beta)^2 + (c \cos\beta - b \sin\beta)^2 \right\}^{1/2} \times \\ &\quad \cos(\beta' + \beta) \, d\beta. \quad (31b)\end{aligned}$$

The final transverse magnetization is then given by

$$(M_{x'y'})_{TE} = \{ (M_x')^2_{TE} + (M_y')^2_{TE} \}^{1/2}. \quad (32)$$

It is not easy to solve for  $(M_{x'y'})_{TE}$  using the above expressions. We therefore make the simplifying assumption that one quarter of the spins are aligned along each of the  $x'$ ,  $-x'$ ,  $y'$  and  $-y'$  directions immediately prior to the " $\pi$ -pulse". If the " $\pi$ -pulse" is on-resonance, the spins in the  $x'$  and  $-x'$  directions will be rotated to the  $-x'$  and  $x'$  directions respectively such that at time  $T_E$ , they will have rephased to the  $y'$  direction. Spins along the  $y'$  and  $-y'$  directions will be unaffected by the " $\pi$ -pulse" and both groups will have rotated to lie along the  $y'$  axis at time  $T_E$ . Thus, as expected, the net magnetization at time  $T_E$  will be  $M_0$  along the  $y'$  axis. However, as has already been shown, if the " $\pi$ -pulse" is not on-resonance, transverse magnetization will be lost.

To determine the remaining transverse magnetization for this case, first consider the magnetizations in the  $x'$  and  $-x'$  directions immediately prior to the " $\pi$ -pulse". Their rotations will be given by equations 27a through 27c with  $\beta = \pi/2$  and  $3\pi/2$  radians respectively and with  $M_0$  replaced by  $M_0/4$ . After the " $\pi$ -pulse", the spins will continue to precess such that they will be aligned at time  $T_E$  with a transverse magnetization of  $(M_0/2) (a^2 + b^2)$  oriented at an angle  $\beta' + \beta = \pi/2 + \tan^{-1} \{ -a / b \}$  from the  $y'$  axis. Secondly, consider the magnetizations which lie along the  $y'$  and  $-y'$  directions immediately prior to the " $\pi$ -pulse". Their rotations will be given by equations 25a through 25c with phase angle  $\beta = 0$  and  $\pi$  radians respectively. After the " $\pi$ -pulse", they will rephase at time  $T_E$  with a transverse magnetization of  $\{ (M_0/2) (b^2 + c^2) \}$  oriented at an angle  $\beta' + \beta = \tan^{-1} ( b / c )$  from the  $y'$  axis.

The net result at time  $T_E$  of these rotations of the four component magnetizations is

$$(M_x')_{TE} = 2 [ (-M_0/4) b + (M_0/4) b ] = 0 \quad (33a)$$

$$(M_y')_{TE} = 2 [ (-M_0/4) a + (M_0/4) c ] = \{ (M_0/2) (c - a) \}. \quad (33b)$$

Since  $(M_x)_{TE} = 0$ , the net transverse magnetization,  $(M_{x'y'})_{TE}$ , is equal to  $(M_y)_{TE}$ . A graph of the normalized transverse magnetization against  $\Delta B/B_1$  at time  $T_E$  calculated using equation 33b is shown in fig 5.

### 3.5.3 Effect of phase shifts caused by eddy currents

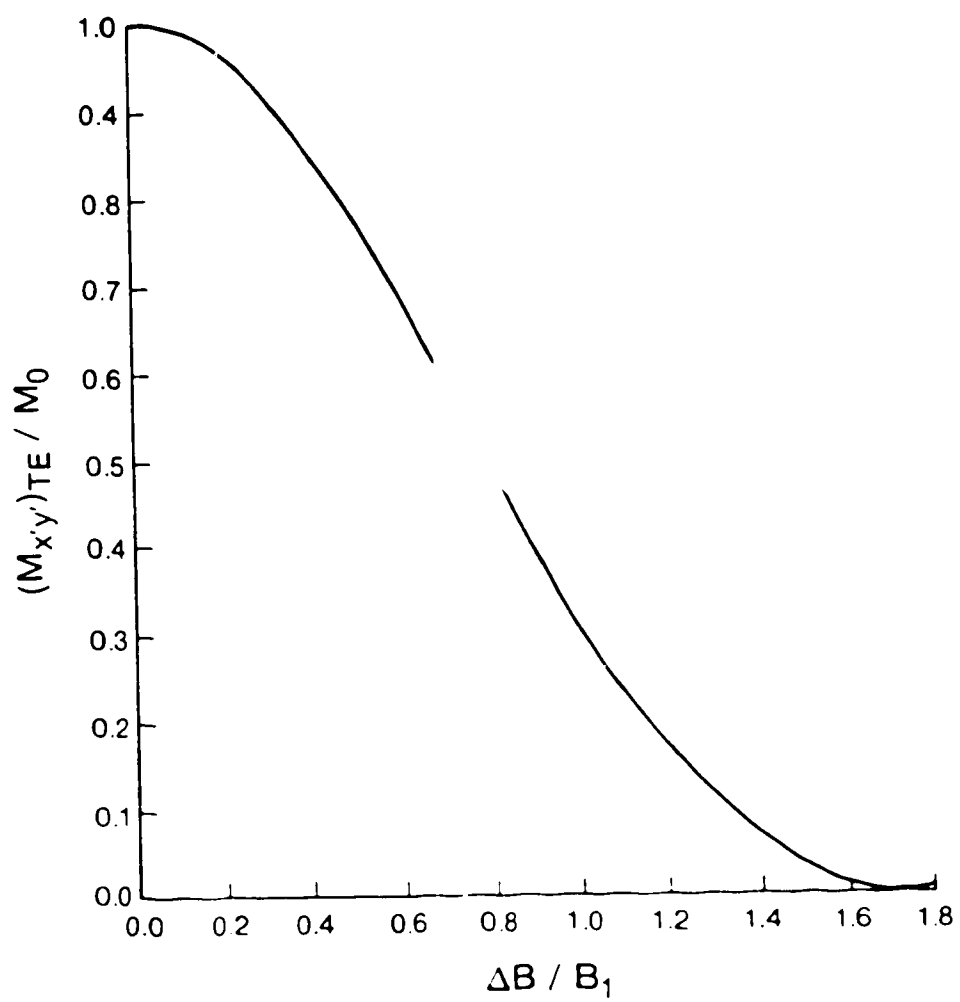
If the read gradient is in the x direction, then all nuclei in a thin slice perpendicular to the x direction should have the same precessional frequency during the data acquisition period. However, as has been pointed out already, eddy currents will, in general, produce a magnetic field across the sample in addition to a magnetic field gradient. If the magnetic field generated by the eddy currents is inhomogeneous, particularly in the y direction, then nuclei in the thin slice will have experienced different phase shifts prior to the data acquisition period. There will in that case be an intensity loss due to destructive interference.

### 3.5.4 Effect of improper refocussing of the spin echo signal

Eddy currents can cause intensity loss by yet another mechanism. The function of the read compensation gradient in a spin echo sequence is, as stated earlier, to dephase the spins in the read direction such that, after the application of a  $\pi$ -pulse, the reapplication of a read gradient of the same polarity will cause the spins to refocus at the same instant that the phase shifts due to the inhomogeneity in  $B_0$  are compensated by refocussing. The condition for this to occur is that the area under the read compensation gradient pulse must be equal to the area under the read gradient pulse measured up to the centre of the echo. However, the areas under the two gradient pulses include the contributions of the eddy currents to the field gradients. If the field

Fig. 5

The normalized transverse magnetization  $(M_{x'y'})_{TE} / M_0$  plotted as a function of  $\Delta B/B_0$ , where  $\Delta B$  is the offset field in the z direction due to the decay of the gradient pulse and  $B_1$  is the amplitude of the rf field. This curve was calculated assuming that the magnetization at the time of the " $\pi$ -pulse" was distributed with  $M_0/4$  along each of the  $x'$ ,  $y'$ ,  $-x'$  and  $-y'$  directions.



gradient produced by the eddy currents uniform throughout the sample, then one should be able to adjust the gradient pulses so that the echoes from all regions form at the same time. However, this will not be the case in general. For example, if the eddy currents produce an inhomogeneous magnetic field, then each region will require a different amount of compensation. Thus, the echoes from different regions will refocus at different times during the acquisition period.

In the absence of gradient pulses, an echo will still form at  $T_E$  because the phase shifts caused by inhomogeneities in the static field will be "unwrapped" by the  $\pi$ -pulse and the subsequent evolution in time of the spin system. If the static field inhomogeneity is large, this "echo envelope" will be short lived in the time domain since the spins will rapidly come into and out of phase near the centre of the echo. If this condition exists when the gradients are incorporated into the imaging sequence, great care must be taken to ensure that the echo forms at the centre of the acquisition period, which is where the echo envelope will refocus due to  $B_0$  inhomogeneity. Any slight misadjustment of either gradient pulse will cause the echo to refocus at some other time than  $T_E$  meaning that the echo envelope will not be at its maximum amplitude. Since the eddy currents cause the echoes from different regions to form at different times, intensity variations will result with greater distortion resulting from a sharper echo envelope. More precisely, an inhomogeneity in  $B_0$  along a line of constant spatial coordinate corresponding to the read direction will lead to an echo envelope with the net envelope being a summation of these individual envelopes. Variations in echo envelope sharpness and in echo reformation time in the presence of gradients for the nuclei along these lines of constant read coordinate will lead to intensity variations at the particular read coordinate.



## CHAPTER 4

### EXPERIMENTAL DETAILS

#### 4.1 Description of the NMR hardware

All of the measurements described in this thesis were carried out using a 2.35 T, 40 cm bore superconducting solenoid. This system is used by several research groups at the University of Alberta for *in vivo* imaging and spectroscopic studies on small animals. Field gradients are generated by means of Maxwell and Golay coils with an inner diameter (ID) of 35 cm placed in the magnet bore. NMR signals are obtained using a single rf coil which is a modified birdcage type (Hayes et al., 1985). This has an ID of 23 cm and is situated within the gradient coil former.

The rf transmitter and receiver systems, gradient power supplies, control units, superconducting solenoid and computing equipment were manufactured by the Bruker Co. of West Germany.

#### 4.2 NMR samples

The intensity artifacts were studied using a square slice phantom, with inner dimensions of 10 cm x 10 cm x 3 mm, filled with the water. The water was doped with  $\text{CuSO}_4$  to give a 5 mMolar concentration of  $\text{Cu}^{++}$ . The paramagnetic  $\text{Cu}^{++}$  ions reduce the  $T_1$  of the protons from 3 s to about 200 ms, thereby allowing shorter repetition times between successive scans.

The field variations, both spatial and temporal, following switch off of the gradient pulses were measured using a small spherical sample of doped water with a diameter of 13 mm.

### 4.3 Set-up procedure

The following procedures were followed at the beginning of each experimental session. They are similar to those used routinely by other researchers who use the system for imaging.

After the sample was placed in the magnet, the variable capacitors associated with the rf coil were adjusted such that the rf coil circuit was tuned and matched to allow for maximum power transfer and S/N ratio. The static magnetic field,  $B_0$ , was then "shimmed" to achieve the best possible field homogeneity over the sample. This was done by adjusting the magnitude of currents passing through various shim coils. These are designed to create linear and higher order tesseral and zonal harmonics of the centre of the magnet ( Romeo and Hoult, 1984 ). For our experiments, currents through the linear shim coils were adjusted in order to obtain a maximum area "under" the FID signal. The non-linear shims were left as set by the technician in charge.

After shimming, an FID was recorded and Fourier transformed. The resonance frequency was then set to be the frequency at the centre of the resulting peak. This peak is narrow for an optimum shim and roughly Gaussian in shape.

The  $\pi$ -pulse and the  $\pi/2$ -pulse were then adjusted. This was done by setting the duration of the  $\pi$ -pulse, called D1, to 300  $\mu\text{s}$  and then adjusting the gain of the transmitter rf amplifier such that after an rf pulse of duration D1, no signal could be observed. A  $\pi/2$  pulse would then result for an rf pulse of duration 150  $\mu\text{s}$  since the area under an rf pulse of such a duration is almost exactly proportional to its duration.

The method used on this system to compensate for the finite rise and decay times of the gradient pulses and the eddy currents is to pre-emphasize the gradient pulses, as was discussed in section 3.5.1. However, this procedure was only done once every few months. First, a large spherical water phantom ( ~10 cm diameter ) was placed in

the centre of the magnet and the static field was shimmed. The resonance frequency was also set, as discussed above. A gradient pulse of 10 ms duration was then applied followed by a variable delay and a non-selective  $\pi/2$  pulse of duration 150  $\mu$ s. If the gradient field dropped to zero immediately upon switch-off, the FID emanating from the phantom would be on-resonance and decay according to  $T_2^*$ . However, the gradient pulses take some time to decay because of the natural L/R decay time of the coil and the presence of long-lasting eddy currents. Thus, the FID emanating from the sample will have frequencies which are varying in time and will not return to the original resonance frequency until the eddy currents have decayed away. Following a 50  $\mu$ s delay after the  $\pi/2$ -pulse to allow the  $B_1$  field to decay, the FID was sampled and recorded. The experiment was then repeated but this time without applying the gradient pulse. Subtraction of the two FID signals gave a measure of the lingering effect of the gradient pulse.

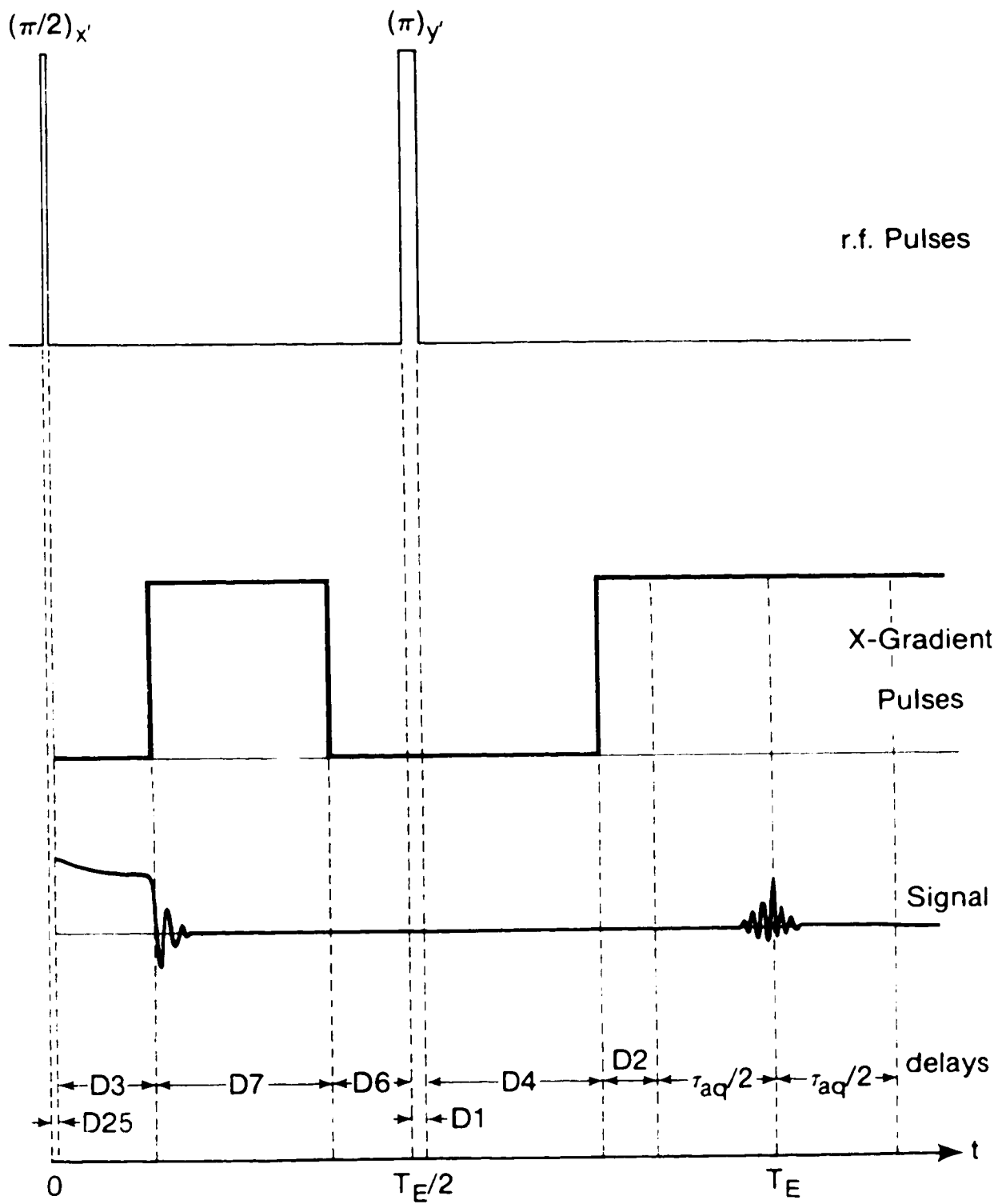
This procedure was repeated many times while varying the delay D5 from 5 ms to 500 ms and while varying the three time constants and gains in the pre-emphasis unit ( cf. section 3.5.1 ). The optimum settings were obtained when the observed difference between the two FID's was minimized.

#### 4.4 Pulse program and phantom set-up used to acquire projections

A schematic diagram of the pulse program, SRPP.PC, used to acquire the one-dimensional images or projections is shown in Fig. 6. After a delay of D3 following a non-selective  $\pi/2$ -pulse of duration D25 in the  $x'$  or  $-x'$  direction, the read compensation gradient is switched on for a duration D7. Following this, there is a delay of D6, a non-selective  $\pi$ -pulse of duration D1, a delay of D4, a read gradient of duration D2 followed by the acquisition period during which the gradient remains on, in that order. These times are chosen so that the  $\pi$ -pulse occurs midway between the

Fig. 6

Schematic diagram of the pulse program SRPP.PC used to generate projections of the slice phantom. The signal is acquired over a time from  $T_E - \tau_{aq}/2$  to  $T_E + \tau_{aq}/2$ .



$\pi/2$ -pulse and the centre of the acquisition period. This ensures that the echo envelope is situated at the centre of the acquisition period. The data points are acquired in both the real and imaginary channels of the phase sensitive detector with a sampling period DW given by

$$DW = 1 / ( 2 * SW ) \quad (34)$$

where SW is the sweep or spectral width. For our projection experiments, an SW of 20,000 Hz was used giving a DW of 25  $\mu$ s. The total acquisition time,  $\tau_{aq}$ , is given by

$$\tau_{aq} = SI * DW \quad (35)$$

where SI is the size or number of data points collected in one acquisition period. For these projection experiments, an SI of 512 was used corresponding to a  $\tau_{aq}$  of 12.8 ms.

The slice phantom was positioned as close to the isocentre of the magnet as possible. It was aligned in the xy plane perpendicular to the magnetic field with its edges aligned along the x ( vertical ) and y ( horizontal ) directions.

Projections were acquired with either of two values for D7, the duration of the read compensation gradient. The first value, D7 = 5 ms, was chosen because this is the value in the standard imaging sequence used by local researchers. The second value, D7 = 25 ms, was chosen because it is a longer duration similar to those used for some flow imaging techniques.

For D7 = 5 ms, D3 was set to 5 ms and D2 to 2 ms. The read gradient strength, expressed in frequency units, was set to roughly -1000 Hz/cm, about 20% of the maximum rating for the x gradient coil. The strength of the read compensation

gradient was adjusted ( to be roughly  $-1380 \text{ Hz / cm}$  ) until the echo formed at the centre of the acquisition period with D6 set to 5 ms and D4 set to 6.6 ms. This ensured that the echo formed at the centre of the echo envelope. This process is known as "trimming".

Phase cycling was accomplished by performing two scans, one with the  $\pi/2$ -pulse along  $x'$  and the other along  $-x'$ . Subtraction of the two FID's removes the D.C. offset.

For  $D7 = 25 \text{ ms}$ , the various durations were  $D3 = 12 \text{ ms}$ ,  $D6 = 20 \text{ ms}$ ,  $D4 = 20.7 \text{ ms}$  and  $D2 = 29.9 \text{ ms}$ . D1 and D25 were left unchanged. In this case, the trimming was done by adjusting the durations D4 and D2 until the echo was centered, keeping  $D2 + D4$  constant such that the echo envelope remained in the centre of the acquisition period.

#### 4.5 Pulse program and set-up to study eddy field decays

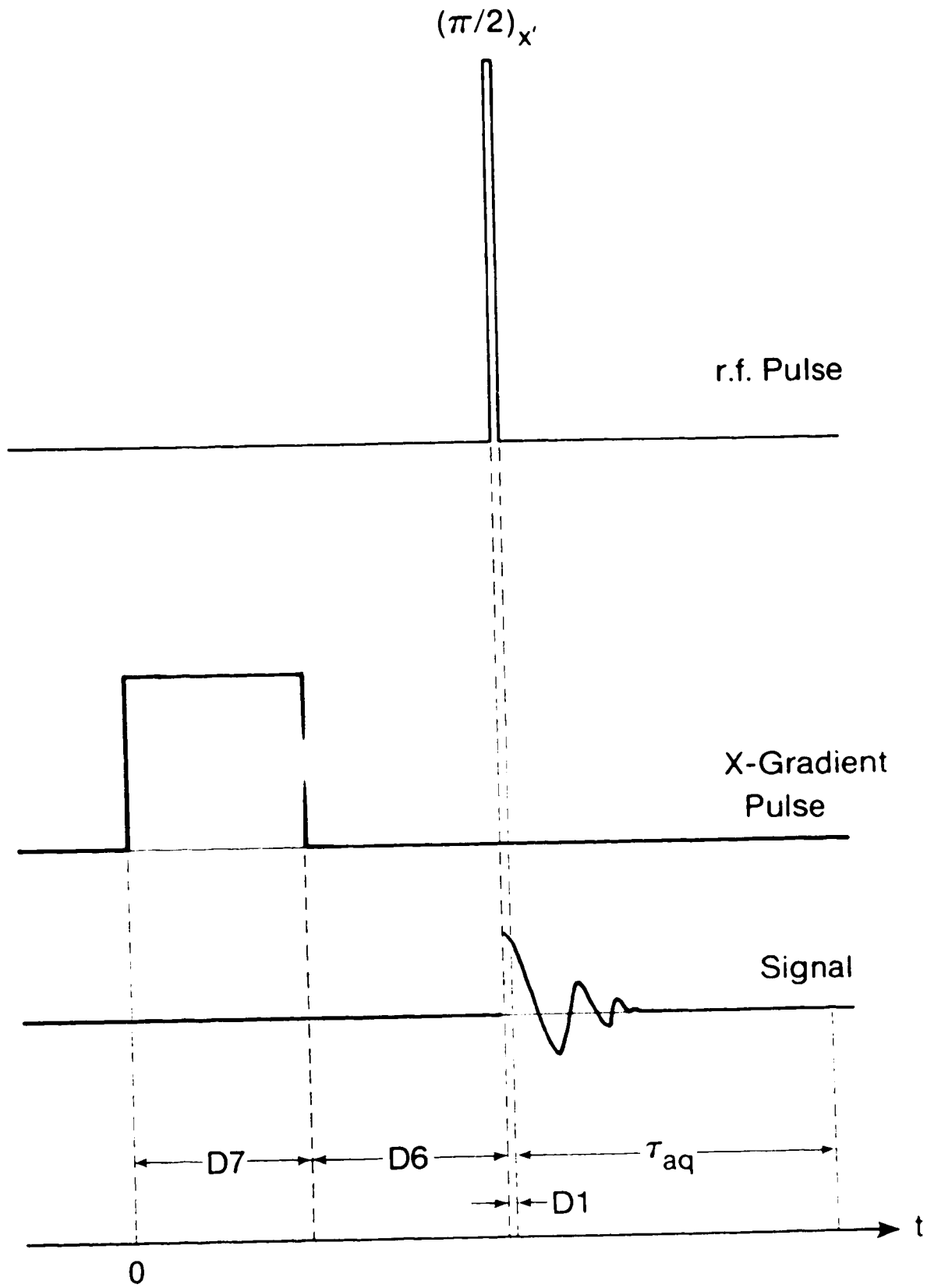
The field and field gradients caused by the eddy currents over the region occupied by the slice phantom were studied using the small spherical sample as a probe. A schematic diagram of CHECPM.PC, the pulse program used for these measurements, is shown in Fig. 7. A gradient was switched on for a duration D7 followed by a delay D6 and then a  $\pi/2$ -pulse of duration  $D1 = 150 \mu\text{s}$ , and an acquisition period,  $\tau_{\text{aq}}$ , in that order. The gradient strength, in frequency units, was set to  $-1380 \text{ Hz / cm}$ , corresponding to the strength of the read compensation gradient used in the projection experiments.

The observed signal was essentially a damped sine wave whose frequency, which we refer to as the offset frequency, is the difference between the actual resonance frequency and the resonance frequency in the absence of the gradient field and the eddy currents. In order to accurately measure the offset frequency, it is important to

**Fig. 7**

Schematic diagram of the pulse program **CHECPM.PC** used to measure the decay of the magnetic field after the switch-off of a gradient pulse.





choose appropriate values for the acquisition period and dwell time. When the offset frequency is high, a short acquisition period with a short dwell time allows many complete cycles to be sampled. On the other hand, if the offset frequency is close to zero, then a longer acquisition period is desirable. Also, in order to measure very low frequencies, it is advantageous to shift the detector reference frequency so that several complete cycles of the signal can be observed in a short time. In practice, the frequency was shifted by  $\pm 200$  Hz. The offset frequencies were found by measuring the period of one complete cycle. The time from the gradient switch-off was taken to be the sum of the delay D6 plus the time at the mid-point of the oscillation measured from the beginning of the FID.

The offset frequency was determined as a function of time at various locations in the magnet.

#### 4.6 Dielectric resonances

To determine if image intensity artifacts were caused by the dielectric resonance effect (Gastine et al., 1967, Roschmann et al., 1988), projections were taken using the slice phantom. However, instead of doped water, cyclohexane was used as the sample. This has a dielectric constant close to 2 in the rf range of frequencies compared with the doped water which has a dielectric constant close to 80.

## CHAPTER 5

### RESULTS

#### 5.1 Inhomogeneity of $B_1$

The inhomogeneity of  $B_1$  was checked by placing the small spherical phantom at various locations within the imaging volume in the magnet and then determining the duration of a  $\pi$ -pulse which would result in zero signal with the amplitude of the rf pulse kept constant.

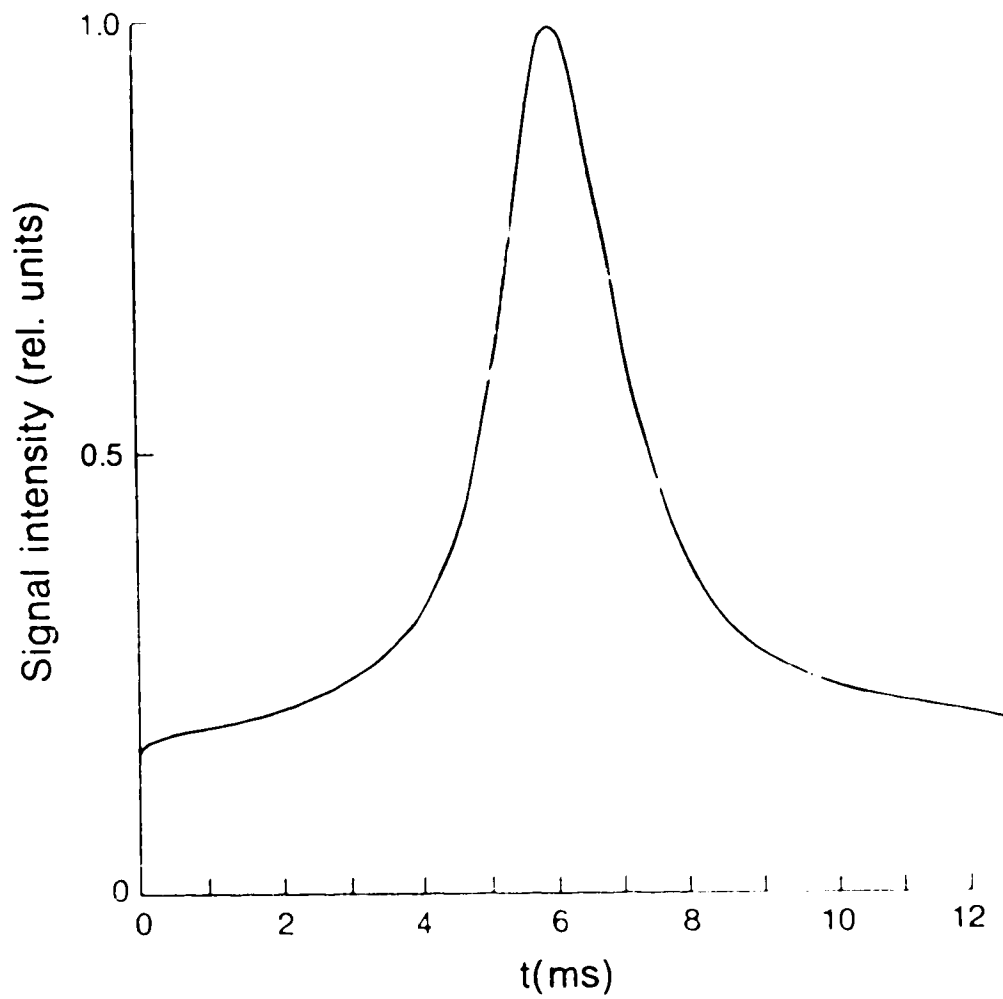
The measured durations were found to be 280  $\mu\text{s}$  at the isocentre and to vary from 260  $\mu\text{s}$  to 300  $\mu\text{s}$  at positions out to  $\pm 5$  cm in the x and y directions. At positions corresponding to 260  $\mu\text{s}$  and 300  $\mu\text{s}$ , tip angles of  $97^\circ$  and  $84^\circ$  respectively would result from a 140  $\mu\text{s}$  " $\pi/2$ -pulse". This would lead to an intensity variation of about 1%. For the  $\pi$ -pulse, a 3% intensity variation would result. Thus, at most, a 4% intensity variation can be expected due to  $B_1$  inhomogeneity.

#### 5.2 Inhomogeneity of $B_0$

Fig. 8 shows the time domain signal received in the real channel when no pulsed field gradients are applied. In other words, this is the real part of the echo envelope. The condition to be satisfied here for there to be no intensity loss due to the inhomogeneity of  $B_0$  is that  $T_2^* \gg 1 / f_1$ .  $T_2^*$  here can be seen to be about 3 ms while  $f_1$ , the maximum frequency in a typical imaging experiment, is roughly 5000 Hz giving a value of  $1 / f_1$  of 0.2 ms. Thus, the condition  $T_2^* \gg 1 / f_1$  is roughly satisfied so no serious intensity artifacts of the type mentioned in section 3.2 should arise from this mechanism, provided that the echo is properly centered.

Fig. 8

The real part of the time-domain echo-envelope acquired using the pulse program SRPP.PC with no gradient pulses.



### 5.3 Finite data acquisition period

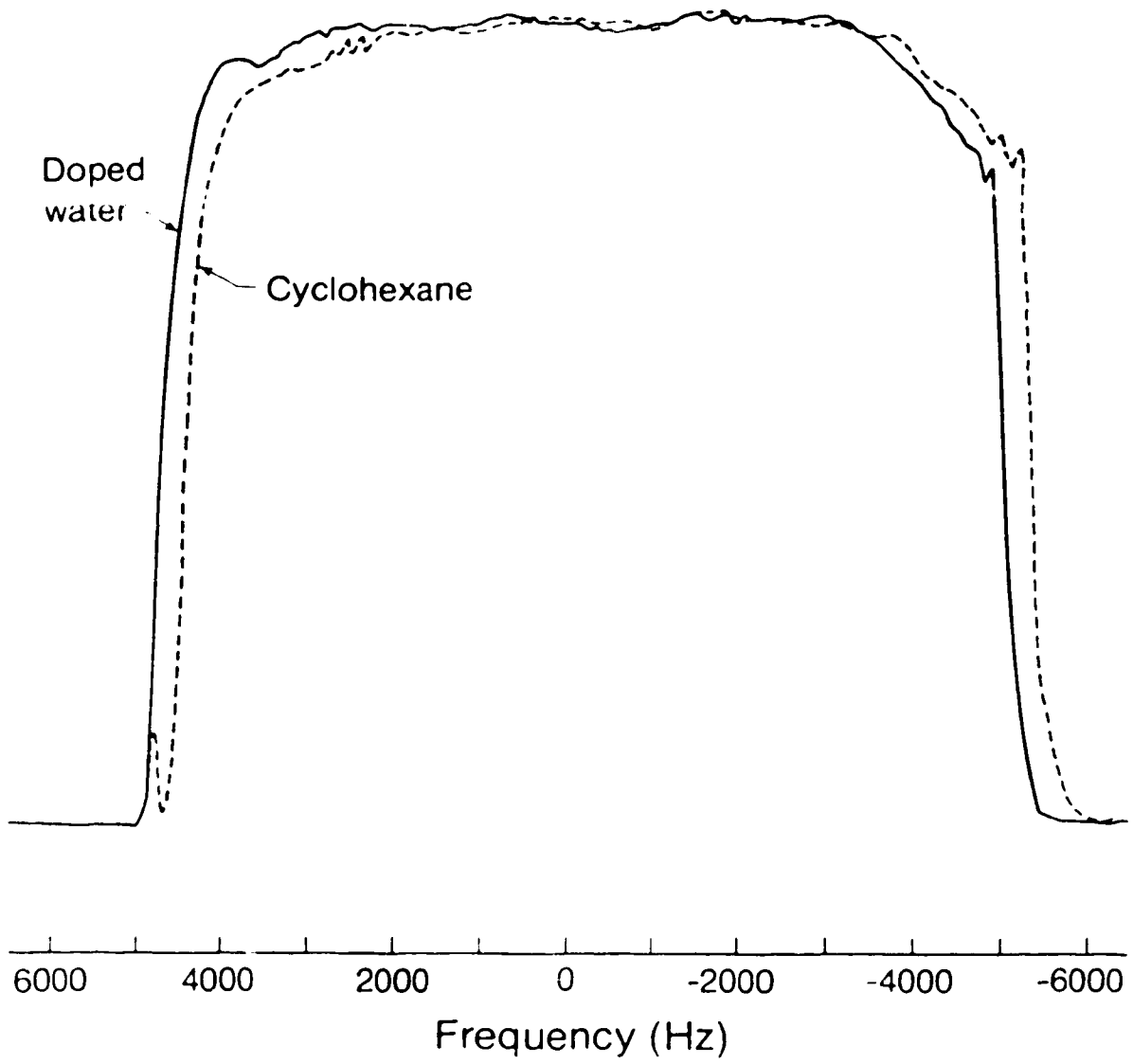
The acquisition period was set to 12.8 ms, the value used by the various imaging research groups. This satisfies the condition  $\tau_{aq} \gg 1 / f_1$  so that there should be no significant intensity artifacts of the kind discussed in section 3.3.

### 5.4 Dielectric resonances

Possible intensity artifacts arising from the dielectric resonance effect discussed in section 3.4 were investigated by comparing projections taken first with doped water and then with cyclohexane in the slice phantom. Fig. 9 shows projections obtained with the two samples under the same conditions ( i.e. all delays in SRPP.PC and shim values were identical and in particular,  $D7 = 5$  ms ). The intensities were normalized to have the same maximum value in the two cases. The positioning of the slice phantom was not exactly identical. No significant difference in intensity can be seen. The small bump in the cyclohexane projection is believed to be due to a small drop of water remaining under the cyclohexane which has a lower density than water. The projection of the cyclohexane- filled phantom is shifted about 500 Hz down frequency relative to the water image. This is presumably due to a combination of different chemical shifts ( Farrar and Becker, 1971 ) and magnetic susceptibilities in the two samples.

Fig. 9

Projections obtained with the slice phantom filled with doped (  $\text{CuSO}_4$  ) water ( dielectric constant  $\sim 80$  ) and with cyclohexane ( dielectric constant  $\sim 2$  ) obtained under the same conditions. The intensities have been normalized to be equal at 0 Hz.





## 5.5 Eddy current results

Preliminary studies showed that it was very important to position the  $\pi$ -pulse midway between the initial  $\pi/2$ -pulse and the centre of the acquisition period. For all of the following projections, great care was taken to ensure that this condition was satisfied.

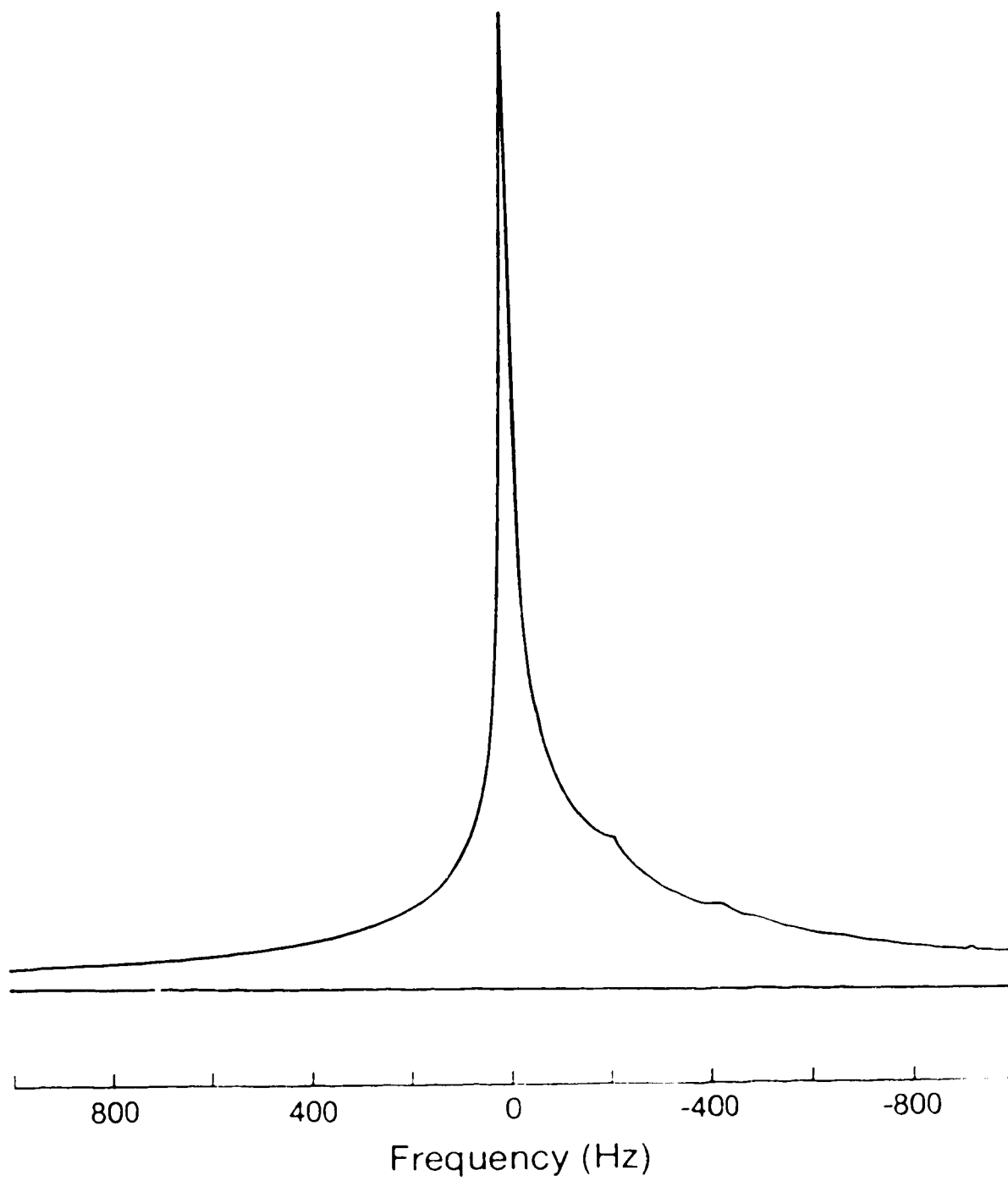
Because the various delays were not independent, it was not possible to vary one of them alone without violating the condition for the positioning of the  $\pi$ -pulse. Thus, two of the delays had to be varied together. For a particular duration of the read compensation gradient pulse, D7, the delay between the read compensation switch-off and the  $\pi$ -pulse, D6, was incremented while simultaneously incrementing the delay between the  $\pi$ -pulse and the read gradient, D4, by the same amount. This was done for values of D6 ranging from 1 ms to between 30 and 50 ms.

Experiments which showed the dependence of the positioning of the echo within the echo envelope were also performed. This was done by varying the duration of the read gradient before the acquisition period, D2, and the delay immediately before this gradient, D4, keeping  $D2 + D4$  constant. This variation caused the trimming condition (cf. sec. 2.6) to be violated, thus causing the echo to form at a time when the echo envelope was not at its maximum.

The homogeneity of the static field  $B_0$  can be inferred from the echo envelope shown in Fig. 8. It can be seen in this plot that the envelope is quite sharp but had broad wings, indicating the decay was not exponential. The magnitude of the real and imaginary parts of the Fourier transform of the initial FID corresponding to the echo of Fig. 8 is shown in Fig. 10. This shows that the peak is not symmetric and has broad wings with significant intensity past  $\pm 800$  Hz. Clearly, the homogeneity over the slice phantom was not very good.

Fig. 10

Field homogeneity plot in frequency units as given by the Fourier transform of the FID signal emanating from the slice phantom filled with doped ( $\text{CuSO}_4$ ) water in the absence of pulsed field gradients but after adjusting the linear shims



The various projections obtained with a 5 ms read compensation gradient pulse (  $D7 = 5 \text{ ms}$  ) are presented in section 5.5.1. The projections obtained with  $D7 = 25 \text{ ms}$  are then presented in section 5.5.2. Finally, in section 5.5.3, the results of the measurements of the offset frequencies due to the magnetic fields and field gradients arising from the eddy currents are presented.

### 5.5.1 Projections obtained with a read compensation gradient pulse of 5 ms duration

The first results presented in this section are those in which  $D6$  and  $D4$  were varied and  $D7$  was set to 5 ms, as was discussed above. For these projections, the other delays were chosen as follows. The duration of the  $\pi/2$ -pulse,  $D25$ , was  $150 \mu\text{s}$ ; the delay between the  $\pi/2$ -pulse and the read compensation pulse,  $D3$ , was 5 ms; the duration of the  $\pi$ -pulse,  $D1$ , was  $300 \mu\text{s}$ ; the duration of the read gradient pulse before the acquisition period,  $D2$ , was 2 ms; half of the acquisition period,  $\tau_{\text{aq}}/2$ , was 6.4ms. The values of  $D6$  chosen were 1 ms, 1.5 ms, 2 ms, 5 ms, 10 ms, 15 ms and 30 ms. For each value of  $D6$ ,  $D4$  was set to  $D6 + 1.6 \text{ ms}$  in order to keep the  $\pi$ -pulse centered. These projections are shown in Figs. 11 and 12. Note that on all projections, frequency increases to the left. Intensity values were not normalized here and in all subsequent projections. Thus, intensity values obtained under different conditions but shown on the same figure can be directly compared.

Important features to note in these projections are as follows. For the projections obtained with small values of  $D6$ , shown in Fig. 11, the higher frequencies are attenuated with the attenuation being greater when  $D6$  is small. Also, the attenuation

Fig. 11

Projections of the slice phantom acquired using the doped water sample and the pulse program SRPP.PC ( see Fig. 6 ) with  $D_{25} = 150 \mu\text{s}$ ,  $D_3 = 5 \text{ ms}$ ,  $D_7 = 5 \mu\text{s}$ ,  $D_1 = 300 \mu\text{s}$ ,  $D_2 = 2 \text{ ms}$  and  $\tau_{\text{aq}}/2 = 6.4 \text{ ms}$ . The values of  $D_6$  in ms are as indicated. The corresponding values of  $D_4$  are given by  $D_6 + 1.6 \text{ ms}$ . The read compensation gradient strength expressed in frequency units is  $-1380 \text{ Hz/cm}$  and the read gradient strength expressed in frequency unit is  $-1000 \text{ Hz/cm}$ . ( See Fig. 12 for projections taken with other values of  $D_6$ .)

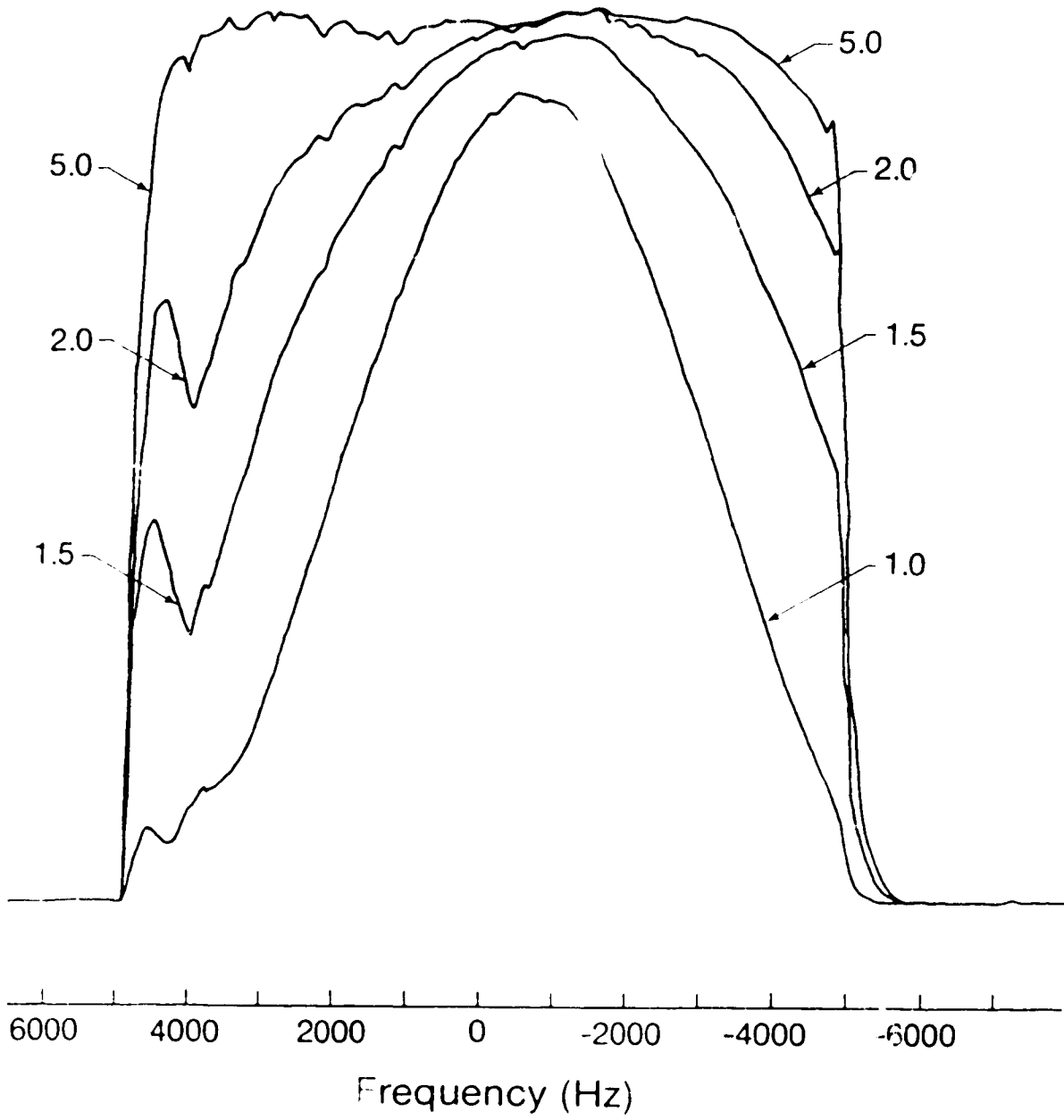
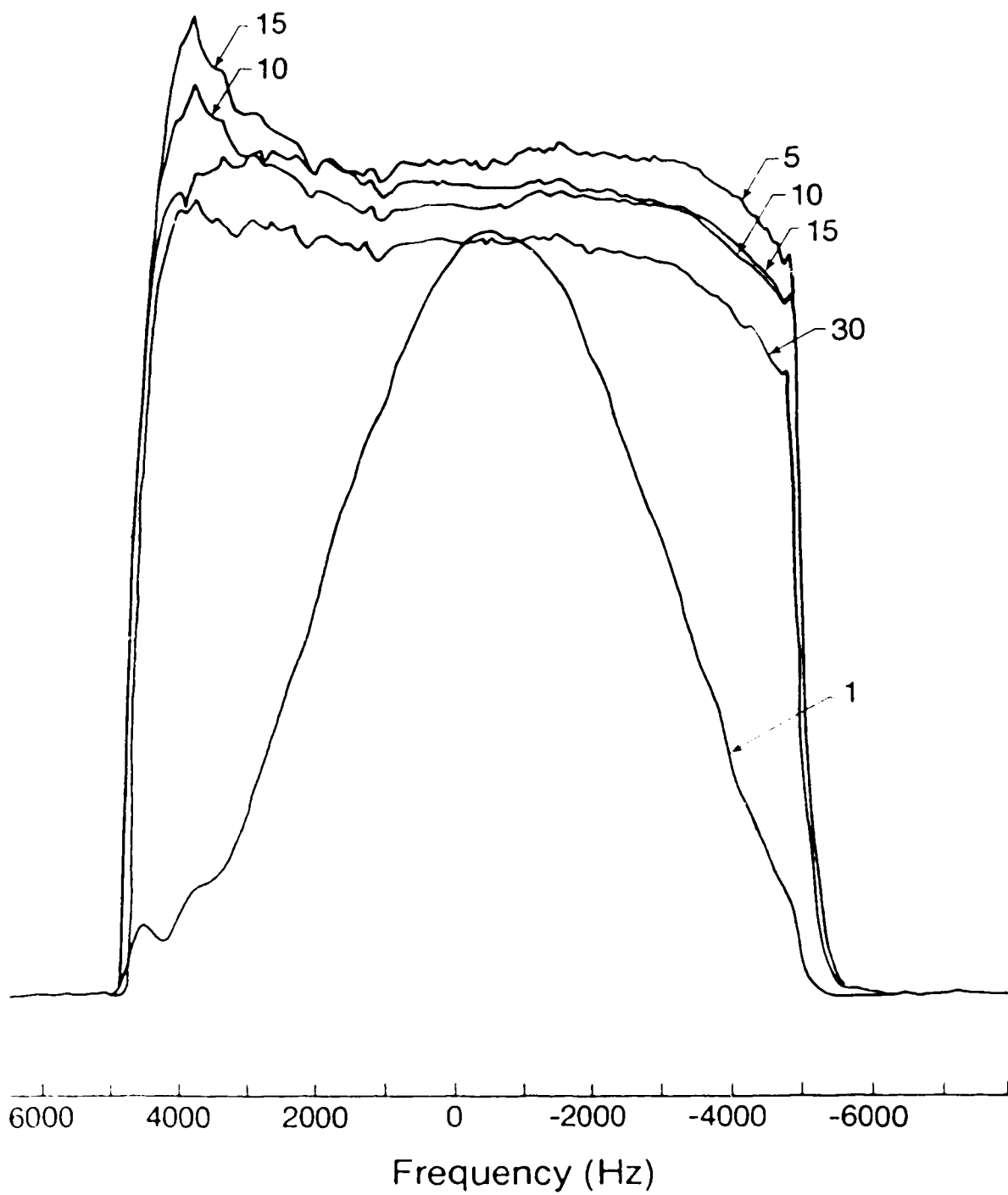


Fig. 12

Projections of the slice phantom acquired using the doped water sample and the pulse program SRPP.PC ( see Fig. 6 ) with  $D_{25} = 150 \mu\text{s}$ ,  $D_3 = 5 \text{ ms}$ ,  $D_7 = 5 \text{ ms}$ ,  $D_1 = 300 \mu\text{s}$ ,  $D_2 = 2 \text{ ms}$  and  $\tau_{\text{aq}}/2 = 6.4 \text{ ms}$ . The values of  $D_6$  in ms are as indicated. The corresponding values of  $D_4$  are given by  $D_6 + 1.6 \text{ ms}$ . The read compensation gradient strength expressed in frequency units is  $-1380 \text{ Hz/cm}$  and the read gradient strength expressed in frequency unit is  $-1000 \text{ Hz/cm}$ . ( See Fig. 11 for projections taken with other values of  $D_6$ .)



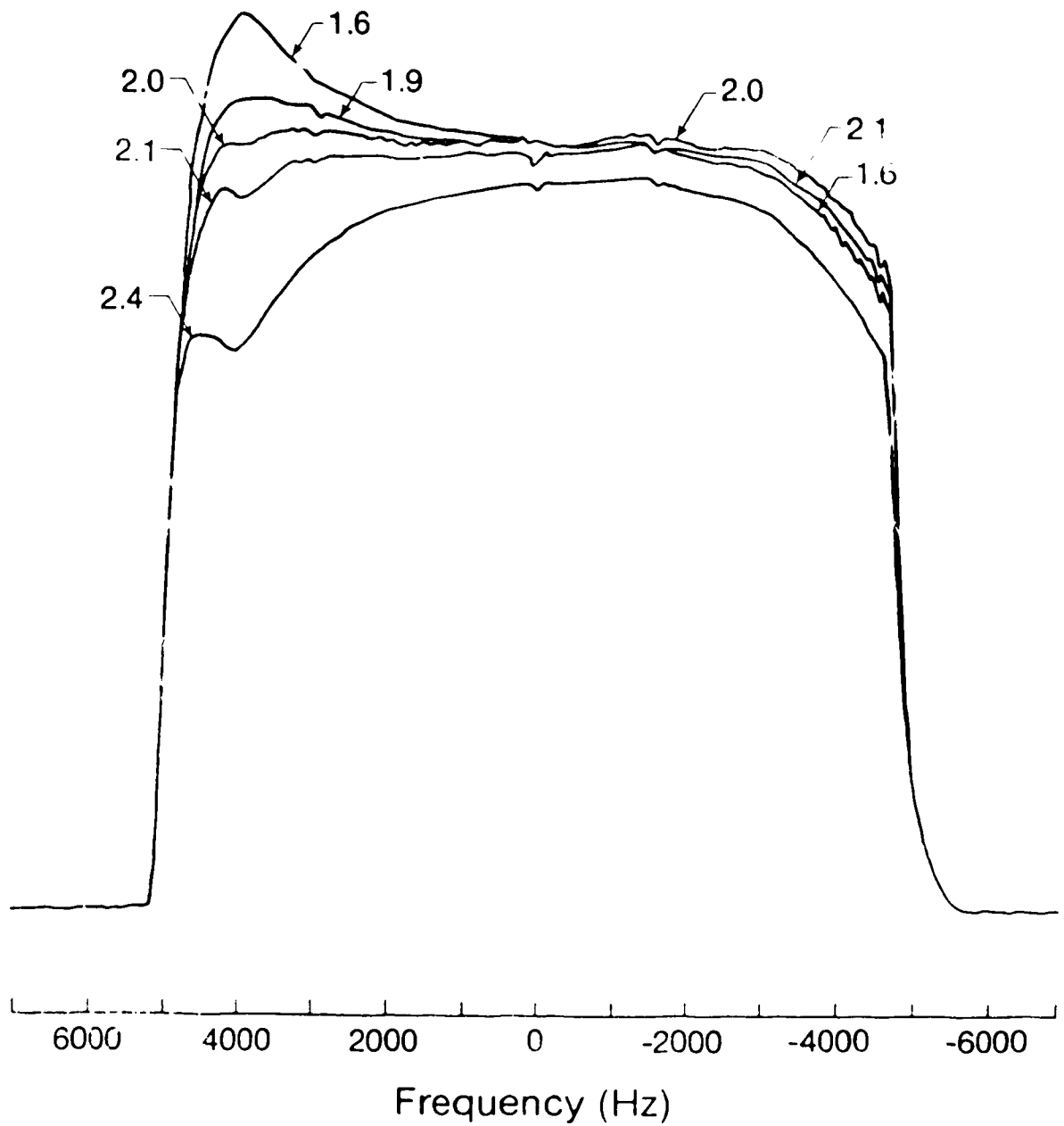


is more severe on the positive frequency side. Maximum intensity seems to occur around -700 Hz instead of at 0 Hz. As can be seen in Fig. 11, the projection corresponding to  $D_6 = 5$  ms is relatively flat, though there is some attenuation at high negative frequencies. As can be seen in Fig. 12, as  $D_6$  increases to 15 ms, the intensity on the positive frequency side increases markedly while the negative frequency side is attenuated slightly. Finally, at  $D_6 = 30$  ms, the sharp peak at the high positive frequency side is absent and the entire projection is attenuated, likely due to  $T_2$  relaxation.

The next results presented are those in which  $D_7$  was set to 5 ms,  $D_4$  and  $D_2$  were varied and all other delays were kept constant. In this case,  $D_6$  was set to 5 ms and the other delays were as above. The values used for  $D_2$  were 1.6 ms, 1.9 ms, 2.0 ms, 2.1 ms and 2.4 ms with the corresponding  $D_4$  being  $8.6$  ms -  $D_2$ . These projections are shown in Fig. 13. An important feature to note here is the strong dependence on  $D_2$  of the intensity at high positive frequencies. Also, the overall amplitude is decreased when  $D_2 = 2.4$  ms.

Fig. 13

Projections of the slice phantom acquired using the doped water sample and the pulse program SRPP.PC ( see Fig. 6 ) with  $D_{25} = 150 \mu\text{s}$ ,  $D_3 = 5 \text{ ms}$ ,  $D_7 = 5 \text{ ms}$ ,  $D_6 = 5 \text{ ms}$ ,  $D_1 = 300 \mu\text{s}$  and  $\tau_{\text{aq}}/2 = 6.4 \text{ ms}$ . The values of  $D_2$  in ms are as indicated. The corresponding values of  $D_4$  are given by  $8.6 \text{ ms} - D_2$ . The read compensation gradient strength expressed in frequency units is  $1380 \text{ Hz/cm}$  and the read gradient strength expressed in frequency unit is  $1000 \text{ Hz/cm}$ .



### 5.5.2 Projections obtained with a read compensation gradient pulse of 25 ms duration

The first results presented here are those in which D6 and D4 were varied and D7 was set to 25 ms. As before,  $D_{25} = 150 \mu\text{s}$ ,  $D_1 = 300 \mu\text{s}$  and  $\tau_{aq}/2 = 6.4 \text{ ms}$ . To accommodate the longer values for D7, D3 was set to 12 ms and D2 to 30.2ms. The values of D6 chosen were 1 ms, 2 ms, 4 ms, 8 ms, 14 ms, 20 ms, 26 ms, 32 ms, 40 ms and 50 ms. For a given value of D6, D4 was set to  $D_6 + 0.4 \text{ ms}$ .

The projections are shown in Figs. 14 and 15. They show roughly similar behavior to those observed with  $D_7 = 5 \text{ ms}$ . However, the following differences are noted. As can be seen in Fig. 14, the higher frequencies ( positive and negative ) are very severely attenuated when D6 is small. Even when D6 is as long as 20 ms, there is a substantial attenuation of the higher frequencies. When  $D_6 = 20 \text{ ms}$ , the attenuation on both sides of the central frequency appears symmetric. However, as can be seen in Fig. 15, the intensity at the high positive frequencies increases sharply with increasing D6, reaching a maximum at  $D_6 = 26 \text{ ms}$  and then falling for longer values of D6. The intensity at negative frequencies does not vary much but decreases for D6 larger than 20 ms. The projections for this case never became as flat as those obtained with  $D_7 = 5 \text{ ms}$  ( see Figs. 11 and 12 ).

The next results presented are those in which D7 was set to 25 ms, D4 and D2 were varied and all of the other delays were kept constant. In this case, D6 was chosen to be 20 ms and all of the other delays were as above. The values chosen for D2 were 29.4 ms, 29.6 ms, 29.8 ms, 30.0 ms, 30.2 ms, 30.4 ms, 30.6 ms, 30.8 ms and 31.0 ms with the corresponding values of D4 being  $50.6 \text{ ms} - D_2$ .

These projections are shown in Fig. 16. The important features to note here are as follows. As D2 increases from 29.4 ms to 31.0 ms, the intensity on the high frequency side is attenuated strongly while the intensity on the negative frequency

Fig. 14

Projections of the slice phantom acquired using the doped water sample and the pulse program SRPP.PC ( see Fig. 6 ) with  $D_{25} = 150 \mu\text{s}$ ,  $D_3 = 12 \text{ ms}$ ,  $D_7 = 25 \text{ ms}$ ,  $D_1 = 300 \mu\text{s}$ ,  $D_2 = 30.2 \text{ ms}$  and  $\tau_{\text{aq}}/2 = 6.4 \text{ ms}$ . The values of  $D_6$  in ms are as indicated. The corresponding values of  $D_4$  are given by  $D_6 + 0.4 \text{ ms}$ . The read compensation gradient strength expressed in frequency units is  $-1380 \text{ Hz/cm}$  and the read gradient strength expressed in frequency units is  $1600 \text{ Hz/cm}$ . ( See Fig. 15 for projections taken with other values of  $D_6$ .)

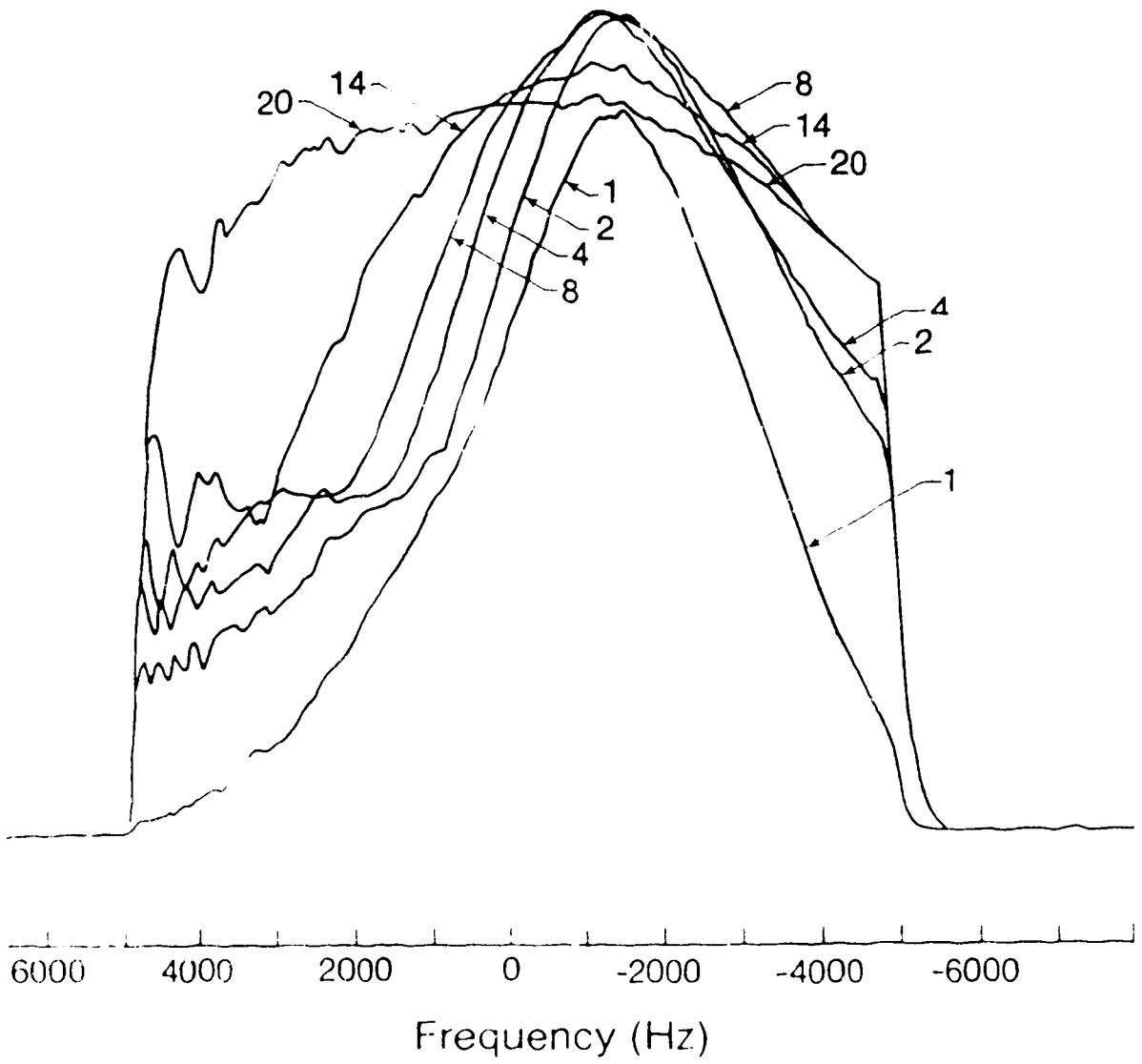


Fig. 15

Projections of the slice phantom acquired using the doped water sample and the pulse program SRPP PC ( see Fig. 6 ) with  $D_{25} = 150 \mu s$ ,  $D_3 = 12 \text{ ns}$ ,  $D_7 = 25 \text{ ms}$ ,  $D_{10} = 300 \mu s$ ,  $D_2 = 30.2 \text{ ms}$  and  $\tau_{aq}/2 = 6.4 \text{ ms}$ . The values of  $D_6$  in ms are as indicated. The corresponding values of  $D_4$  are given by  $D_6 + 0.4 \text{ ms}$ . The read compensation gradient strength expressed in frequency units is  $-1380 \text{ Hz/cm}$  and the read gradient strength expressed in frequency unit is  $-1000 \text{ Hz/cm}$ . ( See Fig. 14 for projections taken with other values of  $D_6$ .)

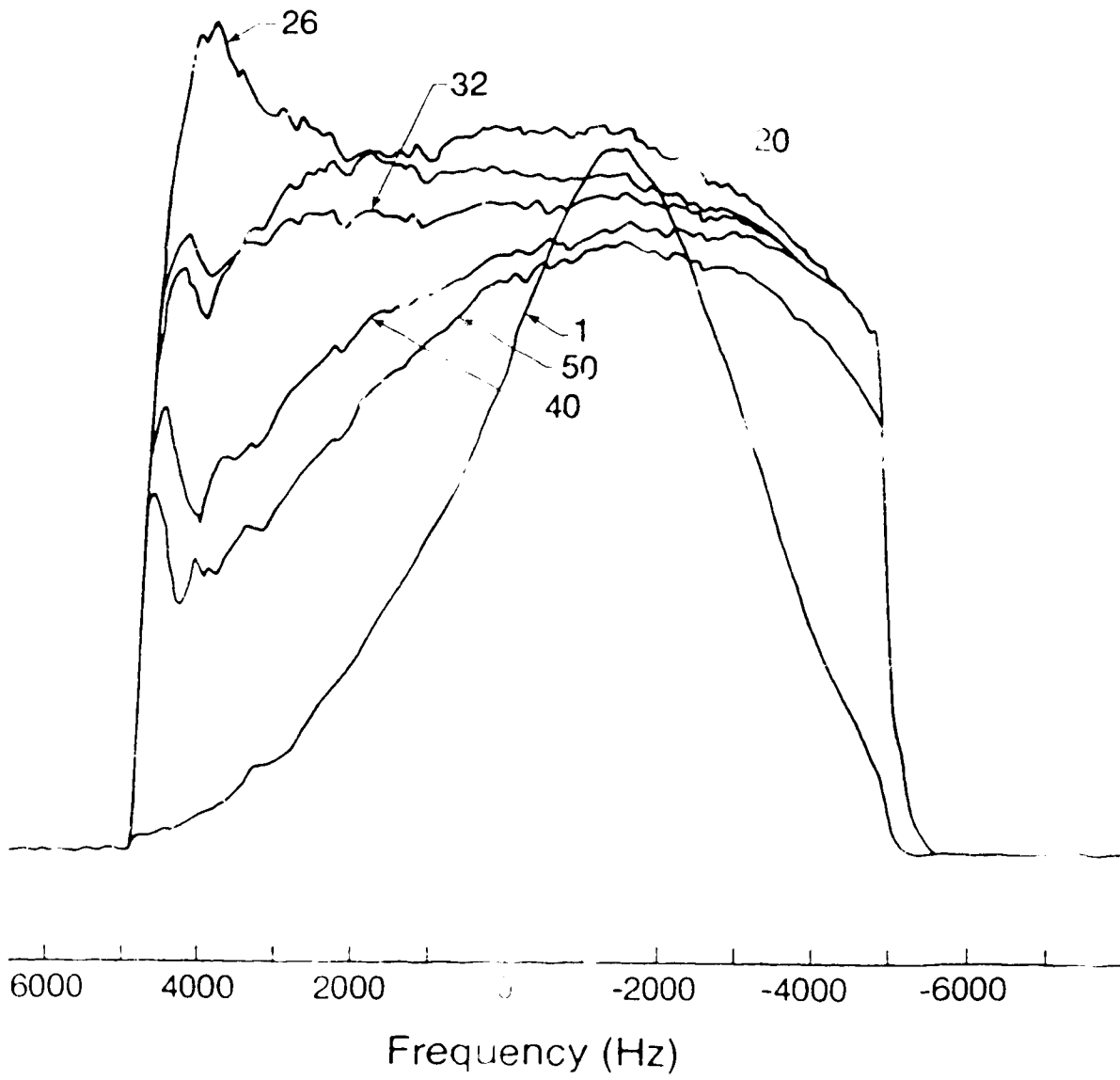
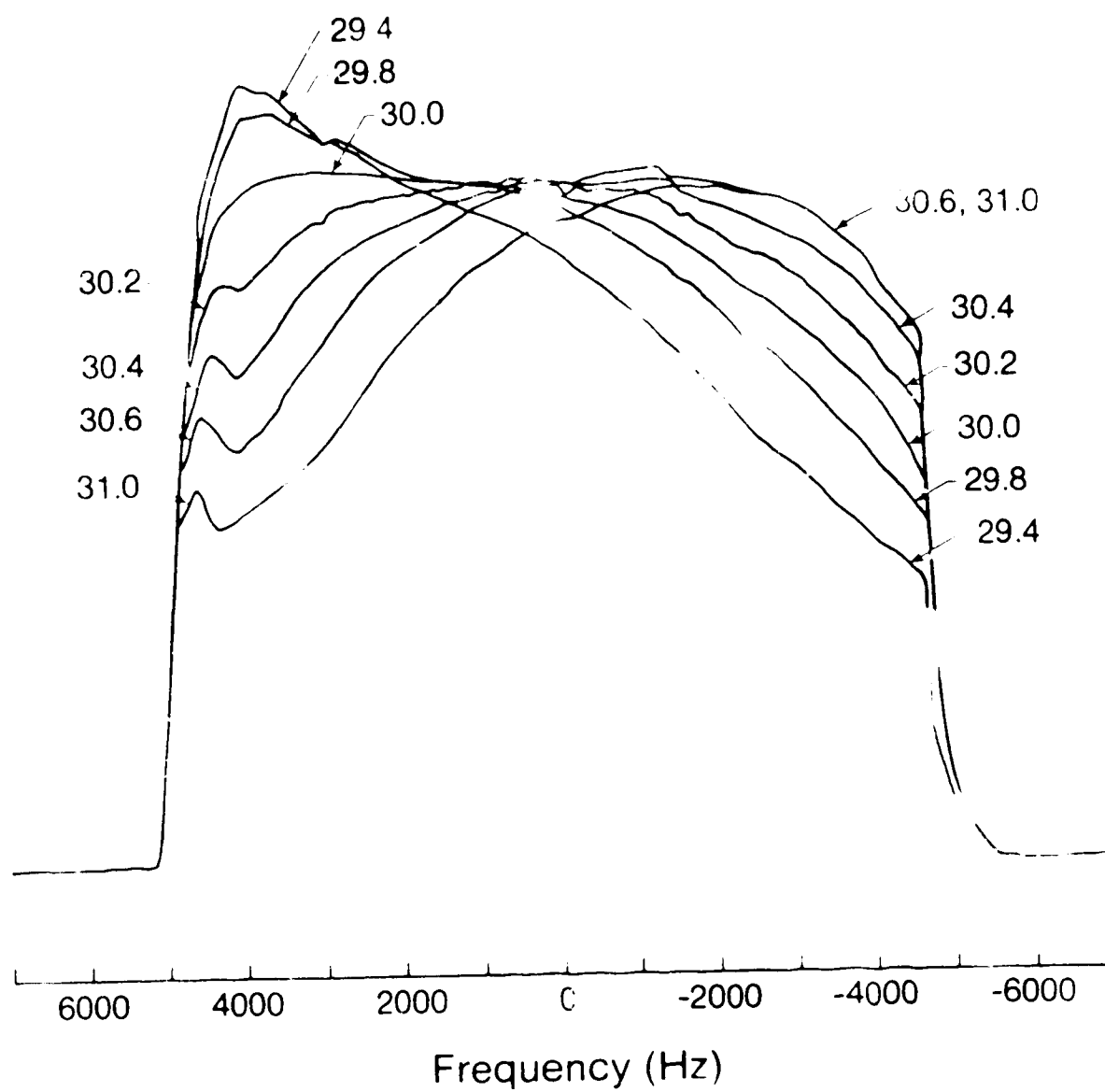




Fig. 16

Projections of the slice phantom acquired using the dopx sequence and the pulse program sRPP.PC (see Fig. 15) with  $D25 = 150 \mu\text{s}$ ,  $D3 = 12 \text{ ms}$ ,  $D7 = 25 \text{ ms}$ ,  $D6 = 20 \text{ ms}$ ,  $D1 = 10 \text{ ms}$  and  $\tau_{\text{aq}}/2 = 6.4 \text{ ms}$ . The values of  $D2$  in ms are as indicated. The corresponding values of  $D4$  are given by  $57.0 \text{ ms} - D2$ . The read compensation gradient strength expressed in frequency units is  $-1380 \text{ Hz/cm}$  and the read gradient strength expressed in frequency unit is  $1000 \text{ Hz/cm}$ .



side increases a lesser amount. The effect is much more pronounced than for the similar experiments with  $D7 = 5$  ms. It should be noted that  $D2 = 30.2$  ms is the optimum value obtained during the "trim" routine ( see sec. 4.4) for the same value of  $D6$  ( 20 ms ). It can be seen that the best ( flattest and most symmetric ) projection is obtained with  $D2 = 30.2$  ms, thereby confirming the appropriateness of the trimming procedure.

### 5.5.3 Measurements of the offset frequencies due to the magnetic field and field gradient caused by the eddy currents

The small spherical sample was placed at the following positions relative to the isocentre of the magnet:  $z = 0$  cm,  $y = 0$  cm,  $\pm 4$  cm and  $y = 0$  cm,  $\pm 5$  cm. The offset frequencies were measured using the method described in section 4.5.

The first measurements were made with a gradient pulse duration of 5 ms ( $D7 = 5$  ms) and with the same amplitude as used for the read compensation gradient pulse in the projection studies. Fig. 17 shows a plot of offset frequency in Hz as a function of time after gradient cessation for the positions corresponding to  $z = 0$  cm,  $x = 4$  cm and  $y = 0$  cm and  $\pm 5$  cm. Additional values obtained for  $x = 0$  cm,  $\pm 4$  cm and  $y = \pm 3$  cm were measured and found to lie between the central values at  $y = 0$  cm and the extreme values at  $y = \pm 5$  cm. Similarly, Fig. 18 shows the results obtained for  $x = 0$  cm and  $y = 0$  cm and  $\pm 5$  cm while Fig. 19 shows the results for  $x = -4$  cm and  $y = 0$  cm and  $\pm 5$  cm. The data are displayed in a log-log plot because of the large range of values of both the ordinate and the abscissa.

Because of the procedure used to determine offset frequencies ( see sec. 4.5 ), there is an uncertainty in the time values on the order of 2%. The errors associated with the offset frequency values are roughly 5% for  $t \leq 3$  ms and 5 Hz for  $t \geq 3$  ms. These limits were obtained by repeating measurements several times.

Frequency offset ( $f_{\text{offset}}$ ) at locations  $x = +4$  cm,  $y = 0$  cm ( crosses ),  
 $x = +5$  cm ( filled circles ) and  $y = -5$  cm ( open circles ), plotted as a  
function of time ( $t$ ) after switch-off of a 5 ms gradient pulse. The solid  
(dashed) curves correspond to positive (negative) values of the frequency  
offset. The dotted line is an extrapolation toward the value expected during  
the gradient pulse.



Fig. 18

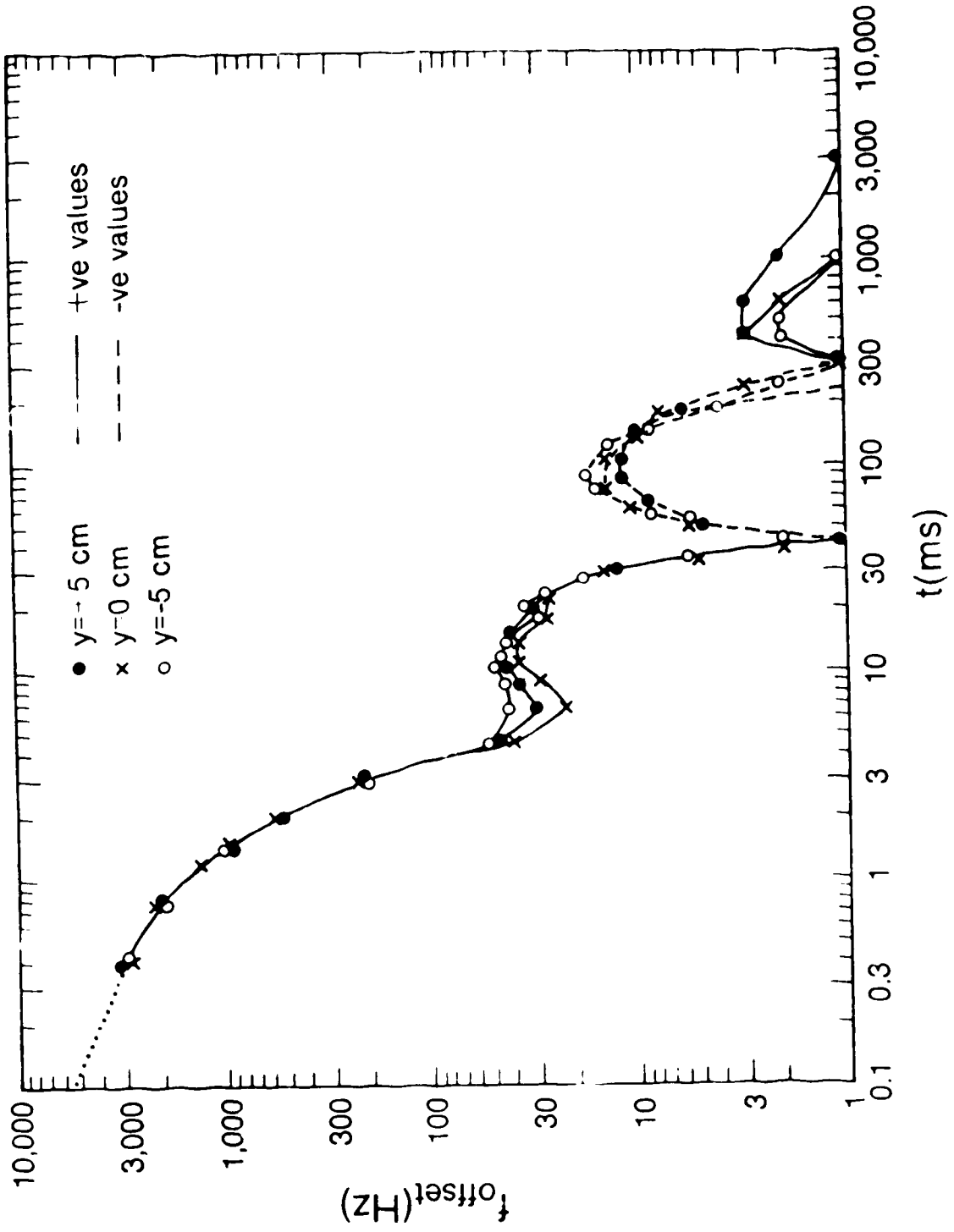
Frequency offset ( $F_{\text{offset}}$ ) at locations  $x = 0$  cm,  $y = 0$  cm ( crosses ),  $y = +5$  cm ( closed circles ) and  $y = -5$  cm ( open circles ), plotted as a function of time ( $t$ ) after switch-off of a 5 ms gradient pulse. The solid ( dashed ) curves correspond to positive ( negative ) values of frequency offset.



Fig. 19

Frequency offset ( $F_{\text{offset}}$ ) at locations  $x = -4$  cm,  $y = 0$  cm ( crosses ),  $y = +5$  cm ( closed circles ) and  $y = -5$  cm ( open circles ), plotted as a function of time ( $t$ ) after switch-off of a 5 ms gradient pulse. The solid ( dashed ) curves correspond to positive ( negative ) values of the frequency offset. The dotted line is an extrapolation toward the value expected during the gradient pulse.





Important features to note here are that the offset frequency close to the gradient switch-off is much higher for  $x = \pm 4$  cm than for  $x = 0$  cm, as expected. Also, the offset frequency for a given value of  $x$  varies with  $y$ , as can clearly be seen in Fig. 19 from 4 ms to 10 ms. This indicates that the magnetic field along an isochromat ( fixed value of  $x$  ) is not homogeneous after ( and presumably during ) a gradient pulse.

Similar measurements were also made with a 25 ms gradient pulse. Fig. 20 shows a plot of the offset frequency as a function of time for  $x = 4$  cm and  $y = 0$  cm and  $\pm 5$  cm. Similarly, Fig. 21 shows the results obtained for  $x = 0$  cm and  $y = 0$  cm and  $\pm 5$  cm while Fig. 22 shows the results for  $x = -4$  cm and  $y = 0$  cm and  $\pm 5$  cm.

Important features to note here are that the offset frequency close to the gradient switch-off is much higher for  $x = \pm 4$  cm than for  $x = 0$  cm, as was the case for a 5 ms gradient pulse. Also, the differences in the offset frequencies for different values of  $y$  for given value of  $x$  are larger than was the case for a 5 ms gradient pulse. The offset frequency also takes longer to approach zero than with a 5 ms gradient pulse.

To better understand the behavior of the magnetic field after the gradient pulse, the same data are shown plotted in different formats. For instance, in Fig. 23, offset frequencies as a function of time after the switch-off of a 5 ms gradient pulse are shown for  $x = 0$  cm and  $\pm 4$  cm and with  $y$  kept constant at 0 cm. Fig. 24 shows the corresponding behavior for a 25 ms gradient pulse. It is obvious from these plots that, since the offset frequencies are not symmetric about 0 Hz at  $x = \pm 4$  cm, eddy currents contribute a time dependent magnetic field as well as a gradient field. Moreover, this contribution is greater for the longer gradient pulse since the observed asymmetry is worse.

Fig. 20

Frequency offset (  $F_{\text{offset}}$  ) at locations  $x = +4$  cm,  $y = 0$  cm ( crosses ),  $y = +5$  cm ( closed circles ) and  $y = -5$  cm ( open circles ), plotted as a function of time (  $t$  ) after switch-off of a 25 ms gradient pulse. The solid ( dashed ) curves correspond to positive ( negative ) values of the frequency offset. The dotted line is an extrapolation toward the expected value during the gradient pulse.

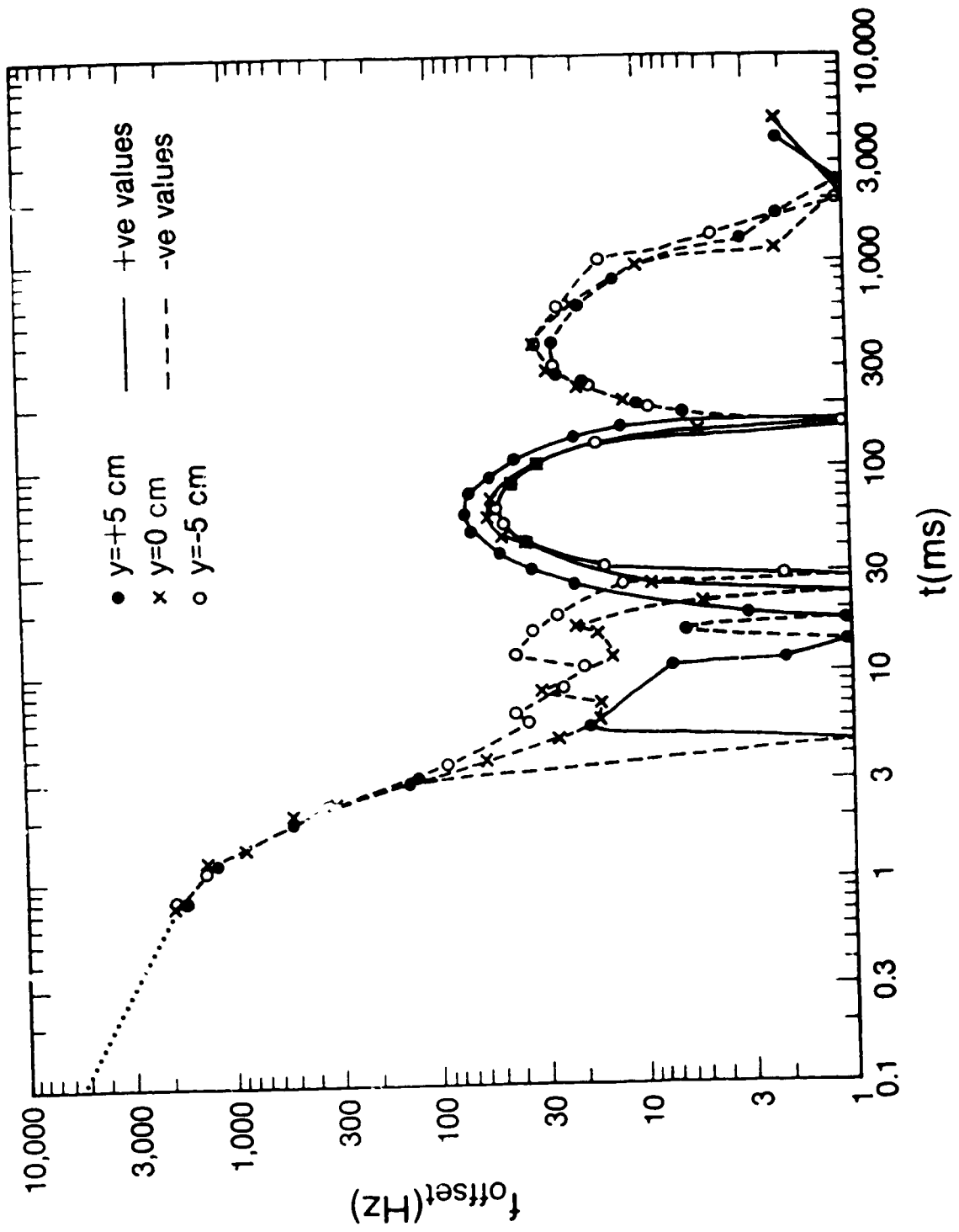


Fig. 2i

Frequency offset (  $F_{\text{offset}}$  ) at locations  $x = 0$  cm,  $y = 0$  cm ( crosses ),  $y = +5$  cm ( closed circles ) and  $y = -5$  cm ( open circles ), plotted as a function of time (  $t$  ) after switch-off of a 25 ms gradient pulse. The solid ( dashed ) curves correspond to positive ( negative ) values of the frequency offset.

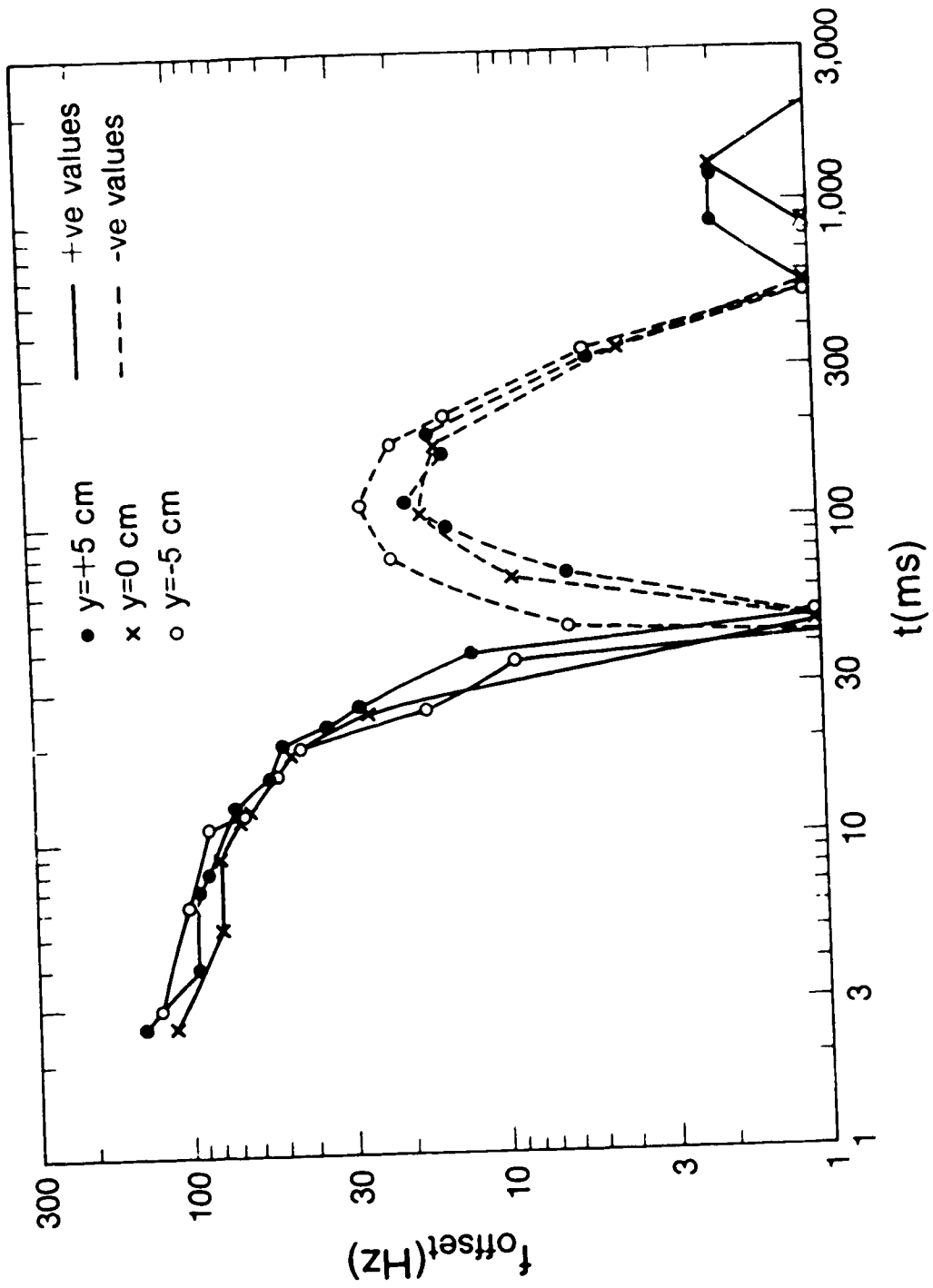


Fig. 22

Frequency offset ( $F_{\text{offset}}$ ) at locations  $x = -4$  cm,  $y = 0$  cm ( crosses ),  $y = +5$  cm ( closed circles ) and  $y = -5$  cm ( open circles ), plotted as a function of time ( $t$ ) after switch-off of a 25 ms gradient pulse. The solid ( dashed ) curves correspond to positive ( negative ) values of the frequency offset. The dotted line is an extrapolation toward the value expected during the gradient pulse.

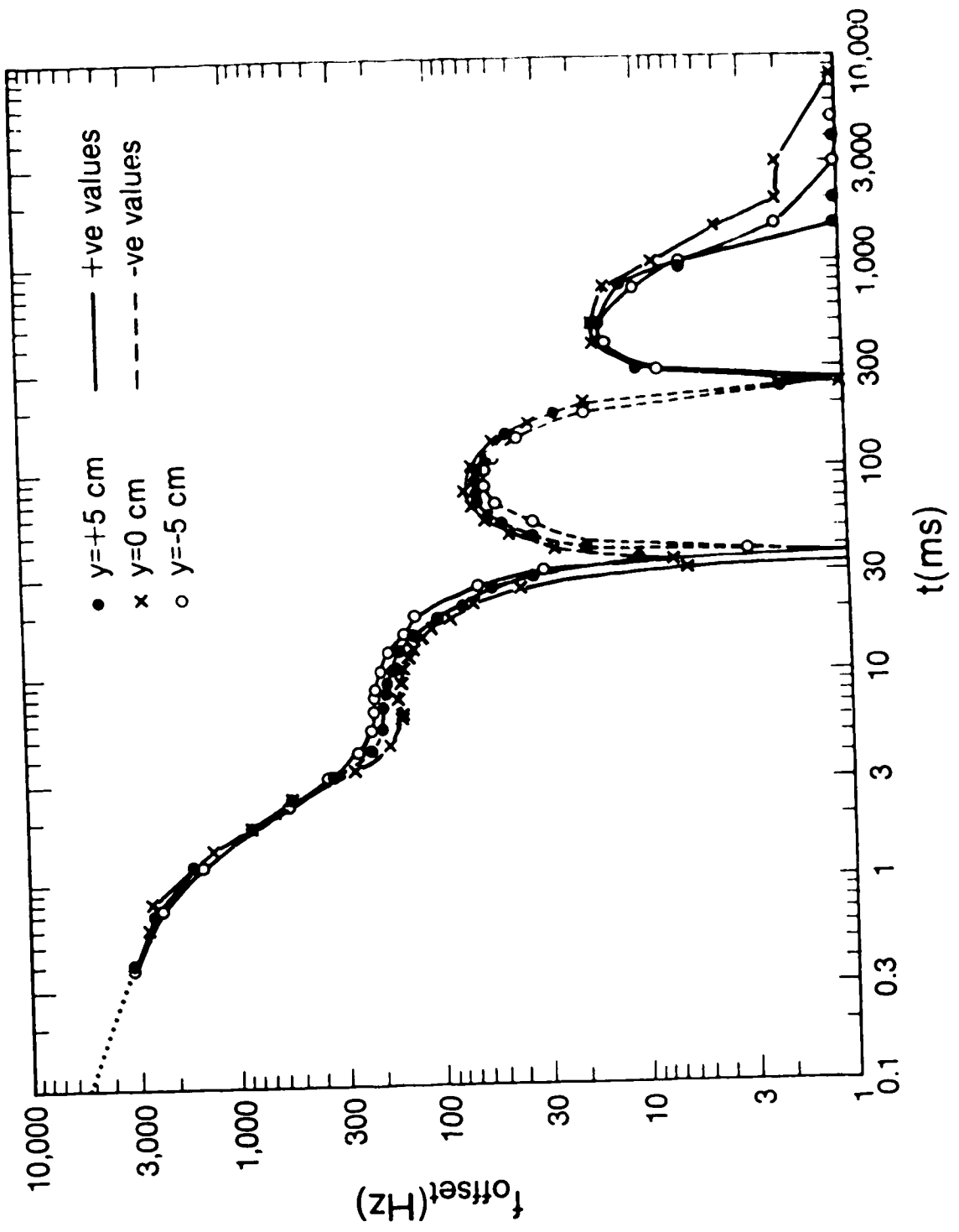




Fig. 23

Frequency offset ( $F_{\text{offset}}$ ) at locations  $y = 0$  cm,  $x = 0$  cm ( crosses ),  $x = +4$  cm ( closed circles ) and  $x = -4$  cm ( open circles ), plotted as a function of time ( $t$ ) after switch-off of a 5 ms gradient pulse. The solid ( dashed ) curves correspond to positive ( negative ) values of the frequency offset. The dotted line is an extrapolation toward the value expected during the gradient pulse.

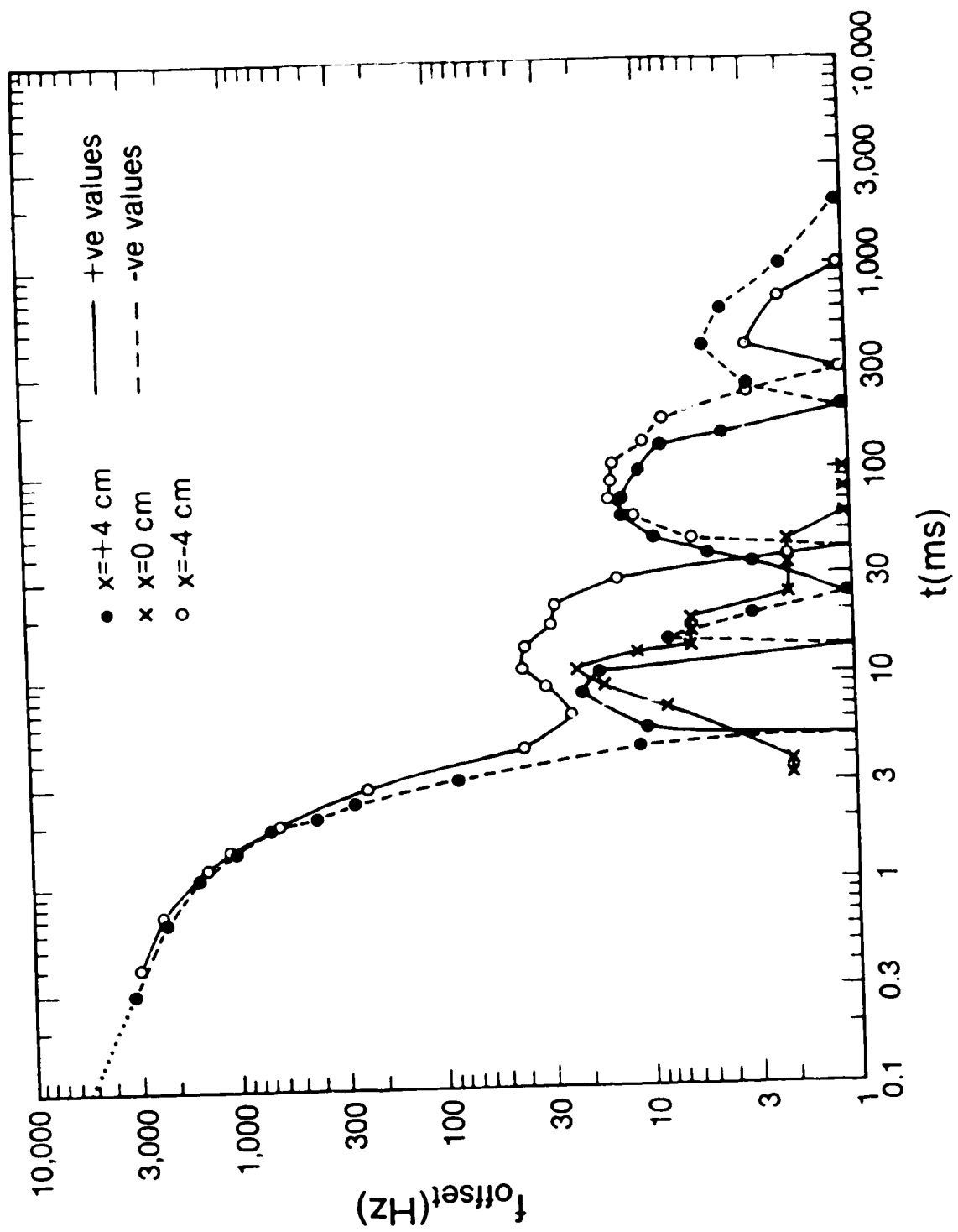
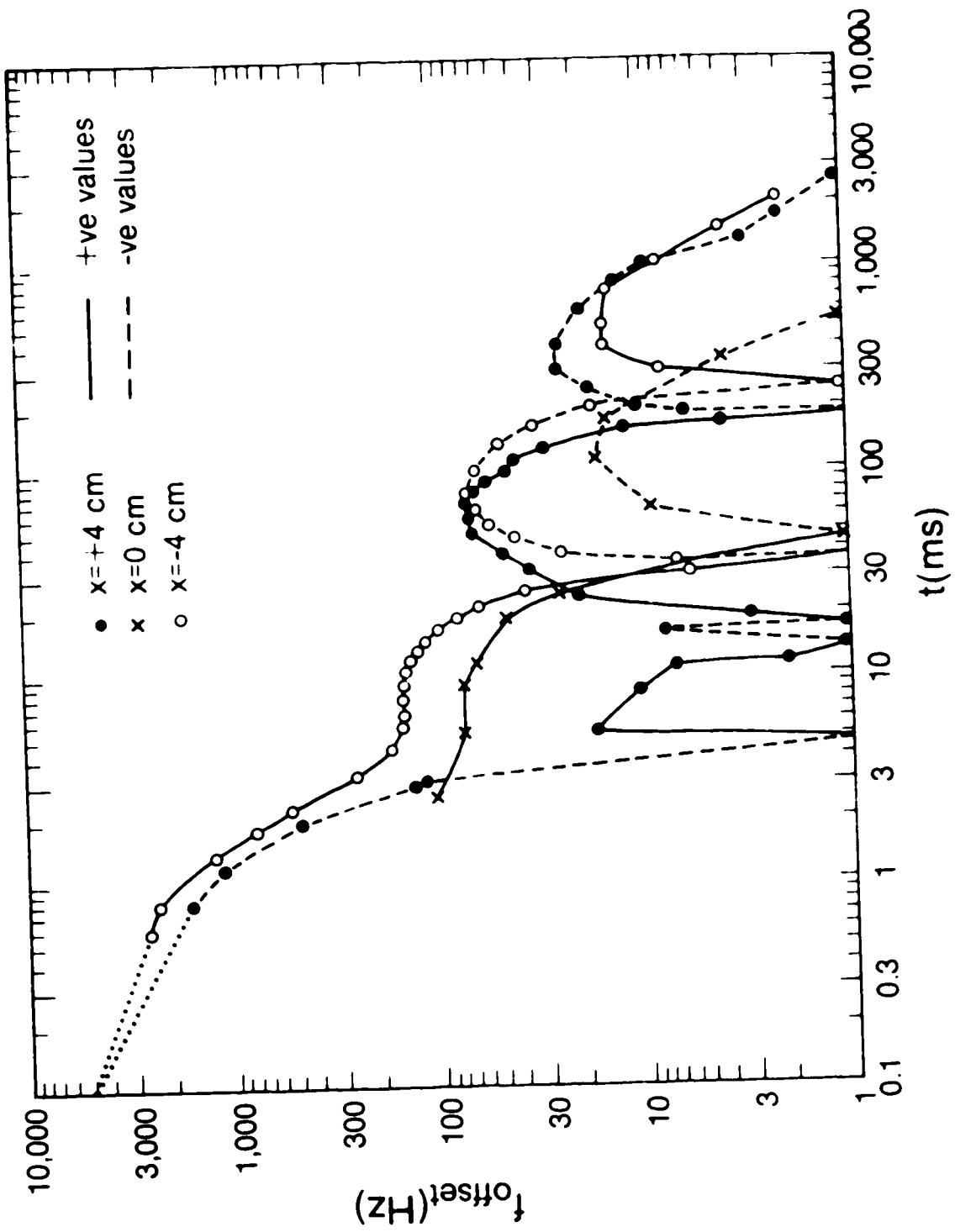


Fig. 24

Frequency offset ( $F_{\text{offset}}$ ) at locations  $y = 0$  cm,  $x = 0$  cm ( crosses ),  $x = +4$  cm ( closed circles ) and  $x = -4$  cm ( open circles ), plotted as a function of time ( $t$ ) after switch-off of a 25 ms gradient pulse. The solid ( dashed ) curves correspond to positive ( negative ) values of the frequency offset. The dotted lines are an extrapolation towards the value expected during the gradient pulse.



Another useful format is to plot the difference between the average frequency at  $y = \pm 5$  cm and the frequency at  $y = 0$  cm for a given value of  $x$  and gradient pulse duration. For a 5 ms gradient pulse, these are plotted in Figs. 25, 26 and 27 for  $x = 4$  cm, 0 cm and  $-4$  cm respectively. For a 25 ms gradient pulse, this is plotted in Figs. 28, 29 and 30 for  $x = 4$  cm, 0 cm and  $-4$  cm respectively.

The error in the difference frequency is roughly  $\pm 10$  Hz. For a 5 ms gradient pulse, no significant difference can be observed for  $t \geq 10$  ms. For  $t \leq 10$  ms, there is some indication of a slight rise as  $t \rightarrow 0$  as indicated by the smooth curves drawn through the data in Figs. 25, 26 and 27. Similar but larger effects can be seen when  $D7 = 25$  ms, as shown in Figs. 28, 29 and 30.

**Fig. 25**

**Difference between the offset frequencies at  $y = \pm 5$  cm and  $y = 0$  cm for  $x = +4$  cm plotted as a function of time after switch-off of a 5 ms gradient pulse. The solid curve is a smooth curve drawn through the data.**

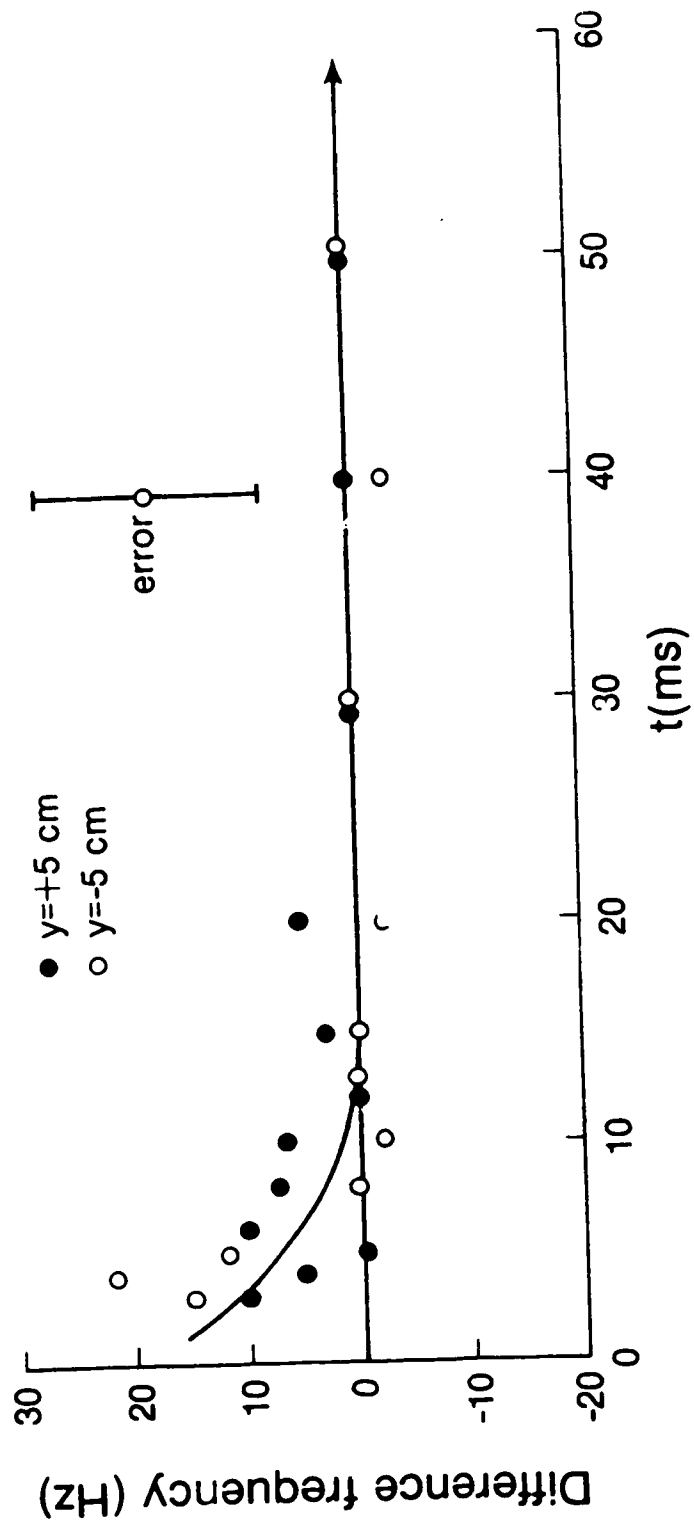


**Fig. 26**

**Difference between the offset frequencies at  $y = \pm 5$  cm and  $y = 0$  cm for  $x = 0$  cm plotted as a function of time after switch-off of a 5 ms gradient pulse. The solid curve is a smooth curve drawn through the data.**



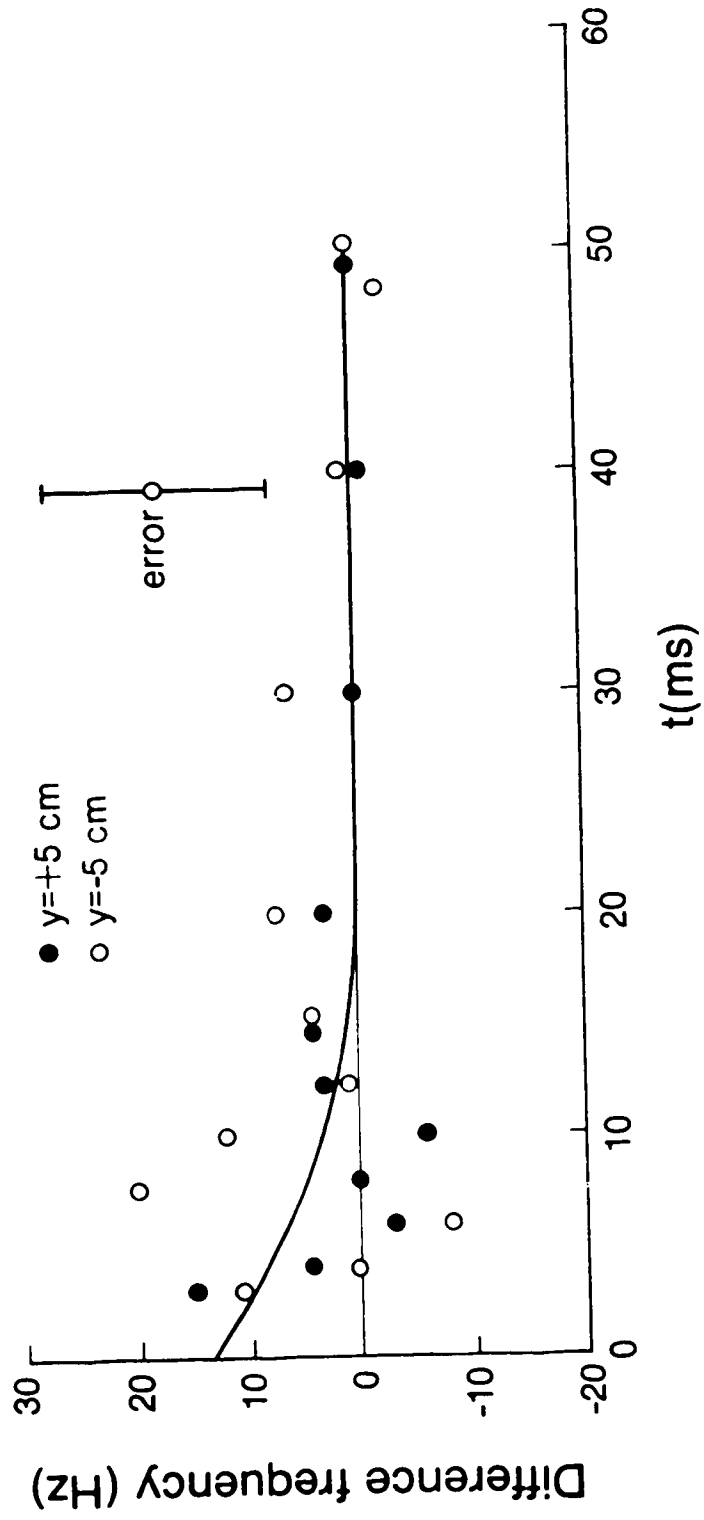


Fig. 27

Difference between the offset frequencies at  $y = \pm 5$  cm and  $y = 0$  cm for  $x = -4$  cm plotted as a function of time after switch-off of a 5 ms gradient pulse. The solid curve is a smooth curve drawn through the data.

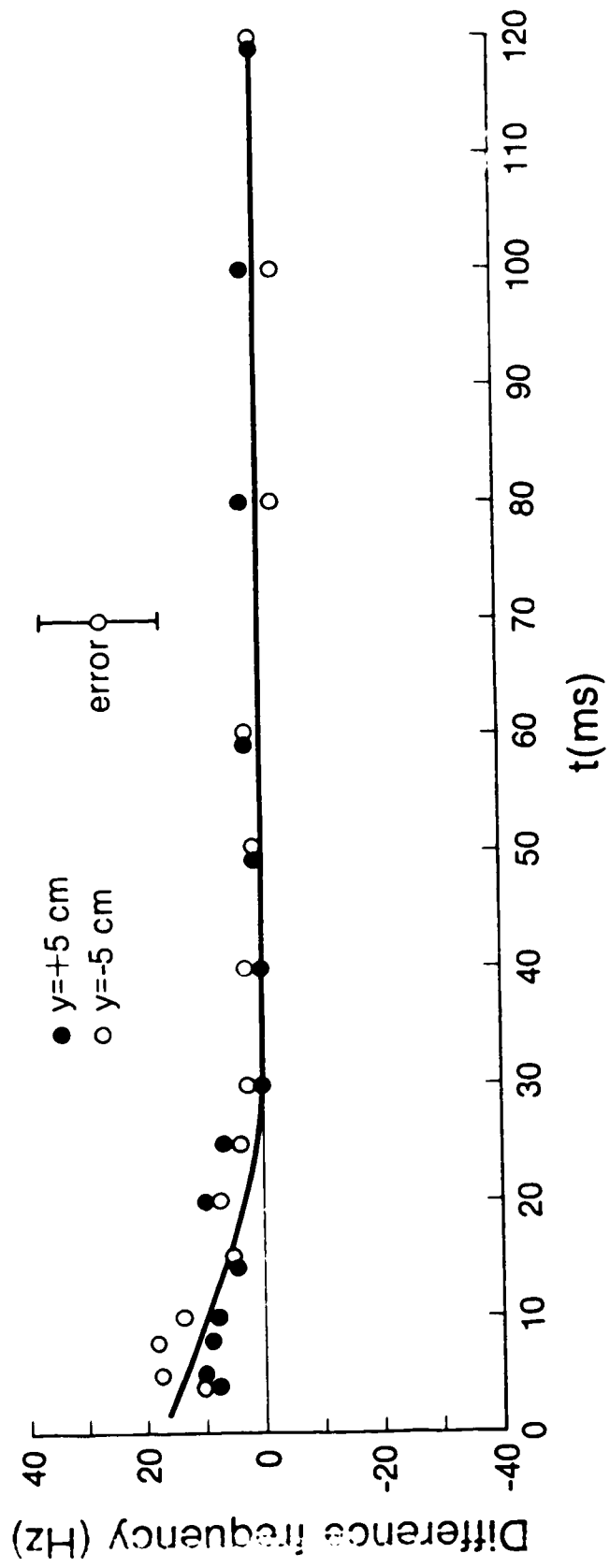


Fig. 28

Difference between the offset frequencies at  $y = \pm 5$  cm and  $y = 0$  cm for  $x = +4$  cm plotted as a function of time after switch-off of a 25 ms gradient pulse. The solid curve is a smooth curve drawn through the data.

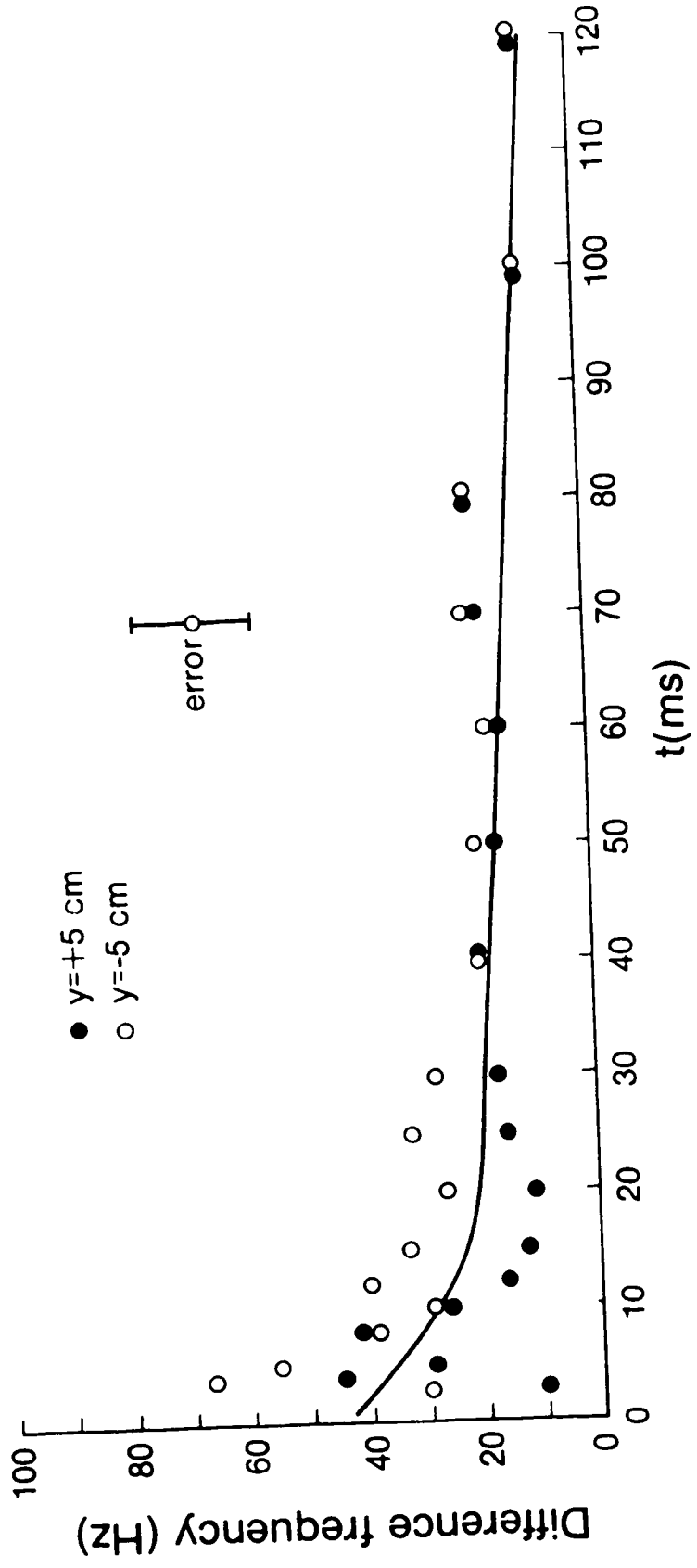
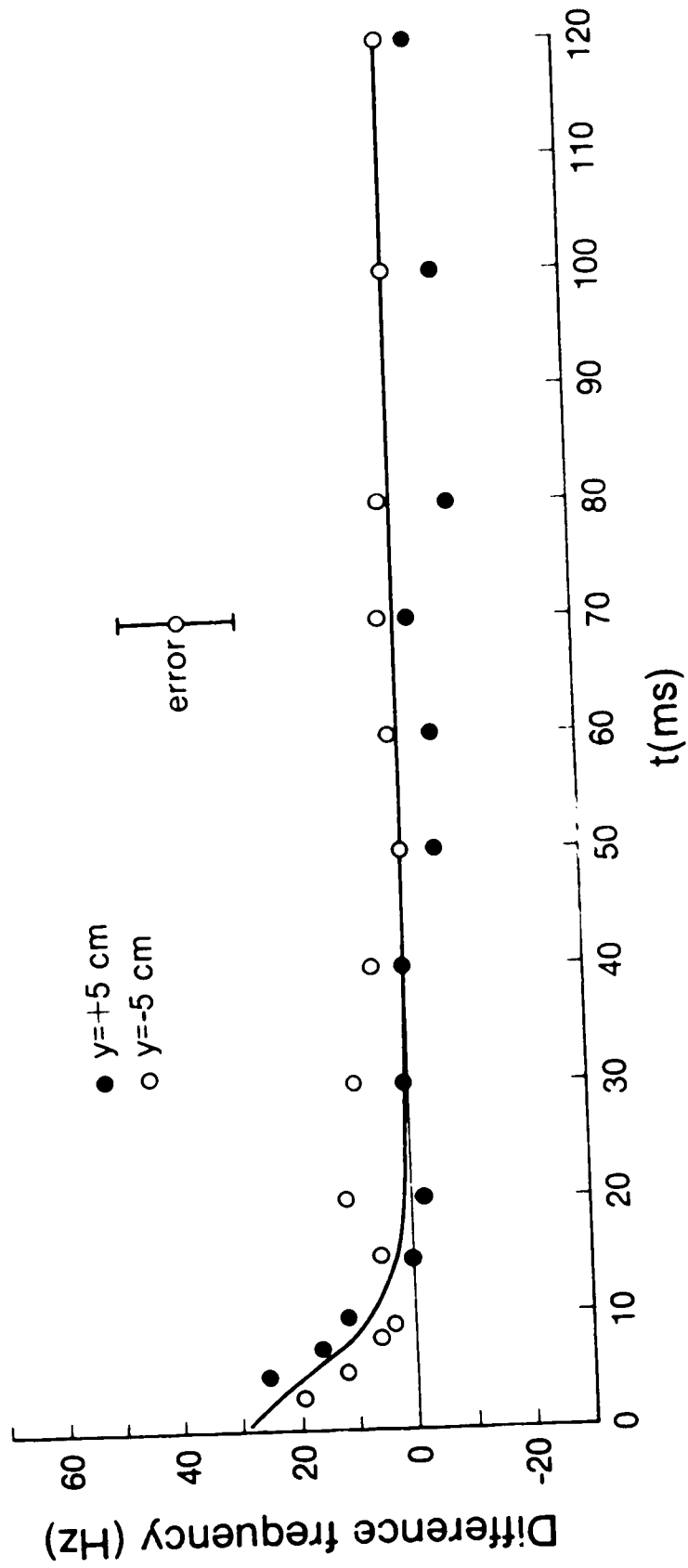


Fig. 29

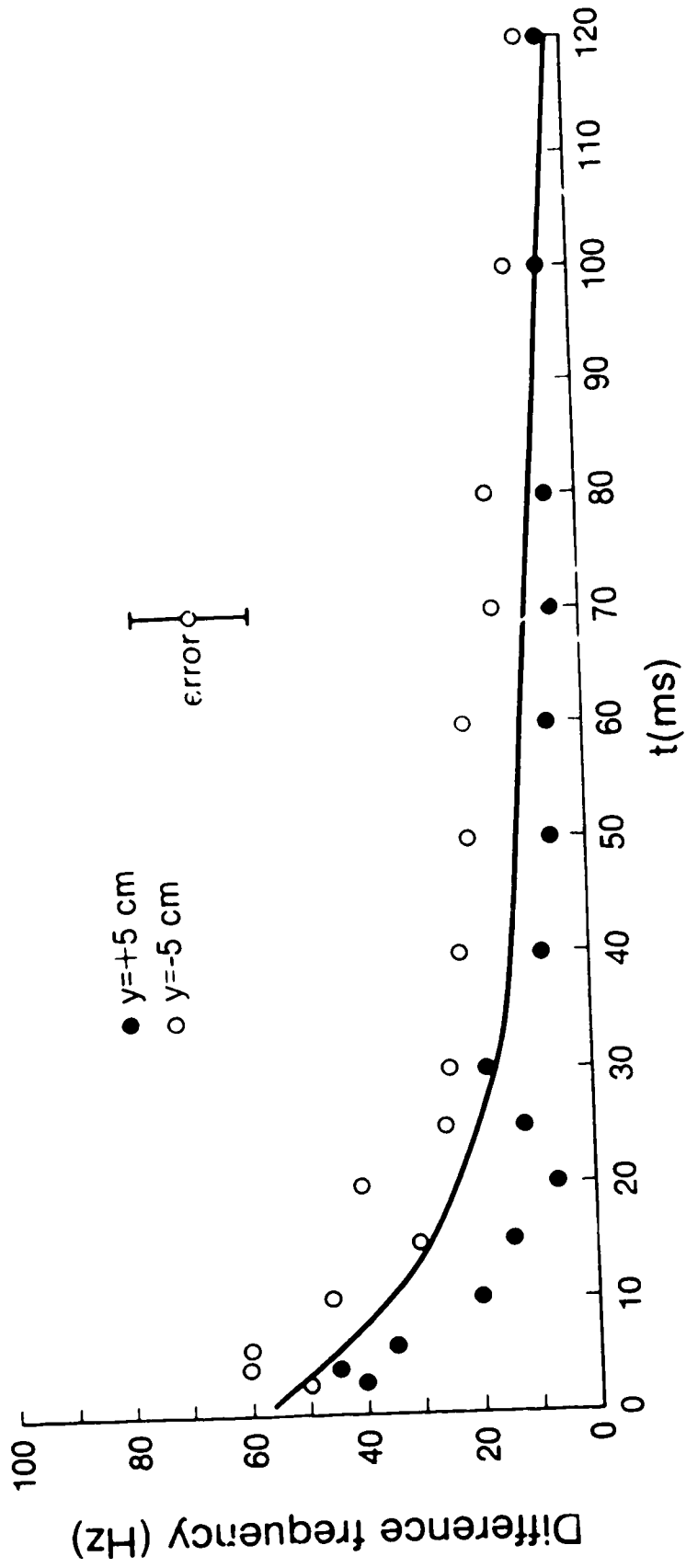
Difference between the offset frequencies at  $y = \pm 5$  cm and  $y = 0$  cm for  $x = 0$  cm plotted as a function of time after switch-off of a 25 ms gradient pulse. The solid curve is a smooth curve drawn through the data.



**Fig. 30**

Difference between the offset frequencies at  $y = \pm 5$  cm and  $y = 0$  cm for  $x = -4$  cm plotted as a function of time after switch-off of a 25 ms gradient pulse. The solid curve is a smooth curve drawn through the data.





## CHAPTER 6

### ANALYSIS AND DISCUSSION OF RESULTS

#### 6.1 Off-resonance effects

As can be seen in Figs. 23 and 24, the offset frequencies measured at  $x = \pm 4$  cm are very large for  $t \leq 1$  ms and take a long time to decay to zero. There will therefore be substantial off-resonance effects if the " $\pi$  pulse" is applied too soon after the gradient pulse is switched off. We derived an approximate expression in section 3.5.2 for the amplitude of the transverse magnetization measured at time  $t = T_E$  as a function of the ratio of  $\Delta B$ , the off-resonance field experienced by a group of nuclei during the " $\pi$ -pulse", to  $B_1$ , the amplitude of the rotating component of the rf field. The expected behavior is shown in Fig. 5.

The value of  $B_1$  can be found from the 300  $\mu$ s duration of the  $\pi$ -pulse and the known value,  $2.67 \times 10^4 \text{ G}^{-1}\text{s}^{-1}$ , of the magnetogyric ratio of protons. Thus, since  $\gamma B_1 \tau = \pi$  for a  $\pi$ -pulse of duration  $\tau$ , we find  $B_1$  to be 0.392 G. Expressed in frequency units, i.e.  $\gamma B_1 / 2\pi$ ,  $B_1$  is 1670 Hz.

Values of  $\Delta B$ , expressed in frequency units, will be the offset frequencies shown in Figs. 23 and 24, at the time of the " $\pi$ -pulse". We take this time to be the time at its centre, i.e. 150  $\mu$ s after the switch-on of the " $\pi$ -pulse".

We can now compare the projections in Figs. 11, 12, 13 and 14 with the prediction of our simple theory. In particular, we consider the projections obtained with  $D_6 = 1$  ms and 2 ms, for gradient pulse durations ( $D_7$ ) of 5 ms and 25 ms. These projections are shown again in Figs. 31, to 34. Also shown in these figures are calculated projections obtained in the following way. Knowing the values of  $D_6$  and  $D_7$  for the particular projection, the offset frequencies at positions  $x = \pm 4$  cm can be

Fig. 31

Projection obtained using the slice phantom filled with doped water and the pulse program SRPP.PC with  $D7 = 5 \text{ ms}$ ,  $D6 = 1 \text{ ms}$ ,  $D25 = 150 \text{ }\mu\text{s}$ ,  $D3 = 5 \text{ ms}$ ,  $D1 = 300 \text{ }\mu\text{s}$ ,  $D4 = 2.6 \text{ ms}$  and  $\tau_{3q}/2 = 6.4 \text{ ms}$  ( solid curve ). A calculated projection ( dashed curve ) based on the off-resonance effect is also shown.

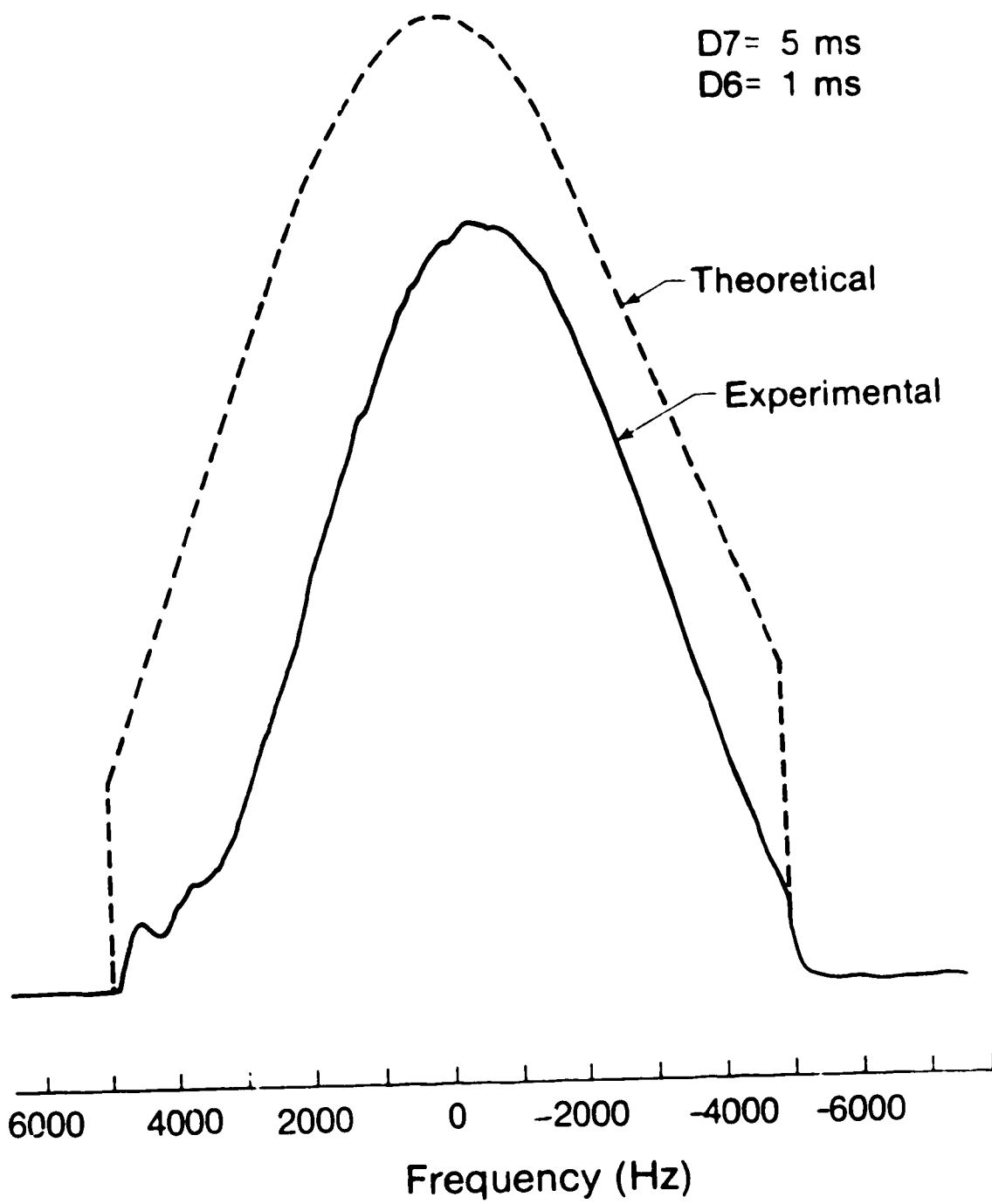


Fig. 32

Projection obtained using the slice phantom filled with doped water and the pulse program SRPP.PC with  $D7 = 5 \text{ ms}$ ,  $D6 = 2 \text{ ms}$ ,  $D25 = 150 \mu\text{s}$ ,  $D3 = 5 \text{ ms}$ ,  $D1 = 300 \mu\text{s}$ ,  $D4 = 2.6 \text{ ms}$  and  $\tau_{aq}/2 = 6.4 \text{ ms}$  ( solid curve ). A calculated projection ( dashed curve ) based on the off-resonance effect is also shown.

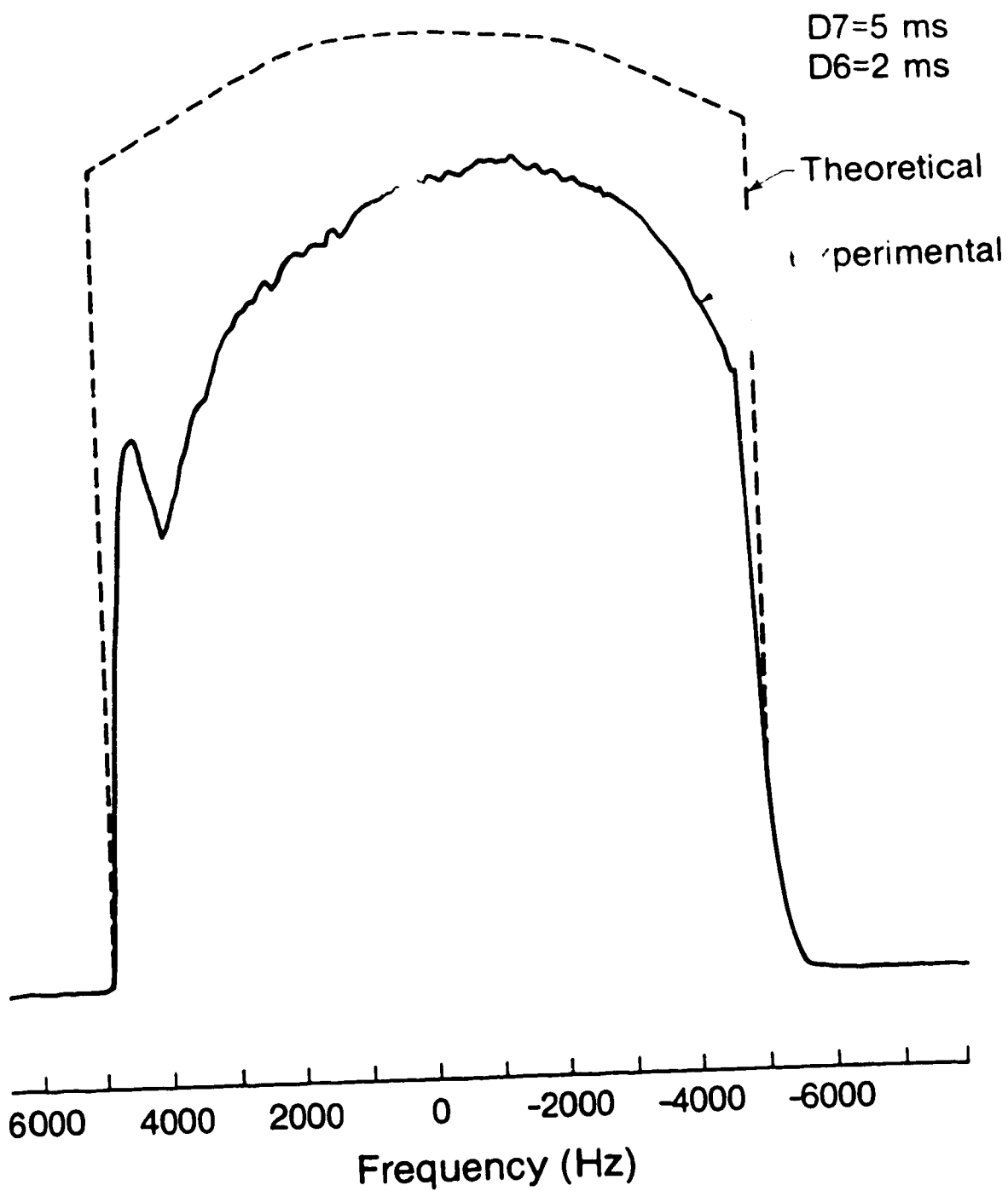


Fig. 33

Projection obtained using the slice phantom filled with doped water and the pulse program SRPP.PC with  $D7 = 25$  ms ,  $D6 = 1$  ms,  $D25 = 150$   $\mu$ s,  $D3 = 5$  ms,  $D1 = 300$   $\mu$ s,  $D4 = 2.6$  ms and  $\tau_{2q}/2 = 6.4$  ms ( solid curve ). A calculated projection ( dashed curve ) based on the off-resonance effect is also shown.

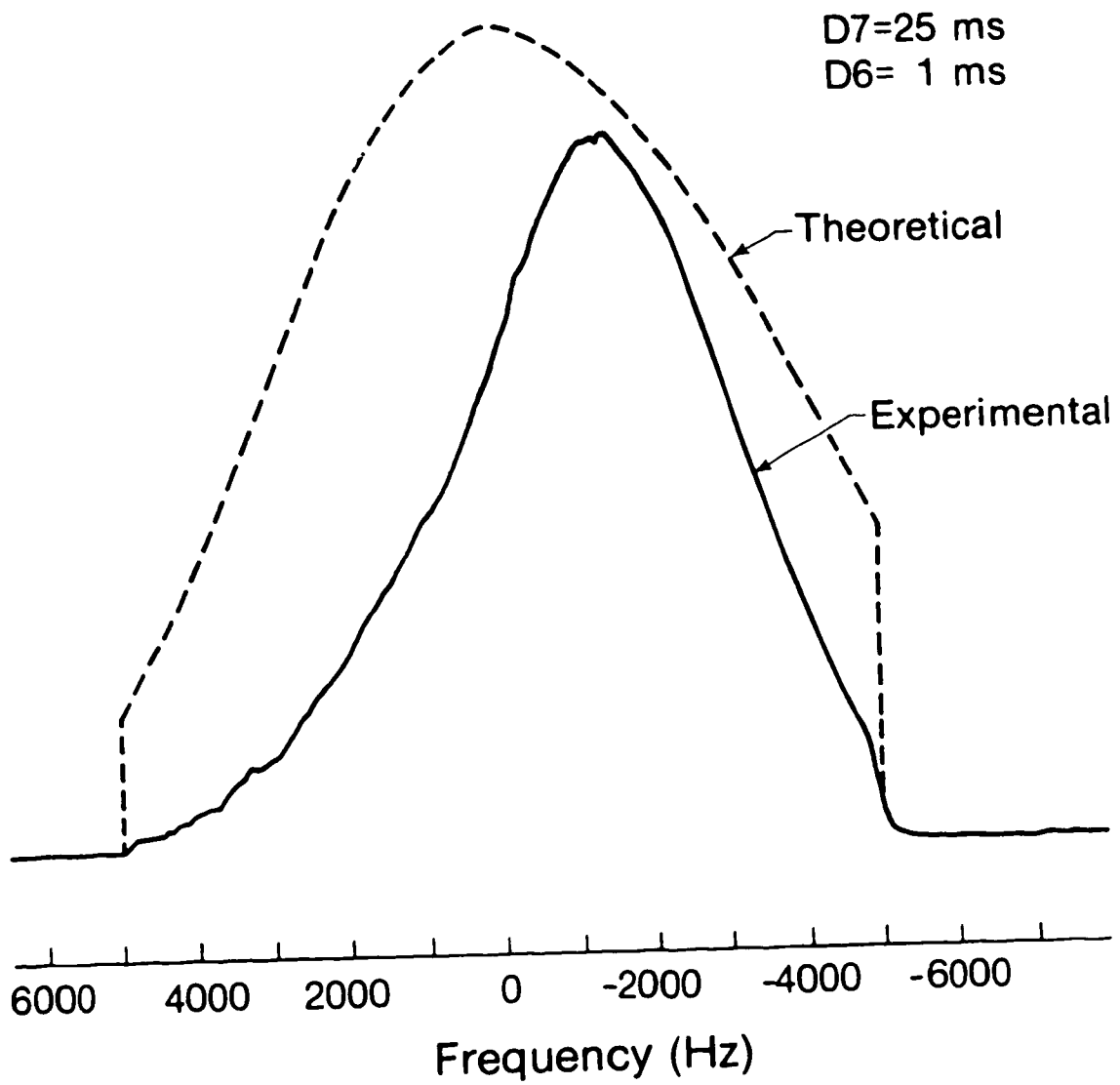
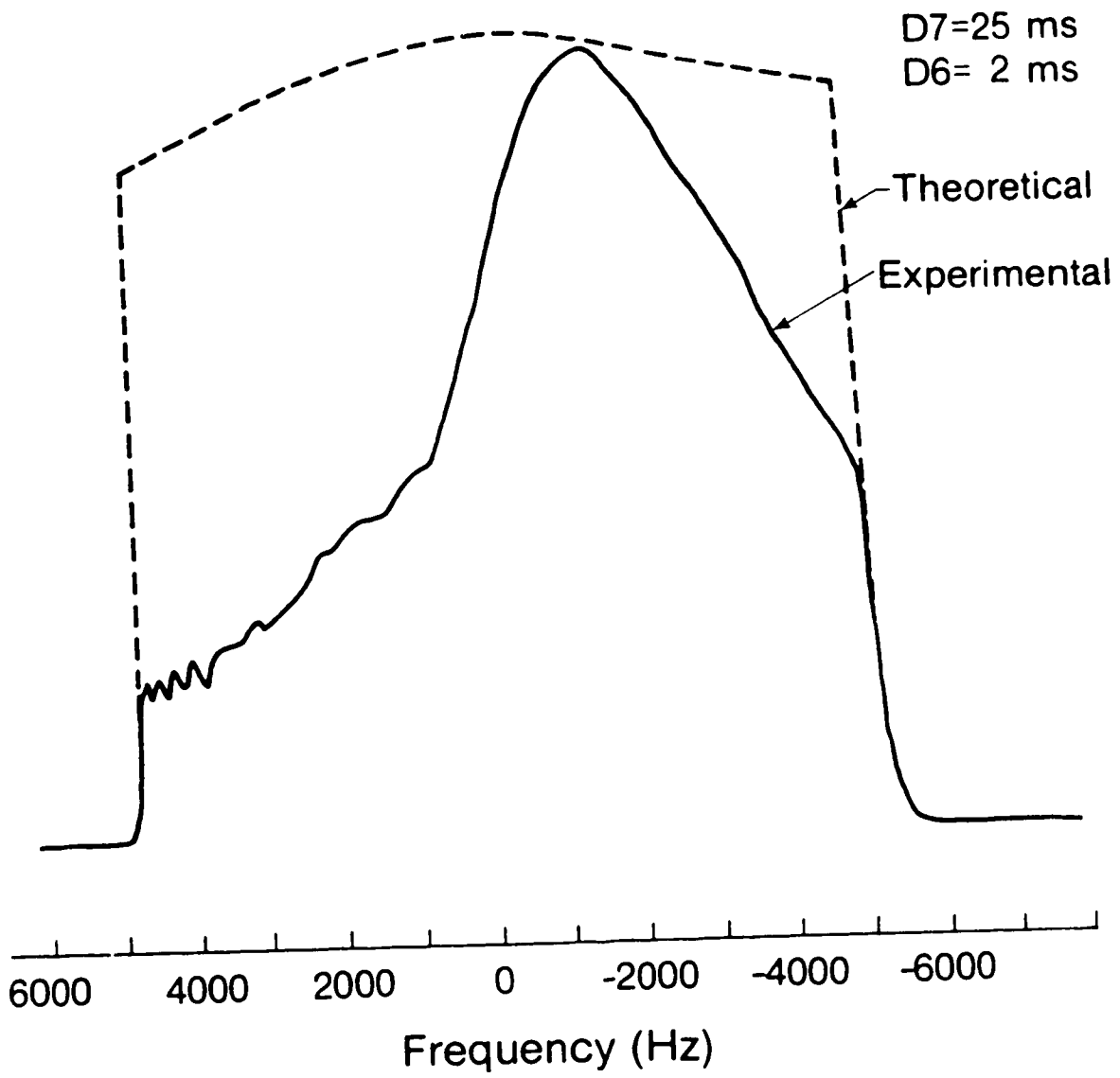




Fig. 34

Projection obtained using the slice phantom filled with doped water and the pulse program SRPP.PC with  $D7 = 25 \text{ ms}$ ,  $D6 = 2 \text{ ms}$ ,  $D25 = 150 \mu\text{s}$ ,  $D3 = 5 \text{ ms}$ ,  $D1 = 300 \mu\text{s}$ ,  $D4 = 2.6 \text{ ms}$  and  $\tau_{aq}/2 = 6.4 \text{ ms}$  ( solid curve ). A calculated projection ( dashed curve ) based on the off-resonance effect is also shown.



obtained from Fig. 23 or 24, depending on the value of D7. If D6 were 1 ms, the offset frequencies of interest are those which occur at the centre of the " $\pi$ -pulse", i.e. at 1.15 ms. Similarly, if D6 = 2 ms, then the frequencies of interest are those at  $t = 2.15$  ms.

The offset frequencies are assumed to arise entirely from a linear gradient field for the purpose of these calculations. (As has been shown, there is also a small magnetic field contribution.) Thus, to find the offset frequencies at other values of  $x$ , say  $x_1$ , one simply multiplies the frequency offset at  $x = +4$  cm, if  $x_1$  is positive, or at  $x = -4$  cm, if  $x_1$  is negative, by the ratio of  $x_1 / (\pm 4 \text{ cm})$ . This offset frequency is then divided by 1670 Hz to obtain the ratio  $\Delta B/B_1$  at the particular value of  $x$ . Knowing the value of  $\Delta B/B_1$ , the transverse magnetization at time  $T_E$  can then be found using Fig. 5. The calculated projections shown in Figs. 31, to 34 have been scaled such that the maximum intensity is equal to the maximum intensity observed in any of the projections, for the particular value of D7.

In Fig. 31, in which D7 was 5 ms and D6 was 1 ms, the shape of the calculated projection is very similar to the actual projection. However, it is clear that the projection is shifted down frequency by about 700 Hz. This may be due in part to a magnetic field caused by the eddy currents. However, the data shown in Fig. 23 indicates that such a field is not large enough to explain the observed shift. Also, it appears that the overall intensity in the experimental projection is reduced. This shows that there are other mechanisms causing intensity artifacts.

In Fig. 32, for which D7 = 5 ms and D6 = 2 ms, the calculated projection again shows that off-resonance effects are present. However, since the offset frequencies are smaller here, the effect is much smaller.

Fig. 33 shows the calculated projections for D7 = 25 ms and D6 = 1 ms. Again, the two projections are similar. However, the marked differences on the positive frequency side indicate that there are other effects causing a loss of intensity. Also, the

frequency at which maximum intensity occurs in the experimental projection is shifted down frequency by about 1500 Hz. Again, this may be due in part to a magnetic field caused by the eddy currents, which is larger here than for a 5 ms gradient pulse.

Fig. 34 shows the calculated projections for  $D7 = 25$  ms and  $D6 = 2$  ms. The off-resonance effect is still present but it is clear that another mechanism is dominating.

In summary, off-resonance effects explain some of the features of the projections with short  $D6$ 's. However, another mechanism must be present which is stronger for longer gradient pulses. It is also clear from the calculated projections and the graphs of frequency offset that, if  $D6 \geq 4$  ms, off-resonance effects will not cause any noticeable intensity artifacts for read compensation gradient pulse lengths of 5 ms and 25 ms. This is consistent with the fact that previous researchers in our *in vivo* NMR group found that a delay of 5 ms between the read compensation gradient pulse and the  $\pi$ -pulse gives satisfactory images.

## 6.2 Phase shift effects caused by eddy currents

As was shown in Figs. 18 to 22, the offset frequencies at different values of  $y$  for a particular value of  $x$  are not always equal. This causes the spins along an isochromat to acquire different phases before the acquisition period ( see sec. 3.5.3 ). The intensity loss due to these phase shifts can be estimated in the following manner. One must make an assumption about the  $y$ -dependence of the frequency effects for a particular value of  $x$ . For simplicity, we assume that it is parabolic and centered about  $y = 0$  cm, although that is not quite the case since the frequency offset at  $y = \pm 5$  cm are not equal. Knowing the timings for a particular projection, one calculate the phase angle  $\delta$  acquired by nuclei at  $y = \pm 5$  cm relative to those at  $y$  cm. This is done most accurately using the difference frequencies shown in Figs. 25

to 30. First, the area under the appropriate curve ( i.e.  $x = 0$  cm,  $\pm 4$  cm,  $D7 = 5$  ms, 25 ms ) from time  $t = 0$  to  $t = D6$  is measured. This corresponds to the phase angle difference,  $\alpha$  say, between the nuclei at  $y = 0$  cm and those at  $y = \pm 5$  cm acquired before the  $\pi$ -pulse. As a result of the  $\pi$ -pulse, this phase angle will be reversed ( i.e.  $\alpha \rightarrow -\alpha$  ). The nuclei will gain an additional phase angle difference, say  $\alpha'$ , given by the area under the same curve from time  $t = D6 + 300 \mu\text{s}$  to  $T_E$ . Thus, at time  $T_E$ , the phase difference  $\delta$  between the nuclei at  $y = 0$  cm and at  $y = \pm 5$  cm is equal to  $\alpha' - \alpha$ . Assuming a parabolic dependence of the offset frequency on  $y$ , the phase angle  $\chi(y)$  at other values of  $y$  will be given by

$$\chi(y) = y^2 \delta / 25^2 \quad (36)$$

where  $y$  is measured in cm.

If we assume that the magnetization at  $y = 0$  cm is in the  $y'$  direction at time  $T_E$ , the net  $y'$  magnetization at time  $T_E$  will be given by

$$\begin{aligned} M_{y'} &= M_0 \int_{-5}^{+5} \cos \chi(y) dy / \int_{-5}^{+5} dy \\ &= M_0 \int_0^{+5} \cos \{ \delta y^2 / 25 \} dy / 5 \end{aligned} \quad (37)$$

where the limits of integration are from  $y = -5$  cm to  $+5$  cm since this is the extent of the slice phantom. Equation 37 can be rearranged to give

$$M_{y'} = M_0 (\pi / 2 \delta)^{1/2} \int_0^{\sqrt{2\delta/\pi}} \cos \{ (\pi/2) t^2 \} dt \quad (38)$$

where  $M_0$  is the transverse magnetization when all the spins are in phase. The final integral is a well-known Fresnel integral,  $C(z)$ , where  $z$  is  $(2\delta/\pi)^{1/2}$ . Thus, once  $\delta$  is known, Fresnel integral tables can be used to determine  $M_y'$ .

Similarly,  $M_x'$  at time  $T_E$  is found to be  $M_0 S(z)$  where  $z$  is  $(2\delta/\pi)^{1/2}$  and  $S(z)$  is the other Fresnel integral. Thus, the final transverse magnetization,  $M_{x'y}'$ , at time  $T_E$  is given by

$$M_{x'y}' = M_0 (\pi/2\delta)^{1/2} [C^2\{(2\delta/\pi)^{1/2}\} + S^2\{(2\delta/\pi)^{1/2}\}]^{1/2}. \quad (39)$$

Since  $C(z)/z \rightarrow 1$  and  $S(z)/z \rightarrow 0$  as  $z \rightarrow 0$ , it can be seen that  $M_{x'y}' \rightarrow M_0$  as  $\delta \rightarrow 0$ . This is as expected.

The normalized intensity ( $M_{x'y}'/M_0$ ) has been calculated at  $x = 0$  cm and  $x = \pm 4$  cm for two different values of  $D7$  and three different values of  $D6$ . The results are presented in Table I.

In summary, when the read compensation gradient pulse duration is 5 ms, the estimated intensity losses due to phase cancellation effects are minor in most cases. No correlation of calculated intensity losses with observed losses could be made. We therefore deduce that another mechanism must be responsible for the intensity losses shown in Figs. 11 and 12. For a 25 ms read compensation gradient pulse, quite large intensity losses were calculated at  $x = \pm 4$  cm. These were of the same order of magnitude as the intensity losses shown in Figs. 14 and 15. However, the agreement is not exact and the intensity losses cannot be fully accounted for by off-resonance effects and phase shifts.

**TABLE I**

Calculated values using equation 39 of the normalized transverse magnetization  $M_{x'y'}/M_0$  based on phase cancellation at positions  $x = +4$  cm, 0 cm and -4 cm for various values of D7, the duration of the read compensation gradient pulse, D2, the duration of the read gradient before the data acquisition and D6, the delay between the read compensation gradient pulse and the  $\pi$ -pulse.

D7 (ms)	D2 (ms)	D6 (ms)	M <sub>x'y'</sub> /M <sub>0</sub>		
			x = +4 cm	x = 0 cm	x = -4 cm
5	2		1.00	1.00	0.98
5	2	5	1.00	1.00	0.99
5	2	30	0.99	0.99	0.91
25	30.2	2	0.29	0.97	0.31
25	30.2	20	0.82	0.93	0.99
25	30.2	40	0.97	0.99	0.78

### 6.3 Improper refocussing of the spin-echo

This effect is studied by measuring the areas under the decay curves from  $t = 0$  to  $T_E/2$  and from  $t = T_E/2$  to  $T_E$ . This is done for  $x = +4$  cm and  $-4$  cm and for two different pulse durations  $D7 = 5$  ms and  $25$  ms using Figs. 23 and 24 respectively. Several different values of  $D6$  are chosen corresponding to several different values of  $T_E/2$ . Subtraction of the areas on either side of the  $\pi$ -pulse gives a measure of the net phase shift  $\psi$  caused by the slow decay of the read compensation gradient pulse. These measured values are listed in Table II.

The values shown in Table II are arbitrary in the sense that, in the "trimming" routine, the magnitude of the read compensation gradient pulse is adjusted until the echo is formed at time  $T_E$ . For the case when  $D7 = 5$  ms, the trimming routine was carried out with  $D6 = 5$  ms and no further trimming was done when  $D6$  was changed. Referring to the second row in Table II, we deduce that the trimming routine must have added approximately 4.05 cycles to the phase angle accumulated at  $x = +4$  cm and subtracted 4.05 cycles from the phase angle accumulated at  $x = -4$  cm. We take account of such trimming by adding 4.05 cycles to all values of  $\psi/2\pi$ , i.e. for all the various values of  $D6$ , at  $x = +4$  cm and subtracting 4.05 cycles from all the values at  $x = -4$  cm. These "corrected" phase angles,  $\psi_{\text{cor}}/2\pi$ , are shown in Table III.

When using the long read compensation gradient pulse ( $D7 = 25$  ms), trimming was performed with a  $D6$  value of  $20$  ms. Referring to Table III, we can see that for  $D6 = 20$  ms,  $\psi/2\pi$  is  $-6.6$  cycles at  $x = -4$  cm and  $+9.0$  cycles at  $x = +4$  cm. This very substantial difference implies that one cannot simultaneously form the echoes from nuclei at  $x = +4$  cm and  $x = -4$  cm at the same time  $T_E$ . In the absence of information to the contrary, we assume that the "trimming" procedure added roughly  $(6.6 + 9.0) / 2$  or  $7.8$  cycles to the phase angle accumulated at  $x = +4$  cm and



Calculated values of the phase shift  $\psi / 2\pi$  at  $x = +4$  cm and  $x = -4$  cm caused by eddy currents for various values of D7, the duration of the read compensation gradient pulse and D6, the delay between the switch-off of this gradient pulse and the  $\pi$ -pulse.

D <sub>7</sub> (ms)	D <sub>6</sub> (ms)	$\psi / 2\pi$ (cycles)	
		$x = +4$ cm	$x = -4$ cm
5	2	-2.8	+2.4
5	5	-4.1	+4.0
5	15	-4.0	+4.5
5	30	-4.4	+5.5
25	2	-3.9	+0.2
25	14	-5.8	+7.1
25	20	-6.6	+9.0
25	26	-7.2	+10.6
25	40	-6.5	+12.4

**TABLE III**

Corrected phase shifts  $\Psi_{\text{corr}} / 2\pi$  at positions  $x = +4$  cm and  $x = -4$  cm for various values of D7, the duration of the read compensation gradient pulse and D6, the delay between the switch-off of this gradient pulse and the  $\pi$ -pulse.

D7 (ms)	D6 (ms)	$\Psi_{\text{corr}} / 2\pi$ (cycles)	
		$x = +4$ cm	$x = -4$ cm
5	2	+1.3	-1.6
5	5	0.0	0.0
5	15	+0.1	+0.5
5	30	+0.3	+1.0
25	2	+3.9	-7.6
25	14	+2.0	-0.7
25	20	+1.7	-1.2
25	26	+0.6	+2.8
25	40	+1.3	+4.6

subtracted 7.8 cycles from the phase angle at  $x = -4$  cm. These "corrected" phase shifts,  $\psi_{\text{corr}}/2\pi$ , are listed in Table III.

The result of these phase shifts is that the echoes are not formed precisely at  $T_E$ . Since the gradient strength during data acquisition is  $-1000$  Hz/cm, nuclei at  $x = +4$  cm and  $-4$  cm have offset frequencies of  $-4000$  Hz and  $+4000$  Hz respectively. The time difference  $\Delta t$  from  $T_E$  at which the echo is formed is thus given by  $\psi_{\text{corr}}/2\pi$  divided by  $-4000$  Hz for  $x = +4$  cm and by  $\psi_{\text{corr}}/2\pi$  divided by  $+4000$  Hz for  $x = -4$  cm. The calculated time differences  $\Delta t$  are listed in Table IV. A similar calculation using data presented in Figs. 23 and 24 shows that the time difference  $\Delta t$  is negligible for nuclei at  $x = 0$  cm.

A rough estimate of the loss of intensity caused by the echo forming at a time other than  $T_E$  can be obtained by examining the echo envelope shown in Fig. 9. However, a better method is to study the intensity artifacts that result from changing D2, the duration of the read gradient before the data acquisition begins, while varying D4 to keep  $T_E$  constant. In this way, the time at which the echo is formed is artificially moved relative to  $T_E$ . Fig. 13 shows projections obtained for various values of D2 while using a 5 ms read compensation gradient pulse ( $D7 = 5$  ms) and a D6 of 5 ms. Similarly, Fig. 16 shows projections obtained for various values of D2 while using a D7 of 25 ms and a D6 of 20 ms.

We can now study improper refocussing of the echo by comparing the effect of artificially changing the time of echo formation in Figs. 13 and 16 with the effect of varying D6 in Figs. 11, 12, 13 and 14, thereby causing the echoes to form at different times because of the phase shifts caused by the eddy currents.

We first consider the intensity artifacts obtained with a read compensation pulse duration of 5 ms. When D6 is 2 ms, it can be seen from Table IV that the time difference  $\Delta t$  is  $-0.3$  ms at  $x = +4$  cm and  $-0.4$  ms at  $x = -4$  cm. The observed intensity loss at  $x = +4$  cm (corresponding to  $-4000$  Hz) and at  $x = -4$  cm

**TABLE IV**

Values of the time difference  $\Delta t$  (ms) between the time of the echo formation and  $T_E$  for nuclei at  $x = +4$  cm and at  $x = -4$  cm as a function of D7, the duration of the read compensation gradient pulse and D6, the delay between the the switch-off of this gradient and the  $\pi$ -pulse.

D7 (ms)	D6 (ms)	$\Delta t$ (ms)	
		$x = +4$ cm	$x = -4$ cm
5	2	-0.3	-0.4
5	5	0.0	0.0
5	15	0.0	+0.1
5	30	+0.1	+0.3
25	7	-1.0	-1.9
25	14	-0.5	-0.2
25	20	-0.3	-0.3
25	26	-0.2	+0.7
25	40	-0.3	+1.2

( corresponding to +4000 Hz ) as compared with that at  $x = 0$  cm ( 0 Hz ) in Fig. 11 should be similar to the intensity loss at +4000 Hz and -4000 Hz found with  $D2 = 2.4$  ms in Fig. 13. This intensity loss should be measured in Fig. 13 relative to the intensity measured at 0 Hz and with  $D2 = 2.0$  ms since  $\Delta t = 0$  at 0 Hz as mentioned above. At  $x = -4$  cm, the predicted intensity loss is roughly 25% and at  $x = +4$  cm, the predicted intensity loss is roughly 10%. The actual intensity loss observed in Fig. 11 is about 40% at  $x = -4$  cm while it is about 10% at  $x = +4$  cm. This is very good agreement when one includes the losses arising from the off-resonance effect ( see Fig. 11 ).

For the case  $D6 = 5$  ms, no intensity artifacts arising from this mechanism are predicted. As observed in Fig. 11, this projection has the most "top-hat" shape of all.

For the case  $D6 = 15$  ms, the time difference at  $x = +4$  cm is given in Table IV as 0.0 ms and at  $x = -4$  cm by 0.1 ms. Thus, no intensity loss should occur in this projection at  $x = +4$  cm. At  $x = -4$  cm, the echo will form 0.1 ms later than  $T_E$  and should cause an intensity artifact similar to that in Fig. 13 when  $D2$  is 1.9 ms. We can see that the intensity at  $x = -4$  cm is increased when  $D2$  is shortened by 0.1 ms but not as much as in the projection in which  $D6 = 15$  ms ( Fig. 12 ) and  $D2$  is 2 ms. Around  $x = +4$  cm ( i.e. around -4000 Hz ), there appears to be no difference in the shapes of the projections except for some overall intensity reduction due to  $T_2$  effects, as expected. Hence, when  $D6 = 15$  ms, one may say that there is some evidence of an effect due to improper refocussing of the echoes from the different regions of the sample.

For the case  $D6$  is 30 ms ( see Fig. 12 ), virtually no effect is predicted on the negative frequency side while the intensity on the high positive frequency side should be about 20% higher. Observation of the projection shows that the overall intensity is reduced due to  $T_2$  effects and the high positive frequency side is about 10% higher. This is in qualitative agreement with the predictions.

Now we turn to the projections where the pulse duration,  $D_7$ , is 25 ms. For the case  $D_6$  is 2 ms ( see Fig. 14 ), the intensity is expected to be slightly higher at  $x = +4$  cm, but more than 50% lower at  $x = -4$  cm. This is in qualitative agreement with the observed projection when one includes the intensity loss caused by the off resonance effect ( see Fig. 34 ) and the phase shift effect ( see sec. 6.2 ).

For the projection where  $D_6$  is 14 ms ( see Fig. 14 ), the agreement again is quite good. The case in which  $D_6$  is 20 ms ( see Fig. 14 ), the value used in the trimming procedure, shows that the echoes from the two regions will not form at the same time, regardless of the trimming routine. This will presumably lead to intensity losses as observed in the projection. When  $D_6$  is 26 ms ( see Fig. 15 ), the peak observed at high positive frequencies is as expected from this mechanism. However, when  $D_6$  is 40 ms ( see Fig. 15 ), a sharp peak at high positive frequencies is expected but, in fact, these frequencies are quite strongly attenuated. This may be a result of the previously described phase shift effects for this particular set of timing.

In summary, imperfect refocussing of the spin-echoes explains, in most cases, the intensity artifacts not accounted for by the previously discussed off-resonance and phase shift effects. It is quite clear that the effect is worse when  $x$  is negative and for long read compensation gradient pulses.

## CHAPTER 7

### CONCLUSIONS AND RECOMMENDATIONS

It should be clear to the reader that the subject of intensity artifacts in MRI is very complicated. In the investigations reported in this thesis, we have identified three major sources of intensity loss associated with Fourier transform spin-echo imaging. These are:

- 1) off-resonance effects associated with switching on the " $\pi$ -pulse" too soon after the switch-off of the read compensation gradient pulse;
- 2) destructive interference caused by nuclei at different values of  $y$  ( for a particular value of the coordinate  $x$  ) experiencing different fields due to the eddy currents and, hence, acquiring different phase angles;
- 3) improper refocussing of the echoes because of the different fields due to the eddy currents experienced by the nuclei in different regions of the sample.

The first cause of intensity loss is largely independent of the duration of the read compensation pulse. The second and third are much more important when the read compensation pulse is of long duration.

To achieve high quality images with faithful reproduction of intensity, the following recommendations are made.

- 1) Sufficient time must be allowed after the read compensation pulse for the field gradient to decay. A 5 ms delay is adequate with the present gradient coils.
- 2) In order to avoid intensity artifacts associated with phase cancellations, it is very important that shielded gradients are employed such that eddy currents are not induced in the conducting parts of the magnet.
- 3) The effect of improper refocussing will be largely eliminated by the use of shielded gradients since the echoes from the different regions will be formed at the

same time. However, this effect of improper refocussing can also be reduced by improving the field homogeneity. Observation of the spectrum of the slice phantom in the absence of pulsed field gradients ( Fig. 10 ) shows that the field varies by more than 0.5 G over the region of the slice phantom. This is larger than expected. It is believed that the nonlinear shims are not being adjusted properly. The method described by Romeo and Hout ( 1984 ) should be used to adjust the nonlinear shims.

Areas for future research of intensity artifacts in MRI include studying the artifacts discussed in this thesis after implementation of a shielded gradient set. Also, the effects of a varying amplitude read gradient pulse during the data acquisition period could be studied.



**BIBLIOGRAPHY**

- Abragam, A., 1961, **The principles of Nuclear Magnetism**, ( Clarendon Press ).
- Bloch, F., Hanson, W.W., and Packard, M.E., 1946, **Phys. Rev.** 69, 127.
- Brateman, L., Jennings, L.W., Nunnally, R.L. and Vaughan, J.T., 1986, **Med. Phys.** 13 (4) , 441.
- Brigham, E. O., 1974, **The Fast Fourier Transform**, Prentice-Hall.
- Cho, Z.H., Ahn, C.B., Lee, S.Y. and Nalcioglu, O., 1987, **Med. Phys.** 14 (1), 43.
- Ernst, R.R., Welti, D. and Kumar, A., 1975a, **J. Magn. Reson.** 18, 69.
- Farrar, T.C. and Becker, E.D., 1971, **Pulse and Fourier Transform NMR**, ( Academic Press ).
- Gabillard, R., 1951, **C. R. Acad. Sci. ( Paris )**, 232, 1551.
- Gastine, M., Courtois, L., and Dorman, J.L., 1967, **I.E.E.E. MIT-15**, 694.
- Hahn, E.L., 1950, **Phys. Rev.** 77, 297.
- Hayes, C.E., Edelstein, W.A., Schenck, J.F., Mueller, O.M. and Eash, M., (1985), **J. Magn. Reson.**, 63, 622.
- Henkelman, R.M. and Bronskill, M.J., (1987), **Reviews of Magnetic Resonance in Medicine**, 2 (1) , pp. 1 - 126.
- Hoult, D.I., 1979, **J. Magn. Reson.**, 35, 69.
- Lai, C.M., 1983, **Phys. Med. Biol.**, 28 (8), 925.
- Lauterbur, P.C., 1973, **Nature, Lond.**, 242, 190.
- Mansfield P., and Grannel, P.K., 1973, **J. Phys.**, C6, L422.
- Mansfield, P., Maudsley, A.A., Morris, P.G. and Pykett, I.L., 1979a, **J. Magn. Reson.** 33, 261.

- Mansfield, P., and Morris, P.G., 1982, **NMR Imaging in Biomedicine**,  
( Academic Press )
- Mansfield, P. and Chapman, B., 1986, **J. Phys. E.: Sci. Instrum.**, 19, 540.
- Meiboom, S. and Gill, D., 1958, **Rev. Scient. Instrum.**, 19, 688.
- Morris, P.G., 1986, **Nuclear Magnetic Resonance in Medicine and  
Biology**, ( Clarendon Press ).
- Romeo, F., and Hoult, D.I. , 1984, **Magnetic Resonance in Medicine**, 1, 44.
- Roschmann, P. and Jensen, D., **Proceedings of the 7th Annual Meeting of  
SMRM**, San Fransisco, Aug. 1988, p. 267.
- Slichter, C.P., 1963, **Principles of Magnetic Resonance**, ( Harper and Row ).
- Vollman, W., 1984, **Magnetic Resonance Imaging**, 2, 221.